SEDE AMMINISTRATIVA

UNIVERSITÀ DEGLI STUDI DI PADOVA

DIPARTIMENTO DI FISICA

SCUOLA DI DOTTORATO IN SCIENZA ED INGEGNERIA DEI MATERIALI
XX CICLO

CHEMICAL METHODS FOR THE PREPARATION OF GOLD PARTICLES BASED NANOSTRUCTURES AND NANOCOMPOSITES

Direttore della scuola: Ch.mo. Prof. GAETANO GRANOZZI

Supervisore: Ch. mo Prof. PAOLO MAZZOLDI

Dottorando: MARCO BERSANI

DATA CONSEGNA TESI
31 gennaio 2008

Motivazione e Schema della Tesi

Negli ultimi anni, l'avvento di nuove strategie sintetiche e di nuovi modi di interpretare strategie ben note ha consentito di iniziare a pensare in termini di dimensioni estremamente ridotte. L'attenzione si è perciò concentrata su scale submicrometriche e nanoscopiche in quasi tutti i campi della ricerca scientifica, tanto che ricercatori con formazioni tradizionalmente diverse stanno cercando di sfruttare le medesime innovative proprietà e allo stesso tempo affrontando i medesimi problemi. La sovrapposizione tra aree di ricerca storicamente indipendenti è diventata così signficativa da renderle quasi indistinguibili, favorendo in tal modo uno scambio di conoscenze e competenze che non trova precedenti e conduce verso lo sviluppo di un vasto modello scientifico interdisciplinare. Il confine tra fisica, chimica, biologia ed ingegneria è sempre meno netto e marcato dal momento che tutte queste discipline si stanno confrontando con i componenti fondamentali della materia. Lavorare con cluster di atomi o molecole al fine di ottenere un fine controllo sulle proprietà del prodotto finale è oggi piuttosto comune: il cosiddetto approccio "bottom-up" si fonda principalmente sulla possibilità di controllare i componenti a livello molecolare, svelando così nuove proprietà e caratteristiche che vanno ben oltre le tipiche potenzialità dei processi su scala macroscopica.

Uno degli aspetti più affascinanti è che ciò ha suggerito un modo per combinare elementi organici ed inorganici molto più efficace dei metodi tradizionali. Solitamente, il fattore limitante risultava legato a questioni di stabilità termica, separazione di fase o processabilità, che erroneamente apparivano come caratteristiche così intrinseche da prevenire ogni contatto tra il mondo organico e quello inorganico. Si possono tuttavia identificare molti passaggi chiave nel superamento di queste limitazioni: una miglior comprensione dei principi fisici che governano la formazione di nanostrutture, la crescente disponibilità di precursori organici e inorganici con un'ampia gamma di funzionalità, gli enormi miglioramenti nelle tecniche di caratterizzazione.

Allo stesso modo, la chimica dei materiali è entrata prepotentemente nel mondo della biologia molecolare e della medicina. Se inizialmente le interfacce tra questi due mondi si limitavano a poche applicazioni nel campo dei materiali biocompatibili per prostetica e alle limitate necessità degli strumenti per le analisi di laboratorio, l'odierna capacità di produrre oggetti su scala cellulare e subcellulare ha messo a disposizione della diagnostica un ampio set di nanosonde e nanovettori per la veicolazione in situ di farmaci. Le implicazioni di questo processo sono enormi, e sorprendentemente non unilaterali: se da un lato ciò sta portando alla definizione di *nanomedicina*, d'altra parte anche le scienze e le tecnologie non biologiche stanno accogliendo principi e materiali biologici nei loro ultimi sviluppi.

La complessità del mondo biologico si può allora riversare nei più disparati ambiti: dalla sintesi di nanoparticelle inorganiche template da polipeptidi di sintesi, a fibre polimeriche con gradienti di densità e proprietà meccaniche che mimano struttura e comportamento di tessuti organici dei molluschi, fino a superfici che riproducono l'articolata rugosità della foglia di loto mimandone l'idrorepellenza. Questo approccio, generalmente denominato *biomimetica*, non esaurisce tuttavia la questione.

La natura infatti ha come costituente fondamentale la capacità di selezionare non solo le specie ma specialmente i principi e gli algoritmi più efficienti. Ecco allora che si iniziano a pensare sistemi di calcolo in grado di replicare le tecniche risolutive che usa il cervello per affrontare le molteplici problematiche cui è continuamente sottoposto. Si parla allora di reti neurali e calcolo in parallelo, fino ai primi esempi di calcolo basato sul DNA. Il DNA (con l'RNA) è certamente una delle molecole più intriganti che la natura ha selezionato, sia strutturalmente che concettualmente.

Non deve quindi sorprendere che l'interesse di molti ricercatori nel campo dei materiali si sia focalizzato proprio sul DNA: è un polimero molto robusto, che con minime precauzioni può essere estratto dal contesto biologico; è facilmente reperibile e sintetizzabile; esistono già numerose tecniche e mezzi di caratterizzazione, ampiamente disponibili e di costo contenuto; ma soprattutto, il meccanismo di sequenziazione ed accoppiamento delle basi azotate offre uno strumento potentissimo e senza precedenti per introdurre informazioni arbitrarie su scala nanoscopica.

Se questa comprensione delle relazioni che intercorrono tra diverse aree della scienza è relativamente recente, è possibile identificare un piccolo insieme di elementi che hanno dimostrato di avere un grande interesse tecnologico e scientifico attraverso i secoli, attraversando di volta in volta ogni epoca scientifica grazie alla scoperta qualche nuova peculiare proprietà: i metalli nobili. Storicamente detti metalli da conio poiché usati come moneta, deposito di valuta o gioielli, sono oggi un materiale fondamentale per l'industria elettrica ed elettronica, mentre molte delle loro proprietà di recente scoperta sono ancora alla ricerca di un'applicazione. Tra i metalli nobili, l'oro ha certamente una posizione speciale: è il più duttile e malleabile tra i metalli noti, e la sua lavorabilità combinata con il suo attraente color giallo e la sua lucentezza superficiale sono stati un fattore fondamentale nel promuovere lo studio e lo sviluppo del materiale. È curioso notare come che alcune delle sue proprietà tipiche della scala nanometrica sono state involontariamente sfruttate dagli antichi artigiani, ad esempio quando utilizzavano minerali contenenti metalli nobili per la produzione di vetri colorati. Techinche di caratterizzazione moderne, accoppiate alla riproduzione delle antiche preparative, hanno permesso di comprendere il processo, che ricorda incredibilmente le moderne strategie di sintesi con le limitazioni imposte dalla tecnologia del tempo.

In questa tesi, si sono perciò esplorate alcune delle possibili interazioni dell'oro con i diversi ambiti dei materiali organici, inorganici, ibridi e biologici, fornendo esempi delle diverse strategie di sintesi e combinazione. Nel **CAPITOLO 1** si è cercato di definire il contesto scientifico in cui si è collocata la ricerca svolta, oltre a fornire i principi fondamentali di alcune delle tecniche sintetiche utilizzate. Nel **CAPITOLO 2** è stata descritta la sintesi colloidale e la caratterizzazione di piccoli cluster d'oro fluorescenti ($D < 2$ nm), con la conseguente introduzione in matrici organiche, ibride e inorganiche. Nel **CAPITOLO 3**, si è studiata la sintesi in-situ di nanoparticelle d'oro e argento in matrice polimerica, in particolare esplorando il processo di introduzione e diffusione degli ioni metallici nelle poliimmidi aromatiche fluorurate e la formazione dei nanocluster in seguito a trattamenti termici. Infine, nel **CAPITOLO 4** si sono esplorate nuove strategie per l'organizzazione a livello nanoscopico di materiali per l'elettronica delle prossime generazioni, accoppiando le nanoparticelle d'oro a particolari strutture di DNA dette origami.

La ricerca è stata svolta nei laboratori dei Dipartimenti di Fisica e di Ingegneria Meccanica dell'Università di Padova, nei Laboratori Nazionali di Legnaro dell'INFN, nel Centro di Ricerca IBM di Almaden (San Jose, CA) e nel dipartimento di Computer Science a Caltech (Pasadena, CA).

"I never ask advice about growing," Alice said indignantly.

"Too proud?" the other enquired.

Alice felt even more indignant at this suggestion. "I mean," she said, "that one ca'n't help growing older."

"One can't, perhaps," said Humpty Dumpty; "but two can. With proper assistance, you might have left off at seven."

Lewis Carroll, Through the Looking Glass

Monter, descendre, aller, venir, tant fait l'homme qu'à la fin il disparaît.

Raymond Quenau

Alla mia famiglia

Table of Contents

Chapter 1

Theory and Background

1.1 Introduction

In recent years, new synthetic routes and new approaches to long-known ones have established the possibility of thinking in terms of extremely small size. The main focus has today been shifted to the submicrometer and nanometer scale in almost every scientific field, thus implying that even researchers coming from traditionally different backgrounds are now exploiting the same novel properties, and at the same time facing the same issues. The overlap between historically independent areas of research has become so significant to make them almost undistinguishable, favoring an unprecedented exchange of knowledge in the development of a broad interdisciplinary science. The line between physics, chemistry, biology and engineering is becoming always fuzzier and thinner, since all of them are now dealing with the basics components of matter. Working with clusters of atoms or molecules with the purpose of achieving a fine control upon the properties of the final product is today pretty common: the so-called “bottom-up” approach mainly relies on the possibility of mixing and reacting components at a molecular level, disclosing novel properties and characteristics that go beyond the traditional macroscale processing capabilities.

One of the most exciting aspects is that it has suggested a way to combine organic and inorganic compounds in a way that is much more effective than the traditional techniques. The limiting factor was typically connected with thermal stability, phase separation or processability issues, which erroneously appeared as features so intrinsic to prevent any efficient contact between the organic and inorganic world. Several crucial steps can be identified in the overcoming of such limitations: a better understanding of the physical principles governing the formation of structure at the nanoscale level, the increasing availability of organic-inorganic precursors with a wide range of functionalities, the huge improvements in the characterization techniques.

In the same way, materials chemistry has veemently entered the world of molecular biology and medicine. While initially the interfaces between these two worlds were limited to a few applications in the field of biocompatible materials for prosthetics and the needs for a few very specific tools of analytical labs, modern capabilities of producing objects on a cellular and sub-cellular size scale have made available a wide set of nanoprobes for diagnostics and nanovectors for the *in-situ* delivery of drugs for pharmacology. The implications of such a process are huge, and surprisingly not unilateral: if on one side the definition of a *nanomedicine* is becoming clear, on the other also non-biological sciences and technologies are introducing biological principles and materials in their latest developments.

The complexity of the biological world and its knowledge can then be applied in the most different areas: from the preparation of inorganic particles with peculiar morphology and crystallinity templated by synthetic polypeptides, to polymeric fibers with density gradients and mechanical properties mimicking the structure and behavior of sea shell organic tissue, up to surfaces reproducing the articulated roughness of the lotus leaf and its hydrophobicity. This approach, that is generally referred to as *biomimetics*, provides just an initial understanding of the topic.

In fact, nature has as a fundamental constituent the capability of selecting not only species ma in particular the most efficient principles and algorithms. One can then think of system of calculus that can replicate the solving techniques used by the brain to address the extended set of problems it has to face in its daily routine. Here come into play the concepts of neural networks and parallel computation, up to the first examples of DNA-based computing. DNA (and RNA) is certainly one of the most intriguing molecules nature has selected, both structurally and conceptually.

Therefore should be of no surprise that the interest of many researchers in the field of materials has been focused on DNA: it’s a very robust polymer, that with minimal precautions can be extracted from the biological context; it’s widely available and easily synthesizeable; there’s a complete range of existing characterization techniques and tools, often with little cost; but above all, the mechanism of sequencing and pairing of the nitrogenous bases offers an extremely powerful and unprecedented mean to introduce arbitrary informations on a nanoscopic scale.

While these insights on the interplay of different areas of science are relatively recent, it’s possible to identify a small set of compounds that have proven to be of great technological and scientific interest throughout the centuries, breaking through each scientific era thanks to the discovery of some new peculiar properties: noble metals. Historically called coinage metals due their use as money, store of value or jewels, today they are a fundamental material in the electric and electronic industry, while many of the recently discovered nanoscale properties are still looking for an application. Among the noble metals, gold has certainly a special position: it’s the most ductile and malleable of the known metals, and its workability combined with its attractive yellow color and surface luster have been a key factor in the development of the material. It’s curious to notice that some of its nanoscale properties were unvoluntarily exploited by ancient artisans, for example when they were using noble-metal doped ores in the preparation of colored glasses. Modern characterization techniques, coupled with the reproduction of the old recipes, have led to the understanding of the process, which amazingly resembles modern synthetic strategies with the limitation imposed by the technology of the time.

In this thesis, some of the possible interactions of gold with organic, inorganic, hybrid and biological materials are explored, providing examples of different synthetic and combination strategies. The research activity was performed at the laboratories of Physics and Mechanical Engineering Departments at the University of Padova, at the INFN Legnaro National Labs, at the IBM Almaden Research Center (San Jose, CA) and at the Department of Computer Science at Caltech (Pasadena, CA).

1.2 Gold

Gold is a chemical element with the symbol Au (from the Latin aurum, meaning shining dawn) and atomic number 79. It is a soft, yellow metal (mp 1063°C) with the highest ductility and malleability of any element: a single gram can be beaten into a sheet of one square meter. Gold leaf can be beaten thin enough to become translucent. The transmitted light appears greenish blue, because gold strongly reflects yellow and red. Gold readily forms alloys with many other metals. These alloys can be produced to increase the hardness or to create exotic colors (see below). Native gold contains usually eight to ten percent silver, but often much more; alloys with a silver content over 20% are called electrum. As the amount of silver increases, the color becomes whiter and the specific gravity becomes lower.

Gold is a good conductor of heat and electricity, and is not affected by air and most reagents. Heat, moisture, oxygen, sulfur and most corrosive agents have very little chemical effect on gold, making it well-suited for use in coins and jewelry; but reacts readily with halogens or with solutions containing or generating chlorine such as aqua regia, that dissolves it via formation of the chloraurate ion. It also dissolves in cyanide solutions in the presence of air or hydrogen peroxide to form $[Au(CN)_2]^-$. A solution of Cl_2 in acetonitrile in the presence of $[NMe_3H]Cl$ dissolves gold at 30°C at a faster rate than aqua regia, whereas I_2/KI in refluxing methanol selectively dissolves gold with respect to other noble metals. Gold dissolves in mercury, forming amalgam alloys, but does not react with it. Gold is insoluble in nitric acid, which will dissolve silver and base metals, and this is the basis of the gold refining technique known as "inquartation and parting". Nitric acid has long been used to confirm the presence of gold in items, and this is the origin of the colloquial term "acid test," referring to a gold standard test for genuine value. Gold extraction from metal sulfide veins can also be facilitated by sulfur consuming bacteria.

High quality pure metallic gold is tasteless, in keeping with its resistance to corrosion (it is metal ions which confer taste to metals). In addition, gold is very dense, a cubic meter weighing 19300 kg. By comparison, the density of lead is 11340 kg/m³, and the densest element, Iridium, is 22650 kg/m³.

1.2.1 Gold Nanoparticles

Gold nanoparticles (AuNPs) are the most stable metal nanoparticles, and they present fascinating aspects such as their assembly of multiple types involving materials science, the behavior of the individual particles, size-related electronic, magnetic and optical properties (quantum size effect), and their applications to catalysis and biology. Their promises are in these fields as well as in the bottom-up approach of nanotechnology, and they will be key materials and building block in the 21st century. Whereas the extraction of gold started in the 5th millennium B.C. near Varna (Bulgaria) and reached 10 tons per year in Egypt around 1200-1300 B.C. when the marvelous statue of Touthankamon was constructed, it is probable that "soluble" gold appeared around the 5th or 4th century B.C. in Egypt and China. In antiquity, materials were used in an ecological sense for both aesthetic and curative purposes. Colloidal gold was used to make ruby glass and for coloring ceramics, and these applications are still continuing now. Perhaps the most famous example is the Lycurgus Cup (***FIGURE 1.1***) that was manufactured in the 5th to 4th century B.C. It is ruby red in transmitted light and green in reflected light, due to the presence of gold colloids.

***FIGURE 1.1**. The Lycurgus cup in reflected (left) and transmitted light (right).*

The reputation of soluble gold until the Middle Ages was to disclose fabulous curative powers for various diseases, such as heart and venereal problems, dysentery, epilepsy, and tumors, and for diagnosis of syphilis. This is well detailed in what is considered as the first book on colloidal gold, published by the philosopher and medical doctor Francisci Antonii in 1618[1]. This book includes considerable information on the formation of colloidal gold sols and their medical uses, including successful practical cases. In 1676, the German chemist Johann Kunckels published another book[2a], whose chapter 7 concerned "drinkable gold that contains metallic gold in a neutral, slightly pink solution that exert curative properties for several diseases". He concluded, well before Michael Faraday (vide infra), that "gold must be present in such a degree of communition that it is not visible to the human eye". A colorant in glasses, "Purple of Cassius", is a colloid resulting from the heterocoagulation of gold particles and tin dioxide, and it was popular in the 17th century[2b]. A complete treatise on colloidal gold was published in 1718 by Hans Heinrich Helcher[3]. In this treatise, this philosopher and doctor stated that the use of boiled starch in its drinkable gold preparation noticeably enhanced its stability.

These ideas were common in the 18th century, as indicated in a French dictionary, dated 1769[4], under the heading "or potable", where it was said that "drinkable gold contained gold in its elementary form but under extreme sub-division suspended in a liquid". In 1794, Mrs. Fuhlame reported in a book[5] that she had dyed silk with colloidal gold. In 1818, Jeremias Benjamin Richters suggested an explanation for the differences in color shown by various preparation of drinkable gold[6]: pink or purple solutions contain gold in the finest degree of subdivision, whereas yellow solutions are found when the fine particles have aggregated.

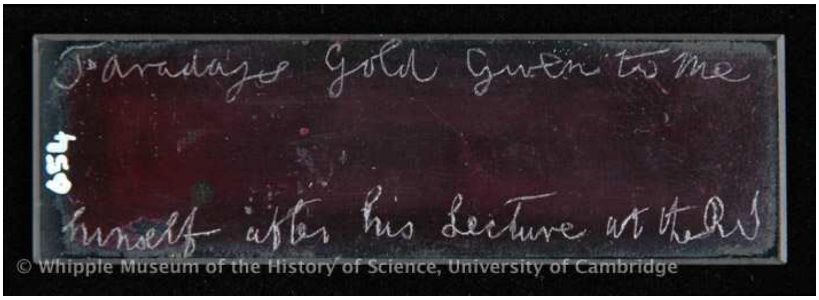

© Whipple Museum of the History of Science, University of Cambridge

FIGURE 1.2. *Faraday's colloidal gold, dispersed on a glass slide, recovered after a lecture, probably in 1858.*

In 1857, Faraday reported the formation of deepred solutions of colloidal gold by reduction of an aqueous solution of chloroaurate ($AuCl4^-$) using phosphorus in CS_2 (a two-phase system) in a well-known work (***FIGURE 1.2***). He investigated the optical properties of thin films prepared from dried colloidal solutions and observed reversible color changes of the films upon mechanical compression (from bluish-purple to green upon pressurizing)[7]. The term "colloid" (from the French, *colle*) was coined shortly thereafter by Graham, in 1861[8]. Although the major use of gold colloids in medicine in the Middle Ages was perhaps for the diagnosis of syphilis, a method which remained in use until the 20th century, the test is not completely reliable[9-11]. In the 20th century, various methods for the preparation of gold colloids were reported and reviewed[11-17]. In the past decade, gold colloids have been the subject of a considerably increased number of books and reviews[15-34], especially after the breakthroughs reported by Schmid[17,19,21] and Brust et al.[22,27]

1.2.2 Synthetic Methods for Gold Nanoparticles

Among the conventional methods of synthesis of AuNPs by reduction of gold(III) derivatives, the most popular one for a long time has been that using citrate reduction of $HAuCl_4$ in water, which was introduced by Turkevitch in 1951[12]. It leads to AuNPs of ca. 20 nm. In an early effort, reported in 1973 by Frens[13], to obtain AuNPs of prechosen size (between 16 and 147 nm) via their controlled formation, a method was proposed where the ratio between the reducing/stabilizing agents (the trisodium citrate-to-gold ratio) was varied. This method is very often used even now when a rather loose shell of ligands is required around the gold core in order to prepare a precursor to valuable AuNP-based materials.

1.2.3 The Brust-Schiffrin Method

Schmid's cluster $[Au_{55}(PPh_3)_{12}C_{16}]$, reported in 1981, long remained unique with its narrow dispersity (1.4 ± 0.4 nm) for the study of a quantum-dot nanomaterial, despite its delicate synthesis[28]. The stabilization of AuNPs with alkanethiols (***FIGURE 1.3***) was first reported in 1993 by Mulvaney and Giersig, who showed the

possibility of using thiols of different chain lengths and their analysis[29a]. The Brust-Schiffrin method for AuNP synthesis, published in 1994, has had a considerable impact on the overall field in less than a decade, because it allowed the facile synthesis of thermally stable and air-stable AuNPs of reduced dispersity and controlled size for the first time (ranging in diameter between 1.5 and 5.2 nm).

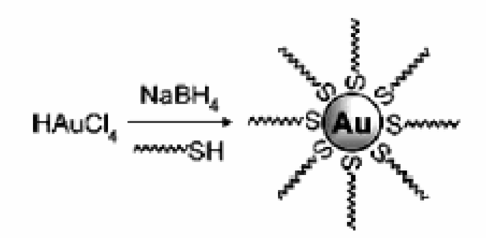

***FIGURE 1.3**. General scheme for the synthesis of thiol-capped AuNPs.*

Indeed, these AuNPs can be repeatedly isolated and redissolved in common organic solvents without irreversible aggregation or decomposition, and they can be easily handled and functionalized just as stable organic and molecular compounds. The technique of synthesis is inspired by Faraday's two-phase system[7] and uses the thiol ligands that strongly bind gold due to the soft character of both Au and S[30]. $AuCl4^-$ is transferred to toluene using tetraoctylammonium bromide as the phase-transfer reagent and reduced by $NaBH_4$ in the presence of dodecanethiol[30a]. The organic phase changes color from orange to deep brown within a few seconds upon addition of $NaBH_4$:

$$AuCl_4^-(aq) + N(C_8H_{17})_4^+(C_6H_5Me) \rightarrow N(C_8H_{17})_4^+AuCl_4^-(C_6H_5Me)$$

$$mAuCl_4^-(C_6H_5Me) + nC_{12}H_{25}SH(C_6H_5Me) + 3me^- \rightarrow$$

$$\rightarrow 4mCl^-(aq) + [Au_m(C_{12}H_{25}SH)_n](C_6H_5Me)$$

The TEM micrographs showed that the diameters were in the range 1-3 nm, with a maximum in the particle size distribution at 2.0-2.5 nm, with a preponderance of cuboctahedral and icosahedral structures. Larger thiol/gold mole ratios give smaller average core sizes, and fast reductant addition and cooled solutions produced smaller, more monodisperse particles. A higher abundance of small core sizes (< 2 nm) is obtained by quenching the reaction immediately following reduction or by using sterically bulky ligands[31-33]. Brust et al. extended this synthesis to *p*-mercaptophenol-stabilized AuNPs in a single phase system[30b], which opened an avenue to the synthesis of AuNPs stabilized by a variety of functional thiol ligands[30,31]. Subsequently, many publications appeared describing the use of the Brust-Schiffrin procedure for the synthesis of other stable AuNPs, also sometimes called monolayer-protected clusters (MPCs), of this kind that contained functional thiols[32-35]. The proportion thiol:$AuCl4^-$ used in the synthesis controls the size of the AuNPs (for instance, a 1:6 ratio leads to the maximum average core diameter of 5.2 nm, i.e., ca. 2951 Au atoms and ca. 371 thiolate ligands; core diameter dispersity of ~ ± 10%). Murray et al. reported and studied the “place exchange” of a controlled proportion of thiol ligands by various functional thiols[35] and the subsequent reactions of these functional AuNPs[33,35].

1.2.4 Other Ligands and Methods

The Brust biphasic method of synthesis has been extended to many other interesting, organosoluble ligands, like phosphines (PPh_3, TOPO), that prove to be a valuable alternative to thiols. Also microemulsions involving the presence of amphiphiles as surfactants or block copolymers, in the presence or in the absence of thiol ligands, have been effectively used to obtain stable water- or oil-soluble AuNPs. The syntheses involve a two-phase system with a surfactant that causes the formation of the microemulsion or the micelle maintaining a favorable microenvironment, together with the extraction of metal ions from the aqueous phase to the organic phase. This is an advantage over the conventional two-phase system. This dual role of the surfactant and the interaction between the thiol and the AuNP surface control the growth and stabilization of the AuNP or nanocrystal, yielding a narrow size distribution.

1.3 The Sol-Gel Process

***FIGURE 1.4**. Liesegang rings.*

In 1846, M. Ebelmen [36,37] observed that under the influence of atmospheric humidity a silicon alkoxide changed from a clear liquid into a transparent solid which on heating formed silicon dioxide, in the form of a "glass-like material" [36]. Fibers could be drawn from the viscous gel [37], and even monolithic optical lenses or composites formed [37]. The precise and detailed description of his observations includes all aspects of what we now call sol-gel processes. In these processes a molecular solution is converted by a chemical reaction to a sol which reacts further to form a gel, which on firing gives a polymeric inorganic solid. However, extremely long drying times, even of one year or more were necessary to avoid the silica gels fracturing into a fine powder, and consequently there was little technological interest.

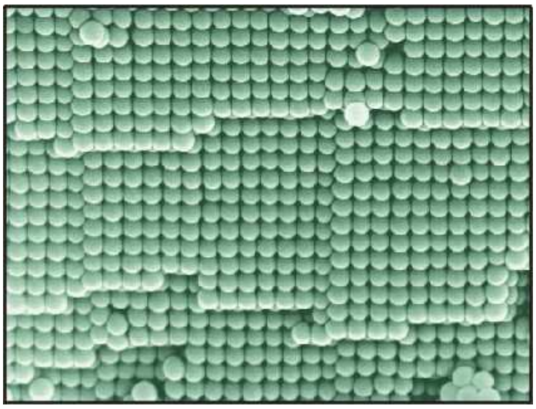

***FIGURE 1.5**. Monodisperse silica spheres synthesized with Stober method [15].*

For a period from the late 1800s through the 1920s gels became of considerable interest to chemists stimulated by the phenomenon of Liesegang rings [38,39] (***FIGURE 1.4***) formed from gels. Many noted chemists, including Ostwald [40] and Lord Rayleigh [41], investigated the problem of the periodic precipitation phenomena that lead to the formation of Liesegang's rings and the growth of crystals from gels. A huge volume of descriptive literature [42-44] resulted from these studies but a relatively sparse understanding of the physical-chemical principles [39].

Roy and co-workers [45-48] recognized the potential for achieving very high levels of chemical homogeneity in colloidal gels and used the sol-gel method in the 1950s and 1960s to synthesize a large number of novel ceramic powder methods. During the same period Iler's [49] pioneering work in silica chemistry led to the commercial development of colloidal silica powders, DuPont's colloidal Ludox spheres. Stober et al. [50] extended Iler's findings to show that using ammonia as a catalyst for tetraethoxysilane (TEOS) hydrolysis reaction could control both the morphology and size of the powders, yielding the so-called Stober spherical silica powder (***FIGURE 1.5***). Some of the fundamental parameters which were individuated and optimized during its development are the ones that characterize modern sol-gel chemistry, such as the initial concentration of water and catalyst, the type of the silicon alcoxide (methyl, ethyl, pentyl, esters, etc.) and alcohol (methyl, ethyl, butyl, pentyl) mixture used [50], and reactant temperature [51]. Anyway, one of the most intriguing aspects of sol-gel processes consists in the wide variety of parameters influencing the final product and in their often not straightforward interactions, thereby determining the fine tunability that makes it an extremely powerful technique.

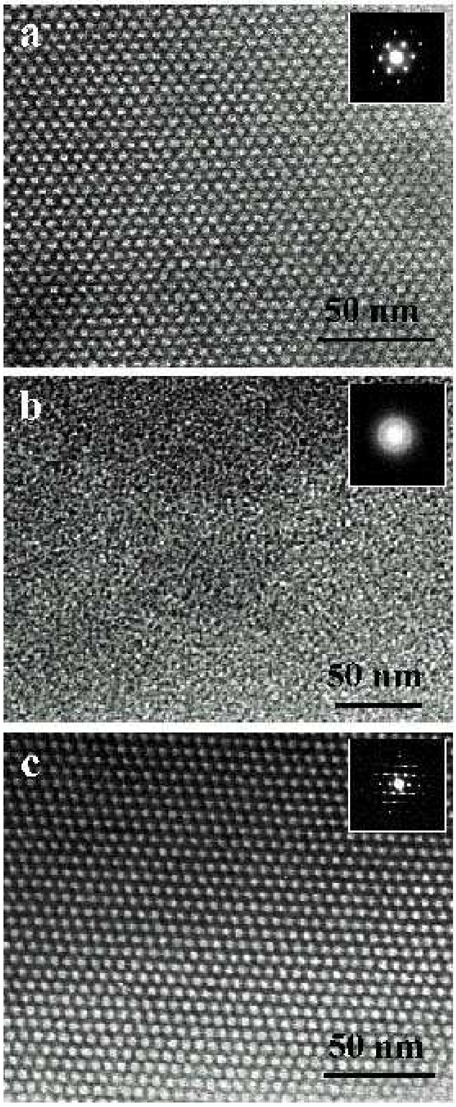

FIGURE 1.6. *Mesoporous titania.*

Since that time an increasing number of published work has explored many of the mentioned features either aiming at pure research or to technological application. An enormous range of colloidal powders [52-55] with controlled size and morphologies has been produced, including oxides (TiO_2, α-Fe_2O_3, Fe_3O_4, $BaTiO_3$, Cr_2O_3, CeO_2, etc.), hydroxides (AlOOH, FeOOH, $Cr(OH)_3$, etc.), carbonates ($Cd(OH)CO_3$, $Ce_2O(CO_3)_2$, Ce(III)/$YHCO_3$), sulfides (Zn, CdS), (Pb, CdS), and even coated and doped particles with a variety of combination limited only by the technological interest.

In the last two decades, the same basic principles were extended by the introduction of novel precursors which carried along new elements and functionalities, opening the way to a completely new class of materials. In the late 1970s, the application of sol-gel precursors to the almost forgotten idea by Kistler [56] who in 1920s had developed the first aerogels starting form traditional precursors, made them applicable in many different fields: from the detection and production of Cherenkov radiation in particle physics (2700 liters of silica aerogel were altogether used at DESY in Hamburg and at CERN in Geneva) and the collection of cosmic dust in the Space Shuttle missions, to acoustic and thermal insulation materials, passing through the development of record-low density for solid state materials of 0.003 g/cm^3 [57].

A variety of coatings and thin films have also been studied. Of particular importance are the reflective and anti-reflective coatings of indium tin oxide (ITO) and related compositions applied to glass window panes to improve insulation characteristics [58]. Anti-scratch and protective coatings have been developed as well for many applications, including optical and magnetic disks. A further possibility is given by the introduction on the surface of organic groups which have led to thin films with controlled hydrophilicity and wettability. On the other hand, the addition of surfactants to the reaction pot has led to the development of mesoporous materials [59] (***FIGURE 1.6***), which are indeed very promising for catalytic, energetic and optical applications. A wider survey as well as a detailed analysis of the mentioned materials goes beyond the purpose of this introduction, which intended to disclose the exciting potential of a technique that at present has already many technological applications. The key motivations for sol-gel processing are primarily the potentially higher purity and homogeneity and lower processing temperatures associated with sol-gels compared with traditional glass melting or ceramic powder methods. The main goal is to control the surfaces and interfaces of materials during the earliest stages of formation, since the long-term reliability of a material is usually limited by localized variations in the physical chemistry of the surfaces or interfaces within the material itself. In order to achieve such homogeneity, starting materials should be soluble in organic solvents, and ideally they should be easily convertible into the corresponding oxide or equivalent inorganic polymer by chemical and/or physical methods. Molecular precursors that combine both properties are metal alkoxides of the general formula $M^N(OR)_n$ where M not only means metal atoms but also several other elements like silicon, boron or phosphorous. Since metal alkoxides of nearly all elements are known [60] and since most of them are commercially available in high purity they are still the main starting materials.

1.3.1 The Sol-Gel Process Steps

The very nature of the Sol-Gel process is undoubtedly contained in its own name, which suggests some sort of transition from a sol to a gel as the key step.

Sols are commonly defined [61] as dispersion of colloidal particles in a liquid. Colloids are solid particles with a diameter varying from few nanometers to hundreds, the definition being consistent with the displayed properties of Brownian motion and for which we can assume the gravitational effects to be neglectable. A gel is an interconnected, rigid network with pores of submicrometer dimensions and polymeric chains whose average length is greater than a micrometer. The term gel embraces a diversity of combination of substances that can be classified in four categories as classified by Flory [62]: 1) well-ordered lamellar structures; 2) covalent polymeric networks, completely disordered; 3) polymer networks formed through physical aggregation, predominantly disordered; 4) particular disordered structures. Such a variety of structures is in principle determined by many different synthetic routes, for instance involving the gelation of a colloidal dispersion or the formation of alkyl-halide byproducts in anhydrous polymerizations. This work deals anyway with typically hydrous sol-gel reactions, which are generally divided into two steps: hydrolysis of metal alkoxides to produce hydroxyl groups, followed by polycondensation of the hydroxyl groups and residual alkoxy groups to form a three-dimensional network (***FIGURE 1.7***).

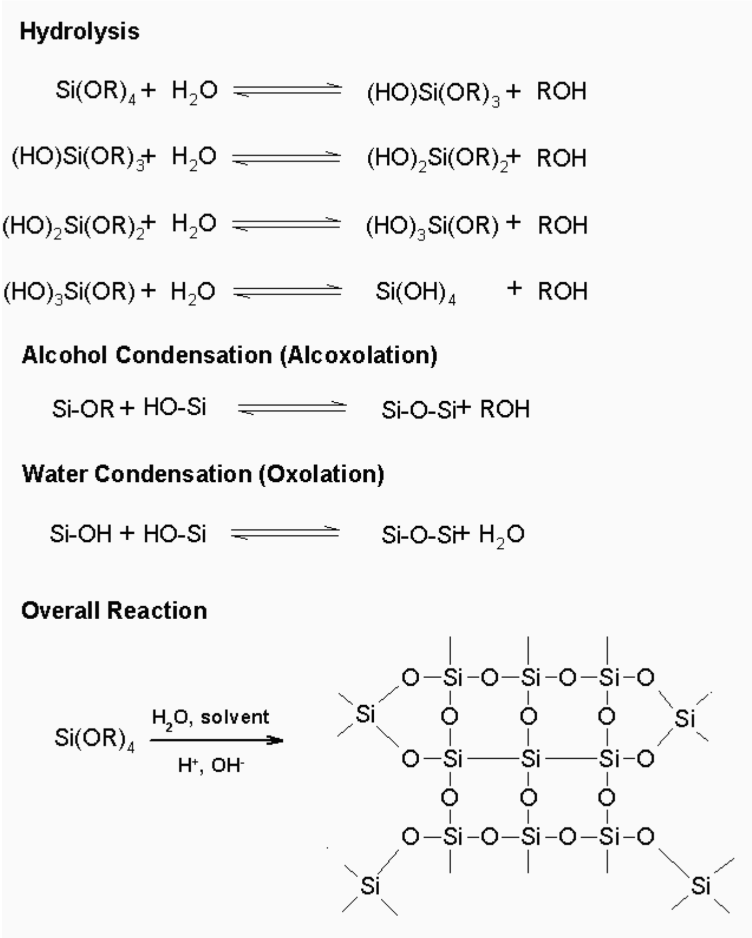

FIGURE 1.7*. Main sol-gel reactions for silicon alkoxides.*

The sol to gel transition, or gelation point, is easy to observe qualitatively and to define in abstract terms, but extremely difficult to characterize and measure analytically. A sol becomes a gel when it can support a stress elastically, but there is no activation energy that can be measured, nor one can precisely define at what time, t_{gel}, the sol changes from a viscous fluid to an elastic gel. The change is gradual as more and more interconnected structures form throughout the sample, and all the subsequent stages of processing depend on the initial structure of the wet gel formed in the reaction bath during gelation. The sol-gel process generally starts with alcoholic or other low molecular weight organic solutions of monomeric, metal or semimetal alkoxide precursors $M^N(OR)_n$, where M represents a network-forming element such as Si, Ti, Zr, Al, B, etc., and R is typically an alkyl group (C_xH_{2x+1}), and water.

Once the hydrolysis reaction has been initiated, both the hydrolysis and condensation reactions occur simultaneously by nucleophilic substitution (SN) mechanisms that which involve three steps: nucleophilic addition (AN), proton transfer within the transition states, and removal of the protonated species as either alcohol or water.

The hydrolysis and condensation reactions in the sol-gel process generally start with the nucleophilic addition of hydroxylated groups onto the electrophilic metal atoms which results in an increase of the coordination number of the metal atom in the transition state. As described by Sanchez and Ribot [63], the degree of reactivity of a given metal or semi-metal atom of an alkoxide is not due only to the electrophilic nature but rather is more a function of degree of unsaturation.

The extent of unsaturation is given as (N - Z), where N is the coordination number of the atom in the stable oxide network and Z is the oxidation state. Table 1.1 lists the electronegativity and the degree of metal unsaturation for a few metal alkoxides. It is noted that silicon has a low electrophilicity and zero degree of unsaturation. Therefore, silicon alkoxides are less reactive. On the other hand, non-silicate metal alkoxides, including elements such as Ti, Zr, Al, and B with higher unsaturation, all have much higher reactivity than silicon. They are so sensitive to moisture, even in the absence of a catalyst, that precipitation of the oxide will generally occur as soon as water is present. For example, the hydrolysis and condensation rates of titanium butoxide are much faster than that of tetraethoxysilane (TEOS). The sequence of reactivity is expressed as follows [60,64]:

$$Zr(OR)_4,\ Al(OR)_3 > Ti(OR)_4 > Sn(OR)_4,\ Si(OR)_4$$

There are several ways to control the reactivity of metal alkoxide species. For instance, chemical additives, such as glycols, organic acids (acetic acid), βdicarbonyl ligands (ethyl or methyl acetylacetate), have often been used as chelating ligands to slow the hydrolysis and condensation reactions of non-silicate metal alkoxides [65,66]. After forming a complex with the chelating ligand, the species between metal and chelating agent is less easy to hydrolyze [67]. However, the chelating ligand will normally remain which alters the structure of the final network.

Alkoxide	χ	N	Z	N-Z
$Si(OPr^i)_4$	1.90	4	4	0
$Sn(OPr^i)_4$	1.96	6	4	2
$Ti(OPr^i)_4$	1.54	6	4	2
$Zr(OPr^i)_4$	1.33	7	4	3
$Ce(OPr^i)_4$	1.12	8	4	4
$Al(OPr^i)_3$	1.61	6	3	3

TABLE 1.1. *Electronegativity (χ), coordination number (N), oxidation state (Z) and degree of unsaturation (N - Z) for some metals.*

As can be seen from ***FIGURE 1.7***, both the hydrolysis and condensation steps generate low molecular weight byproducts such as alcohol and water. These small molecules must be removed from the system: in particular, when the pore liquid is removed as a gas phase from the interconnected solid gel network under hypercritical conditions, the network does not collapse and a low density aerogel is produced. When the pore liquid is removed at or near ambient pressure by thermal evaporation (drying) and shrinkage occurs, the monolith is termed xerogel. The high porosity of the gelled structure determines large amounts of physically adsorbed water that requires temperatures up to 180 °C to be evacuated. Anyway, the dried gel still contains a very large concentration of chemisorbed hydroxyls on the surface of the pores, and a thermal treatment in the range of 500-800 °C is necessary to desorb the hydroxyls and thereby decrease the contact angle and the sensitivity of the gel to rehydration stresses, thus stabilizing the gel. While these temperature ranges represent no particular challenge in the treatment of inorganic glasses, they are certainly prohibitive for organic polymers, whose range of stability rarely exceeds the 200-250 °C limit even in hybrid materials [68].

The heat treatment of an inorganic gel at elevated temperatures substantially reduces the number of pores and their connectivity due to viscous-phase sintering, in a process that is termed densification. The density of the monolith increases and the volume fraction of the porosity decreases during sintering up to the formation of a dense glass when all pores are eliminated. It's probably the most crucial and delicate step in the whole process, and as mentioned above it's the factor that has prevented an earlier technological development of the sol-gel method.

1.3.2 Silica

In the case of silicon based metal alkoxides, the hydrolysis and condensation reactions typically proceed with either an acid or base as catalyst. Therefore, the structure and morphology of the resulting network strongly depend on the nature of the catalyst and the pH of the reaction.

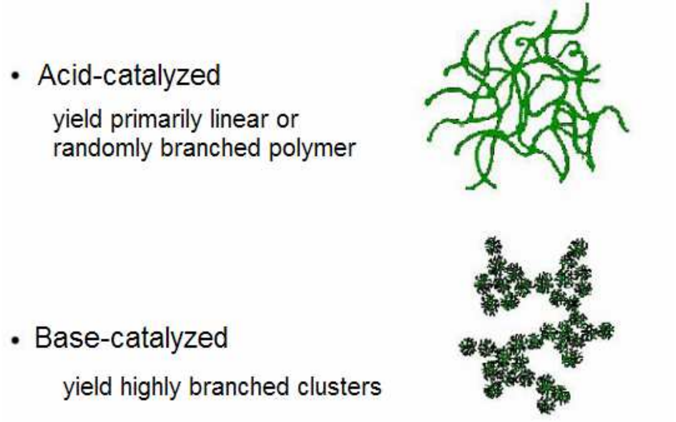

FIGURE 1.8. *Different catalysis products for silicon alkoxides.*

A low pH favors the protonation of an alkoxy group oxygen atom, reducing the electron density on the silicon atom and making it a suitable site for a nucleophilic attack from neutral species. The concertated mechanism (S_N2) implies the attack of a water molecule with the protonated alkoxy group leaving as an alcohol. The resulting hydrolysis rate is high with respect to that of condensation, thus promoting the development of more linear or polymer-like molecules in the initial stages. For a pure metal alkoxide system, this leads to the formation of high-density, low fractal dimension structures.

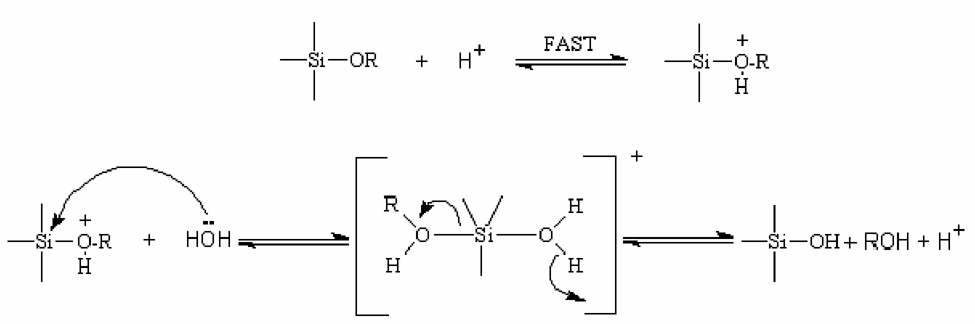

FIGURE 1.9. Acid catalysed hydrolysis.

On the other hand, base catalysis (pH > 6) involves a nucleophilic attack of an OH^- group on the silicon atom, causing again the inversion of the coordination tetrahedron with RO^- as the leaving group. It results in a higher condensation rate, basing on the assumption of a nucleophilic attack of penta-coordinated, hydrolyzed or partially hydrolyzed silicon anions to hydrolyzed or partially hydrolyzed silicon intermediates. Therefore, this environment tends to produce more of a dense-cluster growth leading to dense, colloidal particulate structures [69-72].

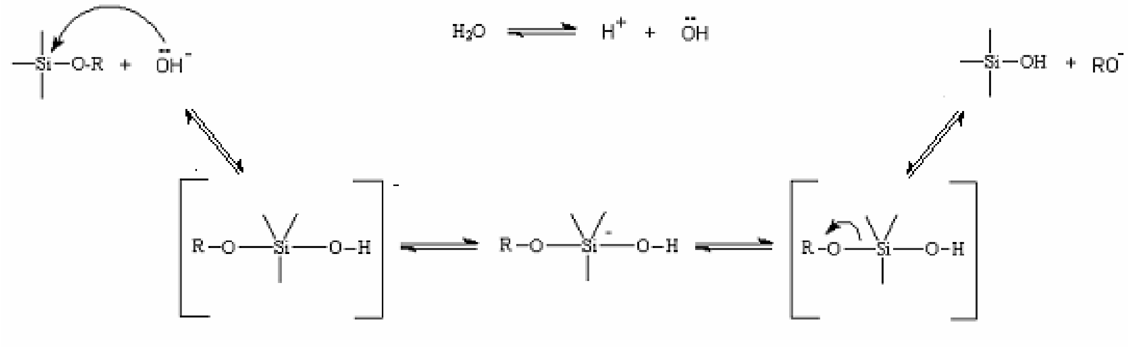

FIGURE 1.10. Base catalysed hydrolysis.

In addition to the pH of the reaction, the size of the alkoxy group can also influence the hydrolysis and condensation reactions through a steric or leaving group stability effect. For example, species such as tetramethoxysilane (TMOS) tends to be more reactive than tetraethoxysilane (TEOS). Furthermore, the Si/H_2O ratio plays a major role since it influences the degree of hydrolyzation: when not all the Si-O bonds are hydrolyzed oligomers of different shapes and lengths, or building blocks, are formed, and their condensation leads to different final structures. The various intermediate stages show different reactivities with respect to hydrolysis itself because of the inductive effects of the substituents attached to the central silicon atom, which are schematized in ***FIGURE 1.11***.

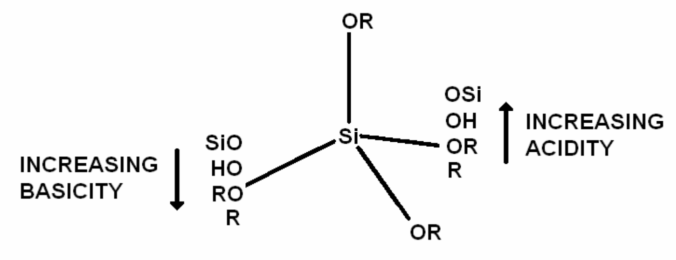

FIGURE 1.11. *Inductive effects of substituents attached to silicon.*

Another key factor is represented by the solvent system, since polarity, dipole moment and proticity affect the strength of the electrostatic interactions and the stability of the intermediates, enhancing or reducing the efficiency of the catalysis both during hydrolysis and condensation.

1.4 Aromatic Polyimides

Aromatic polyimides are considered to be a class of high-performance polymers, and they have found a wide range of applications in advanced technologies[73]. They were developed in the 1960s thanks to intensive research on heatresistant polymers, and soon became highly important because of their excellent thermal stability, along with good mechanical and electrical properties. On the other hand, it was also soon realized that fabrication of aromatic polyimides was not possible from the melt. For injection or extrusion moulding, conventional aromatic polyimides did not show suitable flow properties, and therefore special fabrication methods such as compression or sintering moulding must be applied. Furthermore, their extreme structural rigidity made them insoluble in any organic media.

Fortunately, aromatic polyimides could be used as materials because they can be prepared through a multistep process, based on the existence of soluble polymeric intermediate. Nevertheless, the transformation into polyimides at the moment of application is an approach far from being optimal in most cases, and it can be said that, for many years, aromatic homopolyimides could be successfully applied only in the form of films or coatings[73,74].

Structural modifications were early envisioned to overcome these limitations. A first improvement was outlined by preparing copolymers, which were soluble in the state of full imidation, mainly poly(ester-imide)s and poly(amide-imide)s[74,76,77]. As an alternative to these conventional copolymers, addition polyimides were developed in the 1970s as a new class of thermosetting materials. Thus, bismaleimides, bisnadimides, and end-capped thermocurable polyimides were successfully developed and marketed[78,79]. These resins were the precursors of the modern PMR (polymeric monomer reactants) formulations[80]. Further improvements in the chemistry of polyimides during the last few years have been directed towards novel, linear species that are soluble in organic solvents or melt-processable while fully imidized. Thus, changes had to be introduced in the chemical structure to adapt the behaviour and performance of these specialty polymers to the demands of the new technologies. As a consequence, a new generation of condensation polyimides has appeared, the so-called thermoplastic polyimides. A recent review on organic-soluble and/or melt-processable thermoplastic polyimides is available[81]. The very high transition temperatures and melt viscosities exhibited by most of the modern aromatic polyimides do not really permit their processing in the melt by the conventional methods of extrusion, compression and injection moulding, so when a polyimide is said to be processable this definition includes also some form of solubility.

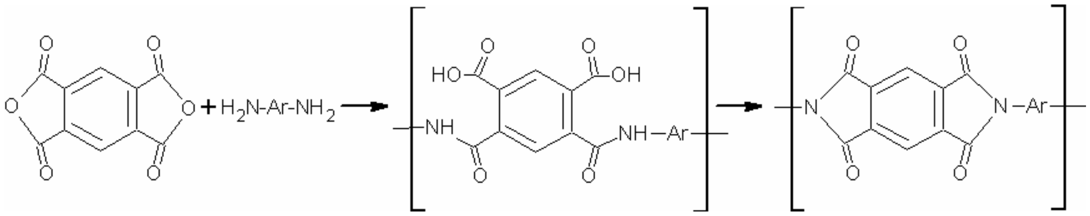

FIGURE 1.12. Two-step method for the synthesis of aromatic polyimides.

Since the commercialization of Kapton® polyimide film by DuPont, more than 30 years ago, a great number of polyimides have been described covering a very wide range of properties. However, the properties of Kapton, the polyimide made from pyromellitic dianhydride and 4,4'-oxydianiline, are actually unique, and no other commercial polyimide has challenged the properties-price balance that this high-temperature film offers. Thus, all the efforts dedicated to design and to produce novel aromatic polyimides have concentrated on the processability and on the improvement of some specific properties that are crucial in advanced technologies, such as photosensitivity, transparency, lack of colour, light transmission, dimensional stability, electrical conductivity, moisture absorption, planarization, adhesion, chemical resistance or etching capabilities. As mentioned before, the first generation of fully aromatic homopolyimides, could be used in a few applications because they had to be applied in the form of soluble polyamic acids, and this limited the materials to be transformed almost exclusively into films or coatings[74,82]. They all had to be synthesized by a two-step method, as exemplified for an aromatic polyimide from pyromellitic dianhydride in ***FIGURE 1.12***. The method involves the synthesis of a soluble polyamic acid, which, after shaping, can be converted to the related polyimide by a thermal or a chemical treatment[75,76,83-85]. The difficulties in processing conventional aromatic polyimides are due to the inherent molecular features of aromatic polyimides, which is particularly true for the most popular of them: polypyromellitimides. Molecular stiffness, high polarity and high intermolecular association forces (high density of cohesive energy) make these polymers virtually insoluble in any organic medium, and shift up the transition temperatures to well above the decomposition temperatures.

Thus, the strategies to novel processable aromatic polyimides have focussed on chemical modifications, mainly by preparing new monomers, that provide less molecular order, torsional mobility and lower intermolecular bonding. Of the various alternatives to design novel processable polyimides, some general approaches have been universally adopted:

- introduction of aliphatic or another kind of flexible segments, which reduce chain stiffness;
- introduction of bulky side substituents, which help for separation of polymer chains and hinder molecular packing and crystallization;
- use of enlarged monomers containing angular bonds, which suppress coplanar structures;
- use of 1,3-substituted instead of 1,4-substituted monomers, and/or asymmetric monomers, which lower regularity and molecular ordering;
- preparation of co-polyimides from two or more dianhydrides or diamines.

However, factors leading to better solubility or lower T_g or T_m in a polymer often conflict with other important requirements, such as mechanical properties, thermal resistance or chemical resistance. Therefore, an adjusted degree of modification should be applied to optimize the balance of properties. In this thesis, polyimides carrying fluorinated, bulky and flexible functional groups have been used to obtain an easily processable and further modifiable material.

1.4.1 Polyimides with Bridging Flexible Functional Groups

Introducing flexible linkages into polymer backbones is a general approach, used mainly to lower transition temperatures and to improve solubility of intractable aromatic polymers. Polyimides with flexible linkages have been known from the advent of high temperature aromatic polyimides. In fact, most of the commercial, fully aromatic polyimides contain ketone or ether linkages in their repeating units, and early works in the field soon demonstrated that dianhydrides having two phthalic anhydride moieties joined by bonding groups gave more tractable polyimides[86]. Many different linkages have been introduced with these purposes, but the most succesful so far have been -O-, C=O, -S-, -SO2-, -C(CH3)2-, -CH2-, -CHOH-, and -C(CF3)2- . A selection of these monomers is shown in ***FIGURE 1.13***.

These bonding groups may be located on the dianhydride, on the diamine or on both monomers, or they can even be formed during the polycondensation reaction, when some functional monomers containing preformed phthalimide groups are used as condensation monomers. The presence of flexible linkages has a dramatic effect on the properties of the final polymers.

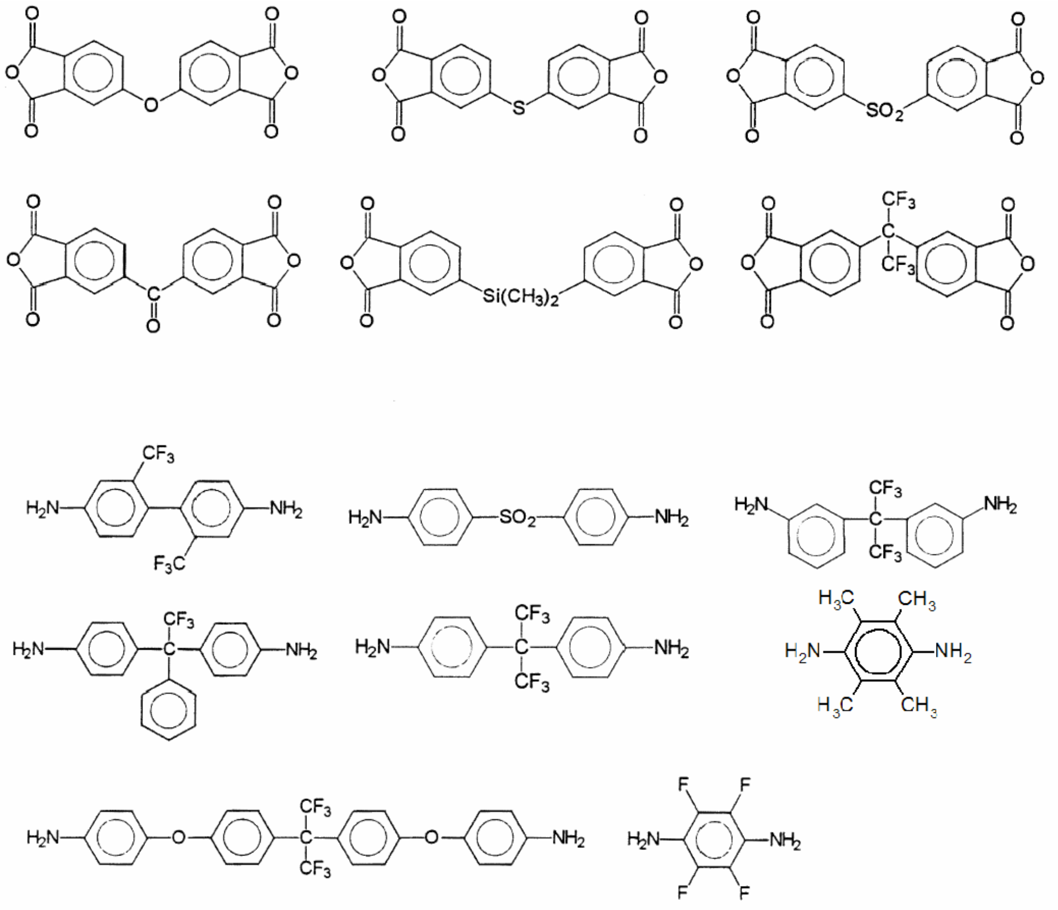

FIGURE 1.13. *Some of the monomers used in the synthesis of non-conventional polyimides.*

First, “kink” linkages between aromatic rings or between phthalic anhydride functions cause a breakdown of the planarity and an increase of the torsional mobility. Furthermore, the additional bonds mean an enlargement of the repeating unit and, consequently, a separation of the imide rings, whose relative density is actually responsible for the polymer tractability. The suppression of the coplanar structure is maximal when voluminous groups are introduced in the main chain, for instance sulfonyl or hexafluoroisopropylydene groups, or when the monomers are enlarged by more than one flexible linkage. The combination of those dianhydrides and diamines, and also the combination of some of them with conventional rigid monomers like benzenediamines, benzidine, pyromellitic dianhydride or biphenyldianhydride, offer a major possibility of different structures with a wide spectrum of properties, particularly concerning solubility and meltability[87-94].

However, very few of the polymers that can be synthesized combining monomers of ***FIGURE 1.13***, have been reported as melt-processable, although many of them are soluble in organic highly polar solvents. All of them show high glass transition temperatures, commonly over 250 °C, and, theoretically, they can develop crystallinity upon suitable thermal treatment, mainly those containing polar connecting groups. Thus, depending on the nature of the bridging groups, polyimides can be prepared that show an acceptable degree of solubility in organic solvent. Hexafluoropropylidene, carbonyl and sulfonyl are the groups most advantageously incorporated concerning processability. This is due to the relatively large volume of these groups, and to the conformational characteristics imparted by them to the polymer chain. The combination of non-planar dianhydrides and non-planar, *meta*-oriented aromatic diamines containing flexible linkages provides the structural elements needed for solubility and melt processability[81,95-97].

A rational approach to improve tractability of aromatic polyimides consists of extending the length of the diamine and/or the dianhydride by incorporating more phenylene rings and more connecting flexible groups. Monomer enlargement contributes to the separation of the very polar, rigid phthalimide groups, and provides an improvement of the chain mobility by the presence of additional bonds with lower rotational barriers.

Using the same chemical functions previously mentioned for bridged diamines and dianhydrides, a wide variety of new enlarged monomers has been prepared and used to synthesize processable polyimides[98-120]. Although very few of them have achieved commercial importance, the research effort during the last two decades to develop new monomers has enriched the chemistry of aromatic polyimides to such an extent that it would be difficult to find another field of macromolecular chemistry where the investigations have produced a similar variety of new species with such a wide range of properties.

1.4.2 Polyimides with Bulky Side Substituents

Structural modifications to attain soluble aromatic polyimides have also been carried out by introducing bulky substituents, aryl or heterocyclic rings. Since the pioneering works of the Russian researchers, many attempts have been made to prepare new monomers, diamines and dianhydrides, with bulky pendent groups for novel processable polyimides. By far, the most promising species are those containing phenyl pendent groups. The phenyl group does not introduce any relevant weakness regarding thermal stability, and provides a measure of molecular irregularity and separation of chains very beneficial in terms of free volume increase and lowering of the cohesive energy density[121-126]. Fluorene diamines and the so-called “cardo” monomers also mean valuable alternatives for the preparation of processable polyimides[127,128]. On the other hand, the presence of the bulky side substituents in polyimides or in any other linear polymer causes a lowering of the chain's torsional mobility and generally an increment of the glass transition temperature[129-132].

1.4.3 Fluorinated Polyimides

One of the most attractive and successful attempts in attaining processable aromatic polyimides is the introduction of fluorine atoms in the polymer structure, either as substituents of carbon atoms on the polymer backbone (as mentioned before for perfluoroalkane containing polyimides), or as perfluoromethyl or perfluoroalkyl side substituents. The most popular approach has been the introduction of the hexafluoroisopropylidene group in the main chain as a bulky separator group in the dianhydride monomer or in the diamine one[106].

The presence of trifluoromethyl groups and, in general, the substitution of fluorine for hydrogen, causes a dramatic change of properties. The combination of electronic and steric effects reduces the ability for interchain interactions and, particularly, hinders the formation of charge transfer complexes, which is a major factor of molecular packing and intractability in aromatic polyimides. Furthermore, the C-F bond is a high-energy bond, so that polyimides containing fluorine are in general polymers with high T_g and excellent thermal properties, comparable to those of the conventional aromatic polyimides. They show some improved properties, such as:

- low dielectric constant
- high optical transparency
- excellent mechanical properties
- low moisture absorption
- increased solubility
- low optical loss and low refractive index.

This excellent balance of properties has made fluorinated polyimides very attractive for some applications in advanced technologies, for instance:

- high performance structural resins
- thermally stable coatings and films
- polymeric membranes for gases separation
- polymeric waveguides, and other electronic and optoelectronic applications.

Dozens of monomers, mainly diamines, have been described as suitable reactants for the synthesis of fluorinated polyimides in last years. Soluble and meltable polyimides have been prepared by combination of these with fluorinated and non-fluorinated monomers, and the range of structures achieved has already been so extended that it appears to be unlimited. They can be amorphous or semicrystalline, and have been processed by virtually any possible processing method.

Fluorinated polyimides have achieved great importance as barrier materials during the last few years. Many experimental polyimides prepared from fluorine-containing monomers, mainly novel diamines, show an advantageous balance of permeability and selectivity for technical gases and vapours, which makes them very attractive for the fabrication of permselective membranes[133]. This is an application field showing very rapid expansion, where there exists a strong demand for new polymeric materials, and where soluble aromatic polyimides are considered as a real alternative[134–140].

1.5 Hybrid Materials

A hybrid is a material in which the organic and inorganic phase are mixed at a submicroscopic level, determining phase homogeneity. Even if the sol-gel process is mainly based on inorganic polymerization reactions that lead to the formation of inorganic materials such as ceramics or glasses, its unique low-temperature processing characteristic provides an excellent opportunity to incorporate organic moieties, typically unsuitable to the traditional ceramic processing methods because of their low thermal stability. Furthermore, having molecular precursors allows an efficient mixing at a nanoscale level, once that the proper solvent and physical conditions have been chosen. A comparison between some of the most significant properties of organic polymers and glass is given in ***TABLE 1.2***.

Property	Polymers	Glass
Refractive index (RI)	1.40 ÷ 1.65	1.35 ÷ 1.95
Dn/DT(10-6/°C)	-140 to -85	-8 to –6
RI homogeneity	10^{-4}	10^{-6}
Thermal expansion (10-7/°C)	150 ÷ 700	-10 to 160
Young Modulus (Mpa)	1÷10	40 ÷ 130
Thermal stability (°C)	90 ÷ 250	450 ÷ 950
Scratch resistance	Low	High
Processing easiness	High	Moderate

TABLE 1.2. *Comparison between the properties of polymers and glass.*

There are many ways by which organic and inorganic phases can be mixed via sol-gel techniques, by incorporating different starting inorganic and organic components with varied molecular structure (in the following schemes, ◇ represents an inorganic polymerizable moiety, such as a silane, and ▲ represents an organic group which in some cases can be polymerised. ▶∿◇ represents the situation in which the organic and inorganic species are covalently bonded, usually through a ≡Si–C– bond):

(1) Hybrid networks can be synthesized by using low molecular weight organoalkoxysilanes as one or more of the precursors for the sol-gel reaction in which organic groups are introduced within an inorganic network through the ≡Si–C– bond [141-143].

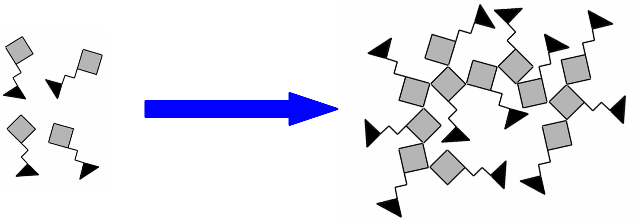

(2) Organic/inorganic hybrid network materials can also be formed via the co-condensation of functionalized oligomers or polymers with metal alkoxides in which chemical bonding is established between inorganic and organic phases [144-146].

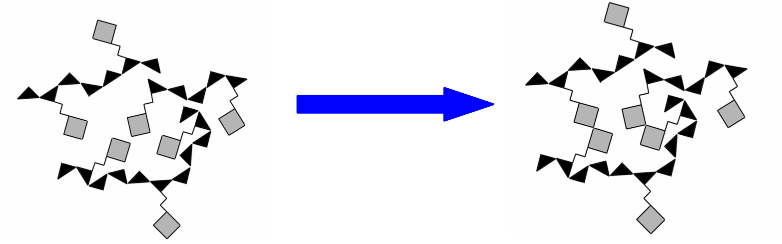

(3) A hybrid material can also be synthesized through the in situ formation of inorganic species within a polymer matrix [147-154]. Specifically, inorganic species, generally in the form of particles with a characteristic size of a few hundred angstroms, can be generated in situ within the polymers by first swelling cross-linked, ionomeric, or crystalline polymeric host with a compatible solution containing metal alkoxides followed by the promotion of the sol-gel reaction of the inorganics. Various inorganic particles with extremely homogeneous particle size have been prepared in this manner within elastomeric or plastic matrixes [155-168]. The concept of such “in situ” generation of fillers is novel and of practical importance in terms of elastomer reinforcement [150-151].

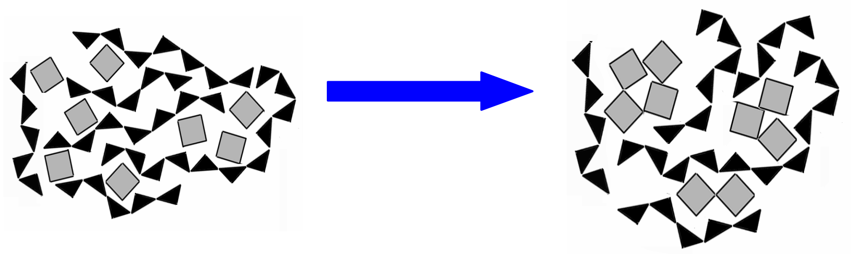

(4) Starting from the opposite direction of (3), organic/inorganic composites can be obtained by either the infiltration of previously formed oxide gels with polymerizable organic monomers or the mixing of polymers with a single or mixture of metal alkoxides in a common solvent. In the first approach, the impregnation of porous oxide gels with organics is followed by an in situ polymerization initiated by thermal or irradiation methods

[169]. In the second approach, polymers can be trapped within the oxide gel network if the hydrolysis and condensation of metal alkoxide are carried out in the presence of preformed polymers [170-172]. Optically transparent composite materials can be obtained if there is no macro- or microphase separation during both the gel forming and drying process.

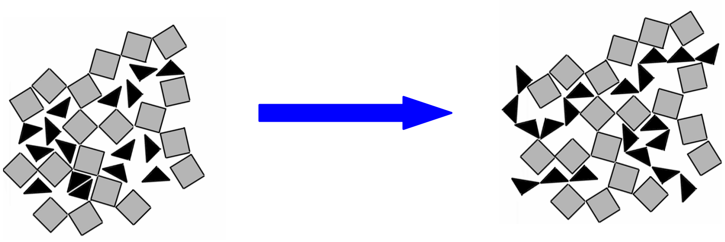

(5) Similar to approach (4), organics can also be simply impregnated or entrapped as a guest within inorganic gel matrixes (as a host). This approach has been extensively used in the incorporation of enzymes, proteins, and various organic dyes such as luminescent dyes, photochromic dyes, and nonlinear optical (NLO) dyes into an inorganic network [173-175]. The main driving force behind the intensive research activity in preparation of these types of materials is the development of new optical and bioactive materials in the application of photophysical, electrical, biotechnical, and nonlinear optical (NLO) devices [173,176].

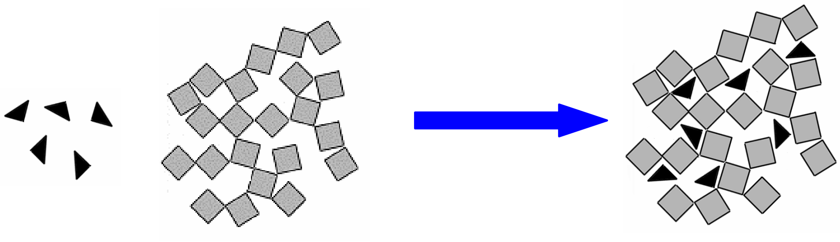

(6) Hybrid networks can also be formed by interpenetrating networks and simultaneous formation of inorganic and organic phases. By using trialkoxyslianes R'Si(OR)$_3$ as the precursors with R' being a polymerizable group such as an epoxy group, an organic network can be formed within the inorganic network by either photochemical or thermal curing of such groups, as Schmidt has demonstrated in 1984 [142].

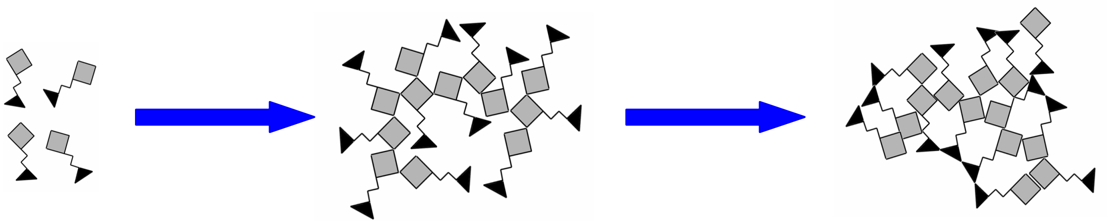

(7) An hybrid IPN can be obtained starting from the same precursors as in (6) by following the inverse polymerization order. In this case, the organic content of the final material can be varied by introducing monomers or oligomers that carry no inorganic functional groups and can be polymerized with the functionalized trialkoxysilanes. Starting from such groups, an inorganic network joining the organic chains can then be formed with a sol-gel process: in a typically anhydrous melting pot the hydrolysis/condensation reactions are catalyzed either thermally or by varying the pH of the water that needs to be added. This approach shows many advantages, especially when low-shrinking materials are required, since the initial formation of organic, linear polymeric chains allows to minimize the drying stresses during the inorganic network formation. At the same time, it is possible to tune the inorganic content to the minimum amount necessary to achieve the desired properties.

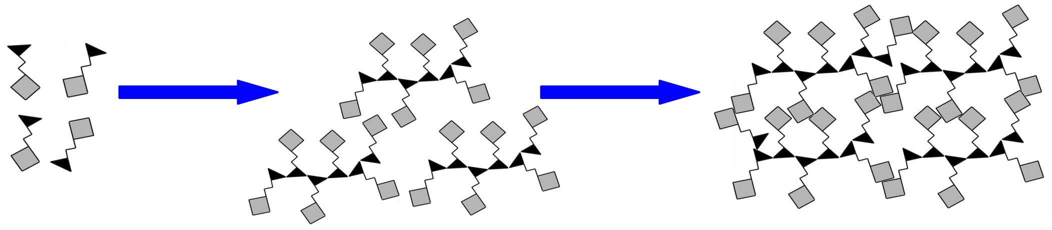

Even though many of the network systems are comprised of components having very different refractive indexes, the resulting material can often be prepared optically transparent due to the small-scale lengths over which phase separation may exist. As a result, these composite materials can find applications in many fields that are far beyond the scope of application of traditional composite materials and this is one important reason for the strong interest in the application of organic/inorganic hybrid materials. To date, the number of commercial sol-gel hybrid products is still comparatively small, but the promise of new technological uses remains. Some potential applications for these materials are as follows, as reviewed by Wen and Wilkes [177]:

(1) Scratch and abrasive-resistant hard coatings and special coatings for polymeric materials, metal, and glass surfaces.
(2) Electrical and NLO materials.
(3) Adhesives and contact lens materials.
(4) Reinforcement of elastomers and plastics.
(5) Catalyst and porous supports, adsorbents.
(6) Tunable solid-state lasers and chemical/biomedical sensors.

On the basis of the connection between the inorganic and organic phases, the organic/inorganic composite materials can be also conveniently divided into two general classes: those with chemical bonding between the two phases ((1), (2), (6),(7)) and those without ((3), (4), (5)) [178]. In the latter case, when one of the two phases is not structurally indispensable it can be in principle removed, giving rise to the concepts of molecular scaffold as in the case of mesoporous materials [24], where organic surfactants are removed after the formation of the inorganic network either thermically or chemically.

The incorporation of organic/inorganic materials into organic/oligomeric/polymeric networks by the sol-gel process makes it possible to optimize selected properties in an almost completely independent manner. Specifically, the introduction of inorganic groups into an organic network leads to new structure-property variation, thereby promoting new potential applications for the resulting composite materials. Linear and non-linear optical properties can be achieved or improved by introducing metallic clusters or semiconductor nanocrystals while maintaining optical transparency. At the same time this results in a significative improvement of the mechanical properties, as for instance the scratching hardness or the elastic modulus. Furthermore, the permeability of organic polymers to gas molecules and ions suggests interesting applications for sensors, catalysis or active membranes.

1.6 DNA Nanotechnology

TheWatson–Crick proposal for the structure of DNA is now over fifty years old. This proposal provided the chemical basis for understanding genetics; indeed, the last half-century of biology has been devoted to the exploitation of the implications of this model. The impact of DNA on society is just beginning to be felt, with the culmination of the Human Genome Project, and in the forensic and medical applications of DNA analysis. Regardless of its central importance in biology, the applications of DNA are not limited to the biological sciences. DNA is a molecule, and it functions successfully as genetic material because of its chemical properties.

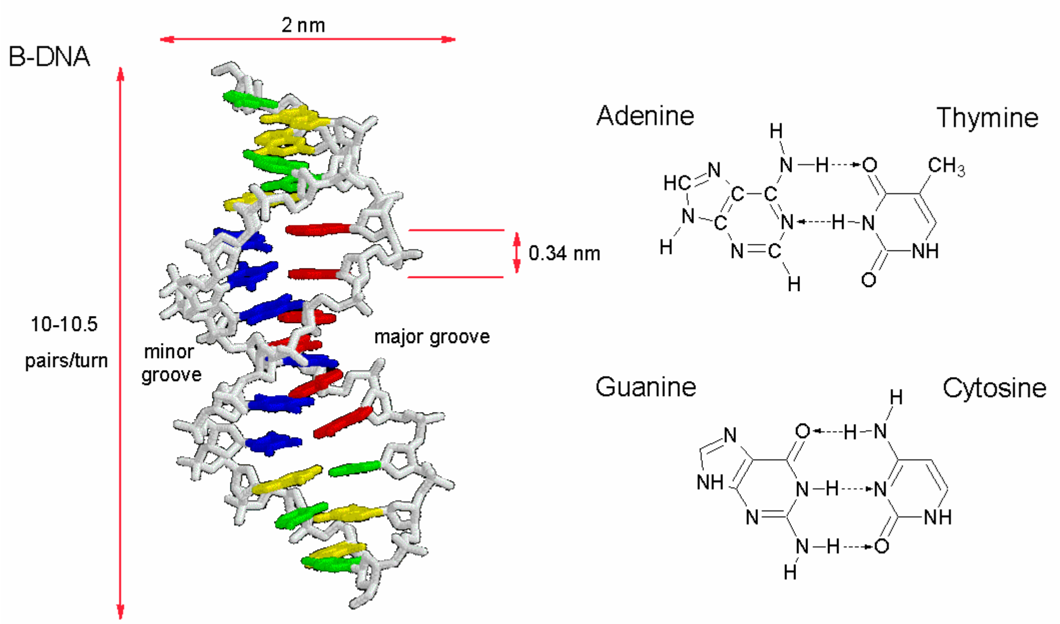

FIGURE 1.14*. B-DNA. The molecular structure and dimensions of key features of the molecule is shown on the left. The base pairs are shown on the right, where red arrows represent hydrogen bonded interactions.*

These properties include the affinity of complementary sequences, a well-stacked antiparallel double-helical backbone that is largely regular regardless of sequence and a persistence length (a measure of stiffness) around 50 nm under standard conditions. It is logical to examine whether these properties can be exploited outside of biology. Structural DNA nanotechnology aims to use the properties of DNA to produce highly structured and well-ordered materials from DNA. This effort has been underway since the early 1980s[179]. The structure of the DNA double helix is illustrated in ***FIGURE 1.14***. This classical DNA structure is known as B-DNA. On the left is the right-handed double-helical molecule; it consists of a pair of backbones whose units are alternating sugars and phosphates that are connected by hydrogen bonding between flat molecular units, called bases. The base–sugar–phosphate unit is called a ‘nucleotide’.

Note that the two backbones have a directionality, and that they are rotated upside down from each other; hence, there is a dyad axis of symmetry relating the backbones that is perpendicular to the helix axis. There is such a dyad going through every base pair and also half-way in between them. The phosphates are ionized at physiological pH, so the backbones are polyanions requiring neutralization by cations. The right side of ***FIGURE 1.14*** shows the Watson–Crick base pairs between adenine (A) and thymine (T), and between guanine (G) and cytosine (C). Although other forms of base pairing are possible, these pairs are most favoured within the double-helical context. The double-helical DNA molecule is inherently a nanoscale species: its diameter is about 2 nm, and its helical repeat is about 3.5 nm, consisting of 10–10.5 nucleotide pairs separated by 0.34 nm (***FIGURE 1.14***).

The early 1970s saw molecular biologists begin to exploit enzymes that modify the DNA molecule to produce new arrangements of DNA sequences. Using restriction enzymes that cleave at specific sites and ligases that fuse nicks in backbones, they were able to cut and splice DNA molecules, in much the same way that a film editor uses his tools to re-order sequences of film, creating a new overall effect[180]. The upshot of this activity was genetic engineering, which has led to the worldwide biotechnology industry. For our purposes, the key feature of their efforts was the use of single stranded overhangs (called ‘sticky ends’) to specify the order in which molecules were to be assembled. Sticky-ended cohesion between DNA molecules is illustrated in ***FIGURE 1.15(a)***. An important feature of sticky-ended cohesion is that when two sticky ends cohere, they form classical B-DNA[181], the structure established by Watson and Crick and refined by their successors. This principle is illustrated in ***FIGURE 1.15(b)***. Thus, if one knows the positions of the atoms of one component of a cohesive pair, one knows the positions of the other component. Hence, sticky ends provide the most readily programmable and predictable intermolecular interactions known, from the perspectives of both affinity and structure[182]. Of course, naturally occurring DNA is a linear molecule. From a topological standpoint, the DNA double helix is just a line. The line may be curved, and closed ones can be knotted or catenated; nevertheless, concatenating a bunch of lines together end-to-end just results in longer lines. Specific arrangements of DNA are of significant value to genetic engineers, because this establishes the presence and regulation of gene products, but linear DNA helical structures are not great structural components for

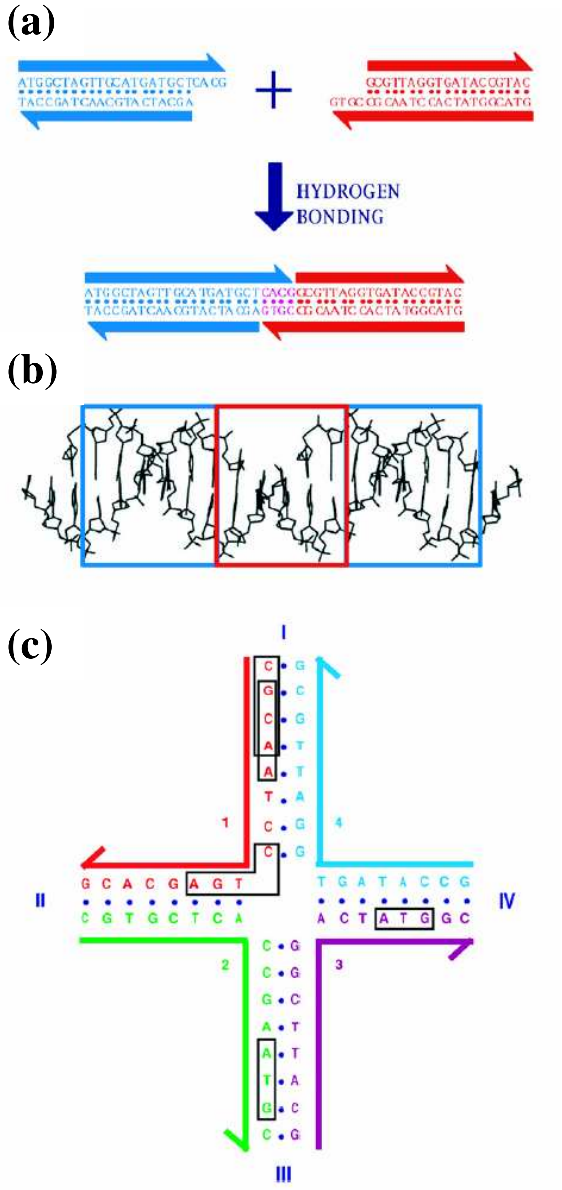

FIGURE 1.15*. (a) Sticky ends and (b) steric model highlighting the double helix formation. (c) Example of Holliday junction*

nanoscale structural engineering. The notion that rescues DNA from its linearity is to make synthetic branched molecules[179].

DNA is found to be branched at the level of secondary structure in biological systems; this means that conventional DNA strands associate to produce junction points. Thus, if we think of the strands of DNA as the lanes of a two-lane highway, a junction point would correspond to the lanes going through an intersection. Typically, branched DNA is an ephemeral intermediate in DNA metabolism; for example, the four-arm Holliday junction is an intermediate in genetic recombination[183]. Although branched DNA of biological origin usually displays symmetry that allows its branch point to migrate, it is a simple matter to design[179] and assemble synthetic DNA sequences that are stable because they lack this symmetry. An example of a stable asymmetric Holliday junction analogue lacking this symmetry is shown in ***FIGURE 1.15(c)***. The ability to generate stable branched DNA molecules opens new opportunities for the bottom-up construction of nanoscale objects.

1.6.1 The Goals of Structural DNA Nanotechnology

Ideally, the systems we have described above should be able to be used like molecular Lego: it should be possible to throw together a variety of branched-DNA components and exploit their well-defined combining properties to get them to self-assemble into a variety of shapes and arrangements. We will discuss below some of the limitations on this ideal system, but here is a good point for us to think about what we would like to be able to make, if this system behaved in an ideal fashion. The key-motivating goal in this system has been the desire to conquer the macromolecular crystallization experiment. Although quite a lore now exists, every macromolecule presents different crystallization problems. The problem of crystallizing a macromolecule of unknown structure is that one does not know how to promote the organization of the molecules into a periodic lattice in a rational fashion, because the structure is unknown. Furthermore, in contrast to experiments that are easily debugged, every relevant parameter must be within the correct window for the crystallization to be successful; consequently, the independent factors cannot easily be optimized individually, although incomplete factorial methods have been developed[184].

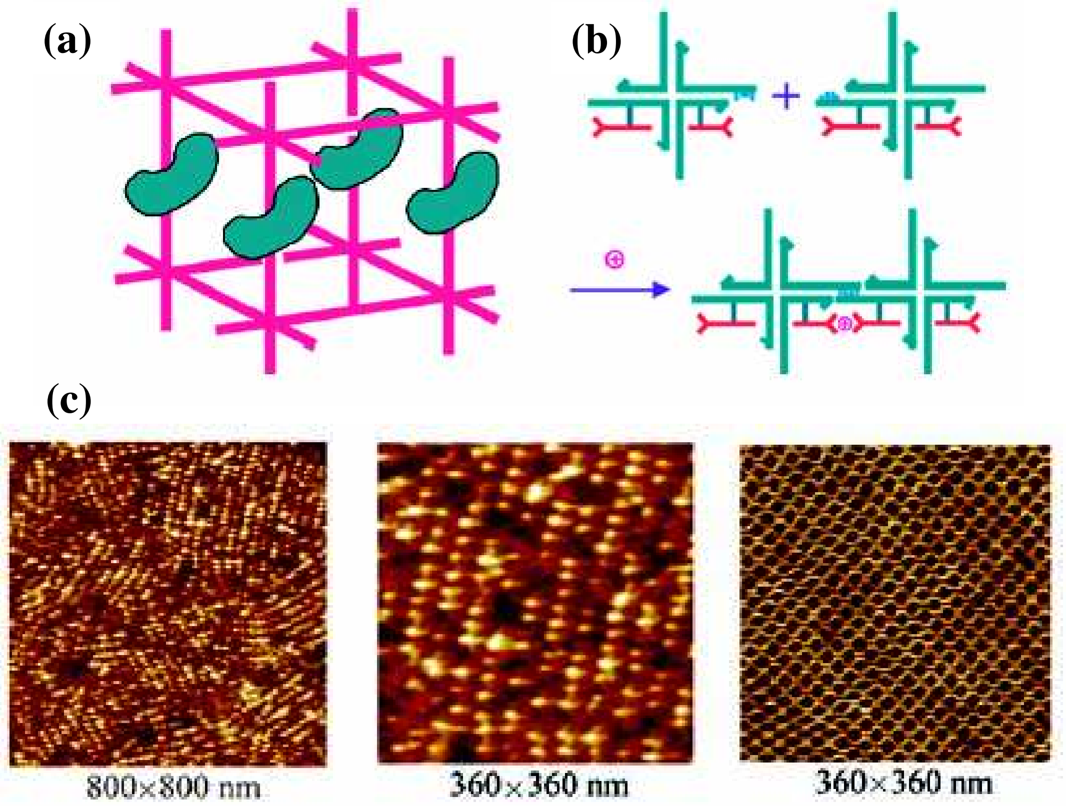

FIGURE 1.16. *Potential crystallization lattice (a) and nanoelectronic device (b). AFM images of gold nanoparticles functionalizing self-assembled DNA nanostructures (bottom right) are shown at low (bottom left) and high (bottom middle) magnification.*

DNA can be used to form periodic arrays that organize the macromolecule of interest[179]. The notion is illustrated in figure ***FIGURE 1.16(a)***. A ‘box’ of nucleic acid is designed to act as the repeating unit of a three-dimensional periodic lattice. A series of boxes are to be held together by sticky ends. These boxes act as the host lattice for a series of macromolecular guests that are positioned and oriented within the host lattice. If all are ordered adequately, then the x-ray diffraction experiment can be performed on the entire contents of the crystal. In addition to the ability perhaps to organize molecules that are otherwise intransigent to crystallization, this system offers the advantage that guest molecules that change their structures while binding to ligands would not destroy the lattice, because only DNA would be involved in maintaining lattice contacts.

If one can imagine organizing macromolecules, it is also possible to imagine organizing other species that do not readily self-organize. Prominent amongst them would be nanoelectronic components. The idea of using DNA to organize nanoelectronic components is not very new[185], but only recently has it started to gain favour. The concept, illustrated for a simple component in figure ***FIGURE 1.16(b)***, is that the outstanding architectural properties of DNA be used to act as scaffolding for species that are intractable to simple bottom-up organization with nanometre precision. In ***FIGURE 1.16(c)*** an example of this approach is given: DNA tile lattices have been functionalized with AuNP on specific sites on the single tile, resulting in an ordered array of AuNPs with a precision in the positioning of a few nanometers. This is just the first step in the development of a bottom-up strategy for the formation of more complex electronic devices.

1.7 References

1. Antonii, F. *Panacea Aurea-Auro Potabile*; Bibliopolio Frobeniano: Hamburg, 1618.
2. (a) Kunckels, J. *Nuetliche Observationes oder Anmerkungen von Auro und Argento Potabili*; Schutzens: Hamburg, 1676. (b) Savage, G. *Glass and Glassware*; Octopus Book: London, 1975.
3. Helcher, H. H. *Aurum Potabile oder Gold Tinstur*; J. Herbord Klossen: Breslau and Leipzig, 1718.
4. *Dictionnaire de Chymie*; Lacombe: Paris, 1769.
5. Fulhame, Mrs. *An Essay on Combustion with a View to a New Art of Dying and Painting*; J. Cooper: London, 1794.
6. Ostwald, W. Zur Geschichte des Colloiden Goldes. *Kolloid Z.* **1909**, *4*, 5.
7. Faraday, M. Experimental Relations of Gold (and other Metals) to Light. *Philos. Trans.* **1857**, *147*, 145-181.
8. Graham, T. *Philos. Trans. R. Soc.* **1861**, *151*, 183-190.
9. Kahn, R. L. Serum Diagnosis for Syphilis. In *Colloid Chemistry*; Alexander, J., Ed.; The Chemical Catalog Co.: New York, 1928; Vol. II, p 757.
10. Hauser, E. A. Aurum Potabile. *J. Chem. Educ.* **1952**, 456-458.
11. (a) Brown, D. H.; Smith, W. E. The Chemistry of the Gold Drugs Used in the Treatment of Rheumatoid Arthritis. *Chem. Soc. Rev.* **1980**, *9*, 217-240. (b) *Immuno-Gold Electron Microscopy in Virus Diagnosis and Research*; Hyatt, A. D., Eaton, B. T., Eds.; CRC Press: Boca Raton, FL, **1993**.
12. Turkevitch, J.; Stevenson, P. C.; Hillier, J. *Discuss.Faraday Soc.* **1951**, *11*, 55-75.
13. Frens, G. *Nature: Phys. Sci.* **1973**, *241*, 20-22.
14. Hayat, M. A. *Colloidal Gold, Principles, Methods and Applications*; Academic Press: New York, **1989**.
15. *Clusters and Colloids*; Schmid, G., Ed.; VCH: Weinheim, **1994**.
16. Bradley, J. S. In *Clusters and Colloids*; Schmid, G., Ed.; VCH: Weinheim, **1994**; Chapter 6, pp 459-544.
17. Schmid, G. *Chem. Rev.* **1992**, *92*, 1709-1727.

18. Fendler, J. H.; Meldrum, F. C. *Adv. Mater.* **1995**, *7*, 607-632.
19. Schmid, G.; Chi, L. F. *Adv. Mater.* **1998**, *10*, 515-527.
20. Edelstein, A. S.; Cammarata, R. C. *Nanoparticle: Synthesis, Properties and Applications*; Institute of Physics Publishing: Bristol, **1996**.
21. Schmid, G. In *Nanoscale Materials in Chemistry*; Klabunde, K. J., Ed.; Wiley: New York, 2001.
22. Bethell, D.; Brust, M.; Schiffrin, D. J.; Kiely, C. *J. Electroanal. Chem.* **1996**, *409*, 137-143.
23. Matijevic, E. *Curr. Opin. Colloid Interface Sci.* **1996**, *1*, 176-183.
24. *Optical Properties of Metal Clusters*; Freibig, U., Vollmer, M., Eds.; Springer-Verlag: New York, **1995**.
25. Ung, T.; Liz-Marza´n, L. M.; Mulvaney, P. *Colloids Surf. A: Physicochem. Eng. Asp.* **2002**, *202*, 119-126.
26. Yonezawa, T.; Toshima, N. In *Advanced Functional Molecules and Polymers*; Nalwa, H. S., Ed.; Gordon & Breach: Reading, UK, 2001; Vol. 2, Chapter 3, pp 65-86.
27. Brust, M.; Kiely, C. J. *Colloids Surf. A: Physicochem. Eng. Asp.* **2002**, *202*, 175-186.
28. Schmid, G.; Pfeil, R.; Boese, R.; Bandermann, F.; Meyer, S.; Calis, G. H. M.; van der Velden, J. W. A. *Chem. Ber.* **1981**, *114*, 3634-3642.
29. (a) Giersig, M.; Mulvaney, P. *Langmuir* **1993**, *9*, 3408-3413. (b) Hasan, M.; Bethell, D.; Brust, M. *J. Am. Chem. Soc.* **2003**, *125*, 1132-1133.
30. (a) Brust, M.; Walker, M.; Bethell, D.; Schiffrin, D. J.; Whyman, R. J. *J. Chem. Soc., Chem. Commun.* **1994**, 801-802. (b) Brust, M.; Fink, J.; Bethell, D.; Schiffrin, D. J.; Kiely, C. J. *J. Chem. Soc., Chem. Commun.* **1995**, 1655-1656.
31. (a) Chen, S. *Langmuir* **1999**, *15*, 7551-7557. (b) Chen, S.; Murray, R. W. *Langmuir* **1999**, *15*, 682-689.
32. (a) Hostetler, M. J.; Green, S. J.; Stokes, J. J.; Murray, R. W. *J. Am. Chem. Soc.* **1996**, *118*, 4212-4213. (b) Ingram, R. S.; Hostetler, M. J.; Murray, R. W. *J. Am. Chem. Soc.* **1997**, *119*, 9175-9178.

33. Templeton, A. C.; Wuelfing, W. P.; Murray, R. W. *Acc. Chem. Res.* **2000**, *33*, 27-36.
34. Hostetler, M. J.; Wingate, J. E.; Zhong, C.-J.; Harris, J. E.; Vachet, R. W.; Clark, M. R.; Londono, J. D.; Green, S. J.; Stokes, J. J.; Wignall, G. D.; Glish, G. L.; Porter, M. D.; Evans, N. D.; Murray, R. W. *Langmuir* **1998**, *14*, 17-30.
35. (a) Templeton, A. C.; Hostetler, M. J.; Kraft, C. T.; Murray, R. W. *J. Am. Chem. Soc.* **1998**, *120*, 1906-1911. (b) Hostetler, M. J.; Templeton, A. C.; Murray, R. W. *Langmuir* **1999**, *15*, 3782-3789.
36. Ebelmen, M. *Ann. Chim. Phys*. **1846,** *16*, 129.
37. Ebelmen, M. *Ann. Chim. Phys.* **1847,** *25*, 854.
38. Liesegang, R. E. *Photogr. Archiv.* **1896,** 221.
39. Heinisch, H. K. *Crystal Growth in Gels;* Pennsylvania State University Press: State College, PA, **1970**.
40. Ostwald, W. Z. *Phys. Chem.* **1897,** *27,* 365.
41. Rayleigh, L. *Philos. Mag.* **1919,** *38,* 738.
42. Lloyd, D. J. In *Colloid Chemistry;* Alexander, J., Ed.; Chemical Catalog Co.: New York, **1926**; p 767.
43. Holmes, H. N. In *Colloid Chemistry;* Alexander, J., Ed.; Chemical Catalog Co.: New York, **1926**; p 796.
44. Stern, K. H. *Bibliography of Liesegang Rings;* National Bureau of Standards Miscellaneous Publication No. 292, **1967**.
45. Roy, D. M.; Roy, R. *Am. Mineral.* **1954**, *39,* 957.
46. Roy, R. J. *Am. Ceram. Soc.* **1956**, *39*, 145.
47. Roy, R. J. *Am. Ceram. Soc.* **1969**, *52*, 344.
48. McCarthy, G. J.; Roy, R.; McKay, J. M. *J. Am. Ceram. Soc.* **1971**, *54*, 637.
49. Iler, R. K. *The Chemistry of Silica;* Wiley: New York, **1955**.
50. Stober, W.; Fink, A.; Bohn, E. *J . Colloid Interface Sci.* **1968**, *26*, 62.
51. Tan, C. G.; Bowen, B. D.; Epstein, N. *J. Colloid Interface Sci.* **1987**, *118,* 290.
52. Matijevic, E.; Bundnick, M.; Meites, L. *J. Colloid Interface Sci.* **1977**, 61, 302.
53. Matijevic, E. In Ultrastructure Processing of Ceramics Classes and Composites; Hench, L. L., Ulrich, D. R., Eds.; Wiley: New York, **1984**; p 334.

54. Matijevic, E. In *Science of Ceramic Chemical Processing*; Hench, L. L., Ulrich, D. R., Eds.; Wiley: New York, **1986**; p 463.
55. Matijevic, E. In *Ultrastructure Processing of Advanced Ceramics*; Mackenzie, J. D., Ulrich, D. R., Eds.; Wiley: New York, **1988**; p 429.
56. Kistler, S. S. *Nature* **1931**, *127*, 742.
57. Jones, S. M. In *Guinness Book of Records*, *"Lightest solid-state material"*, **2003**.
58. Dislich, H. *J. Non-Cryst. Solids* **1985,** *72*, 599.
59. Beck, J. S.; Vartuli, J. C.; Roth, W. J.; Leonowicz, M. E.; Kresge, C. T.; Schmitt, K. T.; Chu, C. T.-W.; Olson, K. H.; Sheppard, E. W.; McCullen, S. B.; Higgins, J. B.; Schlenker, J. L. *J. Am. Chem. Soc*. **1992**, *114*, 10834.
60. (a) Bradley, D. C.; Mehrotra, R. C.; Gaur, D. C. *Metal Alkoxides*; Academic Press: London, **1978**. (b) Mehrotra, R. C. *J. Non-Cryst. Solids* **1988**, *100*, 31.
61. www.iupac.org, *Definition and Classification of Colloids*.
62. Flory, P. J. *Principles of Polymer Chemistry*; Cornell University Press: Ithaca, NY, **1953**; Chapter IX.
63. (a) Sanchez, C.; Ribot, F. *New J. Chem.* **1994**, *18*, 1007. (b) Schubert, U.; Husing, N.; Lorenz, A. *Chem. Mater.* **1995**, *7*, 2010. (c) Mark. J. E. In *Diversity Into the Next Century*; Martinez, R. J., Arris, H., Emerson, J. A., Pike, G., Eds.; SAMPE Publications: Covina, CA, **1995**; Vol. 27. (d) Mark, J. E.; Wang, S.; Ahmad, Z. *Macromol. Symp*. **1995**, *98*, 731.
64. Ribot, F.; Toledano, P.; Sanchez, C. *Chem. Mater.* **1991**, *3*, 759.
65. Mehrota, R. C.; Bohra, R.; Gaur, D. P. *Metal, □-Diketonates and Allied Derivatives*; Academic: London, **1978**.
66. Guglielmi, M.; Carturan, G. *J. Non-Cryst. Solids* **1988**, *100*, 16.
67. Schmidt, H. *J. Non-Cryst. Solids* **1988**, *100*, 51.
68. Hench, L- L.; West, J. K. *Chem. Rev.* **1990**, *90*, 33.
69. Brinker, C. J.; Scherrer, G. W. *Sol-Gel Science, the Physics and Chemistry of Sol-Gel Processing*; Academic Press: San Diego, CA, **1990**.
70. Yoldas, B. E. *J. Mater. Sci.* **1986**, *21*, 1086.
71. Keefer, K. D. *Mater. Res. Soc. Symp. Proc.* **1984**, *32*, 15.

72. Schaefer, D. W.; Wilcoxon, J. P.; Keefer, K. D.; Bunker, B. C.; Pearson, R. K.; Thomas, I. M.; Miller, D. E. *AIP Conf. Proc.* **1987**, *154*, 63.
73. Mittal KL (ed) Polyimides: synthesis, characterization and applications. Plenum, New York, **1985**.
74. Lee H, Stoffey D, Neville K New linear polymers. McGraw-Hill, New York, **1967**.
75. Sroog CE Polyimides. In: Mark F, Gaylord NG, Bikales NM (eds) Encyclopedia of polymer science and technology, vol 11. Interscience New York, **1969**, p 247.
76. de Abajo J Polyimides. In: Kricheldorf HR (ed) Handbook of polymer synthesis, vol 2. Marcel Dekker, New York, **1992**, p 941.
77. Alvino M, Frost LW *J Polym Sci A-1* **1971,** *9*, 2209.
78. Kinloch AJ (ed) Structural adhesives. Elsevier, London, **1986**.
79. May CA (ed) Resins for aerospace. ACS Symp Series No 132. Am Chem Soc, Washington, **1980.**
80. Serafini T, Delvigs P, Lithsey GR *J Appl Polym Sci,* **1971,** *16*, 905.
81. Sat M Polyimides. In: Olabisi O (ed) Handbook of thermoplastics. Marcel Dekker, New York, **1997.**
82. Frazer AH High temperature resistant polymers. Interscience, New York, **1968.**
83. Cassidy PE Thermally stable polymers: synthesis and properties. Dekker, New York, **1980.**
84. Critchley JP, Knight GJ, Wright WW Heat-resistant polymers. Plenum, New York, **1983.**
85. Bessonov MT, Koton MM, Kudryavtsev VV, Laius LA, Polyimides: thermally stable polymers. Consultants Bureau, New York, **1987.**
86. Adrova N, Bessonov M, Laius LA, Rudakov AP Polyimides: a new class of heat resistant polymers. IPST Press, Jerusalem, **1969.**
87. Huang W, Tong YT, Xu J, Ding M *J Polym Sci, A Polym Chem,* **1997,** *35*, 143.
88. Bell VL, Stump BL, Gager H *J Polym Sci Polym Chem,* **1976**, *14*, 2275.
89. Lin Y-N, Joardar S, McGrath JE *Polym Prep* **1993**, *34(1)*, 515.

90. Malinge J, Garapon J, Sillion B *Brit Polym J,* **1988**, *20*, 431.

91. Lin T, Stickney KW, Rogers M, Riffle JS, McGrath JE, Yu TH, Davis RM *Polymer*, **1993**, *34*, 772.

92. Gerber MK, Pratt JR, St Clair TL Proceedings 3rd Int Symp on Polyimides, Ellenville, **1988**, p 101.

93. Connel JW, Croall CI, Hergenrother PW *Polym Prep*, **1992**, *33(1)*, 1101.

94. Kawashima Y, Ikeda T, Kitagawa H Proceedings 3rd Int Symp on Polyimides, Ellenville, **1988**, p 32.

95. Weinrotter K, Vodiunig R. In: Feger C, Khojasteh MM, McGrath JE (eds) Polyimides: materials, chemistry and characterization. Elsevier, Amsterdam, **1989**.

96. Takekoshi T *Adv Polym Sci*, **1990**, *94*, 1.

97. Abadie MJM, Sillion B Polyimides and other high-temperature polymers. Elsevier, Amsterdam, **1991**.

98. Moy TM, DePorter CD, McGrath JE *Polymer*, **1993**, *34*, 819.

99. Burks HD, St Clair TL *J Appl Polym Sci*, **1985**, *30*, 2401.

100. Eastmond GC, Prapotny J *Polymer*, **1994**, i, 5148.

101. Takahashi T, Yuasa S, Tsuji M, Sakurai K *J Macromol Sci Phys B*, **1994**, *33(1),* 63.

102. Huo PP, Friler JB, Cebe P, *Polymer*, **1993**, *34*, 4387.

103. Brode GL, Kwiatkowski GT, Kawakami *J, Polym Prepr*, **1974**, *15(1)*, 761.

104. Yang HH, Aromatic high-strength fibers. Interscience, New York, **1989**.

105. Scola DA, Pike RA, Vontell JH, Pinto JP, Brunette CM, *High Perform Polym*, **1989**, *1*, 17.

106. Cassidy PE, Aminabhavi TM, Farley JM, *J Macromol Sci Rev C*, **1989**, *29*, 365.

107. Young PR, Davis JRJ, Chang AH, Richardson JN, *J Polym Sci A Polym Chem*, **1990**, *28*, 3107.

108. Zoia G, Stern SA, St Clair AK, Pratt JA, *J Polym Sci B Polym Phys*, **1994**, *32*, 53.

109. Bell VL, Kilzer L, Hett EM, Stokes GM, *J Appl Polym Sci*, **1981***, 26*, 3805.

110. Havens SJ, Hergenrother PM, *J Polym Sci A Polym Chem*, **1990**, *28*, 2427.

111. Muellerleile JT, Risch BG, Rodriguez DE, Wilkes GL, *Polymer*, **1993**, 34, 789.

112. Asanuma TA, Oikawa H, Ookawa Y, Yamasita W, Matsuo M, Yamaguchi A, *J Polym Sci A Polym Chem*, **1994**, *32*, 2111.

113. Liou G-S, Maruyama M, Kakimoto M-A, Imai Y, *J Polym Sci A Polym Chem*, **1993**, 3*1*, 3273.

114. Kumar D, Gupta AD*,* *Polym Prep*, **1995**, *36(2)*, 49.

115. Yang C-P, Lin J-H, *J Polym Sci A Polym Chem*, **1995**, *31*, 2153.

116. Davies M, Hay JN, Woodfine B, *High Perform Polym*, **1993**, *5*, 37.

117. Pratt JR, Blackwell DA, St Clair TL, Allphin NL, *Polym Eng Sci*, **1989**, *29*, 63.

118. Eastmond GC, Paprotny J, Webster I, *Polymer*, **1993**, *34*, 2865.

119. Sek D, Pijet P, Wanic A, *Polymer*, **1992**, *33*, 190.

120. Rusanov AL, *Adv Polym Sci*, **1994**, *111*, 177.

121. Harris FW, Norris SO, *J Polym Sci Polym Chem Ed*, **1993**, *11*, 2143.

122. Harris FW, Hsu SL-C, *High Perform Polym*, **1989**, *1*, 3.

123. Giesa R, Keller U, Eiselt P, Schmidt H-W, *J Polym Sci A Polym Chem*, **1993**, *31*, 141.

124. Imai Y, Maldar NN, Kakimoto M-A, *J Polym Sci Polym Chem*, **1984**, *22*, 2189.

125. Akutsu F, Kataoka T, Shimizu H, Naruchi K, Miura M, *Macromol Chem Rapid Commun*, **1994**, *15*, 411.

126. Spiliopoulos IK, Mikroyannidis JA, *Macromolecules*, **1996**, *29*, 5313.

127. Korshak VV, Vinogradova SV, Vygodskii YS, *J Macromol Sci Rev Macromol Chem C*, **1974**, *11*, 45.

128. Korshak VV, Vinogradova SV, VygodskiiYS, Nagiev ZM, Urman YG, Alekseeva SG, Slonium IY, *Makromol Chem*, **1983**, *184*, 235.

129. Lozano AE, de la Campa JG, de Abajo J, Preston J, *J Polym Sci A Polym Chem*, **1993**, *31*, 138

130. Lozano AE, de la Campa JG, de Abajo J, Preston J, *Polymer*, **1994**, *35*, 873.

131. Kricheldorf HR, Schwarz G, *Makromol Chem Rapid Commun*, **1984**, *10*, 243.

132. Tsai T, Arnold FE, *Polym Prep*, **1986**, *27(2)*, 221.
133. Tanaka K, Kita H, Okano M, Okamoto K-I, *Polymer*, **1992**, *33*, 585.
134. Cassidy PE, Aminabhavi TM, Farley JM, *J Macromol Sci Macromol Rev,* **1989**, *C29*, 365.
135. Husk RS, Cassidy PE, Gebert KL, *Macromolecules*, **1988**, *21*, 1234.
136. Feger C, *Polym Prep*, **1991**, *32(2),* 76.
137. Chung T-S, Vora RH, Jaffe M, *J Polym Sci A Polym Chem*, **1991**, *29*, 1207.
138. Buchanan RA, Mundhenke RF, Lin HC, *Polym Prep*, **1991**, *32(2),* 193.
139. Misra AC, Tesoro G, Hougham G, Pendharkar S, *Polymer*, **1992**, *33*, 1078.
140. Matsuura T, Hasuda Y, Nishi S, Yamada N, *Macromolecules*, **1991**, *24*, 5001.
141. Schmidt, H. *J. Non-Cryst. Solids* **1985**, *73*, 681.
142. Schmidt, H; Philipp, G. *J. Non-Cryst. Solids* **1984**, *63*, 283.
143. Schmidt, H; Scholze, H; Kaiser, H. *J. Non-Cryst. Solids* **1984**, *63*, 1.
144. Schmidt, H. *Mater. Res. Soc. Symp. Proc.* **1984**, *32*, 327.
145. Wilkes, G. L.; Orler, B.; Huang, H. *Polym. Prepr.* **1985**, *26*, 300.
146. Wilkes, G. L.; Brenann, A. B.; Huang, H.; Rodrigues, D.; Wang, B. *Mater. Res. Soc. Symp. Proc.* **1990**, *171*, 15.
147. Wilkes, G. L.; Huang, H.; Glaser, R. H. *Silicon-Based Polymer Science: A Comprehensive Resource*; Advances in Chemistry Ser. 224; American Chemical Society: Washington, DC, **1990**; p 207.
148. Mark, J. E.; Pan, S. J. *Makromol. Chem. Rapid Commun.* **1982**, *3*, 681.
149. Mark, J. E.; Jiang, C.; Tang, M. *Macromolecules* **1984**, *17*, 2613.
150. Ning, Y. P.; Tang, M. Y.; Jiang, C. Y.; Mark, J. E.; Roth, W. C. *J. Appl. Polym. Sci.* **1984**, *29*, 3209.
151. Mark, J. E. In *Frontiers of Macromolecular Science*; Saegusa, T., Higashimura, H., Abe, A., Eds.; Blackwell Scientific Publishers: Oxford, **1989**.
152. Mark, J. E. *Chemtech* **1989**, *19*, 230.
153. Mark, J. E.; Wang, S.; Xu, P.; Wen, J. *Mater. Res. Soc. Symp. Proc.* **1992**, *274*, 77.

154. Schaefer, D. W.; Jian, L.; Sun, C.-C.; McCarthy, D.; Jiang, C.-Y.; Ning, Y.-P.; Mark, J. E.; Spooner, S. In *Ultrastructure Processing of Advanced Materials*; Uhlmann, D. R., Ulrich, D. R., Eds.; Wiley & Sons: New York, **1992**.
155. Mark, J. E.; Calvert, P. D. *J. Mater. Sci., Part C* **1994**, *1*, 159.
156. Wang, S. B.; Mark, J. E. *Polym. Bull.* **1987**, *17*, 231.
157. Mark, J. E.; Wang, S. B. *Polym. Bull.* **1988**, *20*, 443.
158. Wang, S. B.; Mark, J. E. *J. Macromol. Sci., Macromol. Rep.* **1991**, *A28*, 185.
159. Clarson, S. J.; Mark, J. E. *Polym. Commun.* **1989**, *30*, 275.
160. Landry, C. J. T.; Coltrain, B. K. *Polymer* **1992**, *33*, 1486.
161. Landry, C. J. T.; Coltrain, B. K.; Wesson, J. A.; Zumbulyadis, N. *Polymer* **1992**, *33*, 1496.
162. Sun, C.-C.; Mark, J. E. *J. Polym. Sci., Polym. Phys. Ed.* **1987**, *25*, 1561.
163. Shelly, D. B.; Giannelis, E. P. *Chem. Mater.* **1995**, *7*, 1597.
164. Krenceski, M. A.; Cantow, H. j.; Mulhaupt, R. *PMSE Prepr.* **1994**, *70*, 356.
165. Shao, P. L.; Mauritz, K. A.; Moore, R. B. *Chem. Mater.* **1995**, *7*, 192.
166. (a) Mauritz, K. A.; Stefanithis, I. D.; Davis, S. V.; Scheetz, R. W.; Pope, R. K.; Wilkes, G. L.; Huang, H. H. *J. Appl. Polym. Sci.* **1995**, *55*, 181. (c) Mauritz, K. A.; Warren, R. M. *Macromolecules* **1989**, *22*, 1730.
167. Mauritz, K. A.; Jones, C. K. *J. Appl. Polym. Sci.* **1990**, *40*, 1401.
168. Wen, J.; Mark, J. E. *Rubber Chem. Technol.* **1994**, *67*, 806.
169. Wen, J.; Mark, J. E. *J. Appl. Polym. Sci.* **1995**, *58*, 1135.
170. Pope, E. J. A.; Asami, M.; Mackenzie, J. D. *J. Mater. Res.* **1989**, *4*, 1017.
171. (a) David, I. A.; Scherer, G. W. *Polym. Prepr.* **1991**, *32*, 530. (b) David, I. A.; Scherer, G. W. *Chem. Mater.* **1995**, *7*, 1957.
172. Novak, B. M.; Ellsworth, N.; Wallow, T. I.; Davies, C. *Polym.Prepr.* **1990**, *31*, 698.
173. Novak, B. M.; Davies, C. *Macromolecules* **1991**, *24*, 5481.
174. Avnir, D.; Levy, D.; Reisfeld, R. *J. Phys. Chem.* **1984**, *88*, 5956.
175. Levy, D.; Einhorn, S; Avnir, D. *J. Non-Cryst. Solids* **1989**, *113*, 137.
176. Kobayashi, Y.; Kurokawa, Y.; Imai, Y.; Muto, S. *J. Non-Cryst. Solids* **1988**, *105*, 198.

177. Wen, J.; Wilkes, G. L. *Chem. Mater.* **1996,** *8,* 1667.

178. Sanchez, C.; Alonso, B.; Chapusot, F.; Ribot, F. *J. Sol-Gel Sci. Technol.* **1994**, *1*, 161.

179. Seeman N C, *J. Theor. Biol.* **1982***, 99***,** 237.

180. Cohen S N, Chang A C Y, Boyer H W and Helling R B, *Proc. Natl Acad. Sci. USA,* **1973**, *70* 3240.

181. Qiu H, Dewan J C and Seeman N C, *J. Mol. Biol.,* **1997**, *267***,** 881.

182. Seeman N C , *Chem.Biol.,* **2003**, *10***,** 1151.

183. Holliday R , *Genet. Res.,* **1964**, *5***,** 282.

184. Carter C W Jr, *Methods Enzymol.* A, **1997**, *276***,** 74.

185. Robinson B H and Seeman N C, *Prot. Eng.,* **1987**, *1***,** 295.

Chapter 2

Synthesis and Characterization of Fluorescent Gold Nanoclusters

2.1 Introduction

Noble metals exhibit a particularly wide range of material behavior along the atomic to bulk transition[1,2]. While high conductivity, ductility and malleability are generally accepted as the most peculiar physical characteristics of bulk noble metals and have historically been the reason for their extensive practical use, common knowledge usually associates them to their beautiful surface luster: despite this, the beauty of metals on the nano scale is far more than imagined[1-4]. Motivated by the complete understanding and manipulation of size-dependent properties, researchers have intensively investigated noble metals in different size domains for many decades[1]. Among these investigations, the study of few-atom metal clusters has attracted great interest because they bridge the evolution of properties from isolated atoms to nanoparticles and even to the bulk[5-10]. According to the number of metal atoms, nanoscale metals are roughly classified into three size domains: large nanoparticles, small nanoparticles and clusters, corresponding to three different characteristic length scales respectively[1,11].

The first characteristic length scale encountered in shrinking from bulk to nanoparticles is the wavelength of light. Optical responses of large metal nanoparticles ($R \sim \lambda$) to external electromagnetic fields are simply dependent on their sizes, free electron density and therefore their dielectric function relative to that of the surrounding medium. This size-dependent effect is extrinsic because optical properties such as dielectric functions (i.e. refractive indexes) of the nanoparticles are similar to those of bulk metals[1]. These optical properties can be quantitatively described with the theory Mie proposed in 1908 for small metallic spheres[1]. Applying Maxwell's equations with appropriate boundary conditions in spherical coordinates, Mie found that optical absorption, light scattering and extinction of a metal sphere depend on its radius and bulk dielectric functions[1,2].

When particle size approaches the second characteristic length, electron mean free path (the average distance an electron travels between two adjacent collisions, and ~50 nm for gold and silver) [11], the dielectric function and refractive indices become size dependent. As a result, the optical responses such as plasmon absorptions of small metal nanoparticles ($R<<\lambda$) have different size-dependences compared with large nanoparticles. This is an intrinsic or quantum size effect[1,11], but Mie theory still can be extended into this quasi-static regime.

Eventually, when particle size becomes comparable to the third characteristic length - Fermi wavelength of an electron (i.e. de Broglie's wavelength of an electron at the Fermi energy, or ~0.5 nm for gold and silver) [2,12,13], optical, electronic and chemical properties of metal clusters are dramatically different from the other two size regimes. In this smallest size regime, metal clusters become "molecular species" [14-16], and discrete states with strong florescence can be observed[6,9,10,19-22]. Providing the "missing link" between atomic and nanoparticle behavior in noble metals, these highly fluorescent noble metal nanoclusters smoothly link the optical and electronic structure transitions from atoms to nanoparticles with observable free electron behavior and also offer new opportunities for creating new biological labels, energy transfer pairs, and other light emitting sources in nanoscale electronics.

2.2 Free electron model

In 1900, Drude successfully applied the kinetic theory of gases to explain the electrical and thermal conduction of metals with three assumptions to account for electron densities and interactions of metals being much greater than those of classical gases[1,11]. These assumptions are: (1) The interactions of a given electron with others and with ions are neglected between two collisions. (2) Electron-electron scattering is neglected. (3) Electrons experience a collision probability per unit time of $1/\tau$, where τ is the interval between two adjacent collisions. In the Drude model, the valence electrons of metals were considered free electrons due to strong electron screening effects. These free electrons are delocalized in the bulk metals and do not belong to any specific metal atoms. As a result, free electrons move in the constant potential field provided by the positively charged cores. The total Hamiltonian of a metal can be written as the sum of "non-interacting" Hamiltonians of free electrons, which is also called the "one particle" approximation.

Although the free electron model was originally proposed based on the kinetic theory of molecular gases, the dramatic difference between these two systems is that the energy levels are not quantized in a molecular gas while they are quantized in metals due to the Pauli exclusion principle[11,23]. As a result, the energy of an electron system is enormously larger than that of a molecular gas system. Based on the one-particle approximation, the effective Hamiltonian for an electron can be considered as a free electron moving in a constant potential field. Consequently, a simple particle in a box model is used to describe the behaviors of the free electrons in metals. The energy levels of metals can be simply written as

$$E = \frac{n^2 h^2}{2mL^2}$$

based on the one particle in a box model, where n is the principle quantum number, E is the energy of a quantized level, L is the size of the box, m is electron mass, h is Planck's constant.

The boundary conditions for this box are the physical dimensions of the system. However, since metals have periodic crystal structures in the bulk states, boundary conditions can be set at any length as long as properties of metals are size-independent. This simple model sheds light on how the free electrons pile up in the metals. In a given metal, since each energy state could have different degeneracy, the number of the free electrons will be piled up at the rate of as many electrons per level as permitted by its degeneracy until all the electrons are exhausted[11,23]. For example, while only 2 electrons are allowed in the lowest energy state, 6 electrons are allowed in the second lowest energy level because of degeneracy increasing. The topmost filled level corresponds to the highest electron energy of a given metal, called the Fermi energy E_f, which is independent of the metal size. Quantized energy states and large Fermi energies are characteristic of an electron gas, thereby making them distinct from the more familiar molecular gas.

2.2.1 Metallic Optical Responses at Different Size Scales

The optical response of free-electron metals in the bulk state is well described by Drude-Lorentz-Sommerfeld/free electron model[1,11]. Based on this model, the macroscopic optical response of metals follows by summing the single electron response over the total number of the free electrons. Thus, according to this model, all the free electrons in a metal react in phase with the electrical field[1,11]. In reality, due to the large electron density and delocalization, all the free electrons indeed coherently oscillate under a time dependent electrical field, which gives the well known bulk plasmon absorption. The frequency of bulk plasmon can be written as[1,11]

$$\omega_p = \left(\frac{4\pi n e^2}{\varepsilon_0 m_e} \right)^{1/2}$$

where ε_0 is the dielectric constant of vacuum, m_e is the effective electron mass, and n is the electron density of the bulk metal. The dielectric “constant” of a metal is a function of the frequency of the external electrical field. Its real and imaginary parts, respectively, can be written as[1,11]

$$\varepsilon_R \approx 1 - \frac{\omega_p^2}{\omega^2} \qquad \varepsilon_i \approx 1 - \frac{\omega_p^2}{\omega^3}\Gamma$$

in which ω_p is the Drude plasma frequency and the relaxation time constant Γ ($\Gamma = 1/\tau$, τ is relaxation time) is related to the electron mean free path l by $\Gamma = v_f /l$, where v_f is the average speed of an electron at the Fermi energy. When ω is larger than ω_p, the metal becomes transparent and radiation can propagate without absorption.

When metal nanoparticle size is comparable to the light wavelength, plasmon absorption becomes size-dependent although the metallic dielectric functions remain nearly equal to those of the bulk. The free electrons in the large nanoparticles have different oscillation modes toward the time-dependent electrical field of the light.

The optical response of the metal nanoparticles is the summation of all the different plasmon frequencies resulting from dipole and higher order oscillation modes[1],

$$\omega_L \approx \frac{\omega_p}{\sqrt{1 + \frac{L+1}{L}\varepsilon_m}}$$

in which ω_p is the volume plasmon frequency of a bulk metal, L is the oscillation mode and is equal to one for dipole oscillation, and two for quadrapole oscillation, ε_m is the dielectric constant of an embedding material. When the diameters of metal nanoparticles are larger than their mean free paths, not only dipole oscillation but also the higher-order multipole oscillations are allowed. The plasmon positions of metal nanoparticles can be calculated with Mie theory.

Assuming that ε_m is 1 in vacuum, for a spherical metal nanoparticle, its surface plasmon frequency is $\omega_p / 3^{1/2}$ because L is equal to 1.

Qualitatively, the larger the metal nanoparticle is, the lower its surface plasmon absorption frequency. Conduction electrons in a spherical nanoparticle act like an oscillator system, whereas in bulk metals they behave like a relaxator system to dissipate energy. The displacement of negative charges due to an electric field gives rise to polarization charges at the nanoparticle surface and hence to a linear restoring force between electrons and positive charges[1].

When metal nanoparticle sizes become much smaller than the electron mean free path, a monotonic absorption transition with size is observed because absorption is mainly due to dipole oscillation mode while higher order oscillations contribute much less to the overall oscillation strength[24]. Both the absorption frequency and the absorption linewidth have simple size-dependences. For silver nanoparticles (with diameter 2 nm < D <10 nm) embedded in an argon matrix, absorption linewidths Γ and frequency $h\omega_s$ are quantitatively related to silver particle diameter D. With decreasing silver particle size, the bandwidth increases and the plasmon position is blue shifted, as described by the empirical relations:

$$\Gamma / eV \approx 0.04 + \frac{0.59}{D / nm} \qquad h\omega_s / eV = 3.21 + \frac{0.58}{D / nm}$$

2.2.2 Electronic Structure of Noble Metals

Although optical responses of metals and metal nanoparticles are strongly size-dependent, metallic band structure is only weakly size-dependent. Bulk metals have continuous band structures and the conduction bands are occupied with free electrons. Such band structure is also observed from metal nanoparticles larger than 2 nm, in which the density of states is large enough and energy level spacings between adjacent quantum states are much smaller than thermal energy[24]. Thus, these delocalized free electrons coherently oscillate and give the well-known surface plasmon absorption. Differences in size-dependent optical response mainly arise from the change in the number of free electrons.

When metal nanoparticle size approaches the Fermi wavelength, the continuous band structures of metals break up into discrete energy levels. In 1964, Kubo produced quantitative predications on the electronic structure of very small metal clusters based on the recognition that quasi-continuous electron energy states of bulk metals become discrete on the few-atom scale[25]. The energy level spacing between adjacent levels for an N-atom particle is on the order of E_f/N, where E_f is theFermi energy of the bulk metal. The relative difference between the energy level spacing and thermal energy has become a criterion to distinguish metallic conduction from insulation[26]. If the energy level spacings are smaller than thermal energy, thermal energy can create mobile electron-hole pairs in the metals. As a result, current can flow through the metal. However, if the energy level spacings are much larger than the available thermal energy, the free electrons in the metal clusters are confined to discrete energy levels. Thus, the metal clusters are often considered to be nonmetallic. Although Kubo et al. predicted some properties of metal cluster electronic structure; the quantitative correlation of electronic structures with the number of atoms in metal clusters was not discovered until 1984[27].

2.2.3 Optical Response of Alkali Metal Clusters

Knight and co-workers observed a periodic pattern of intense peaks in the mass spectra of alkali metal clusters Na_n, indicating that Na clusters with $n = 2, 8, 18, 20, 40, 58$ have greater stability than do others[27]. This magic pattern in stability can be rationalized with a simple quantum mechanical model called the jellium model, which originates from nuclear physics[24,27-29]. Due to a strong electron screening effect, valence electrons of noble metal atoms are considered free electrons after neglecting electron-electron and electron-ion interactions. In this model, a metal cluster is modeled by uniform, positively charged spheres with electronic shells filled with free electrons. These free electrons are provided by the valence electrons of alkali atoms, and they delocalize and form spherical electron shells surrounding thepositively charged core. Distinct from electronic structure of single atoms, cluster electron density is independent of the number of free electrons in the metal clusters. However, analogous to single atoms, free electrons in metal clusters are also delocalized for electronic shells surrounding the atoms and subject to the Pauli Exclusion Principle. The quantized shells can be described by a simple 3D harmonic oscillator[24,27-29]. Due to the nature of the cluster spherical potential, the solutions of the Schrödinger equation are very similar to those of single atoms. Similarly, these free electrons form quantal shells surrounding the positively charged cores. Although jellium orbitals are labeled in the similar way as are with atomic orbitals, the principle quantum number n of Jellium orbitals is different to that n_{atom} of atomic orbitials and has such relation, $n = n_{atom}-l$, where l is the angular momentum quantum number[24]. In addition, it should be noted that angular momentum is not restricted by the principal quantum number n. As a result, 1s, 1p, 1d, 2s, 1f, 2p, … are observed in the electronic structure of alkali clusters because of potential surface differences between clusters and atoms. For example, an electron in hydrogen atom is in a r^{-1} potential, while an electron in a metal cluster is in the spherical harmonic oscillator (HO) r^2 potential.

As a result, for a given shell n, the magic numbers for the r^{-1} potential are following the equation

$$N_0 = \frac{2}{3} n \left(n + \frac{1}{2} \right) (n+1)$$

and are 4, 10, 18…, corresponding to 1s, 2s, 2p, 3s, 3p, 3d…. electronic shells, while the magic numbers for the harmonic oscillator are following the equation

$$N_0 = \frac{1}{3} (n+1)(n+2)(n+3)$$

and are 2, 8, 18, 20…, corresponding to 1s, 1p, 1d, 2s,…. electronic shells.

The determination of the harmonic oscillator energy level spacing $\hbar\omega$ for atomic clusters and its variation with the particle number N is discussed in literature [1–3], by adopting the approach which is traditionally followed in *nuclear physics* [4] and adjusting it to the case of atomic clusters. The essential idea is that the energy scale is directly related to the size of the cluster. It is assumed that the cluster valence electrons have a constant density ρ_0 equal to the bulk conduction electron density and the size R_0 of the (spherical) cluster is normalized so that it contains exactly N electrons, that is $R_0 = r_s N^{1/3}$, where $r_s = (3/4\pi\rho_0)^{1/3}$ is the Seitz–Wigner radius (in atomic units). By equating the mean-square radius of such a density distribution to that which results on the basis of the HO model in the case of large N, there results the following expression for $\hbar\omega$ (in eV):

$$\eta\omega_0 = 3.61 \frac{\eta^2}{2m_e r_s^2} N^{-\frac{1}{3}}$$

Fundamentally, the jellium model is the Drude free electron model and contains the same assumptions. The magic sizes observed in the alkali clusters are due to the complete filling of the different energy shells. For example, in Na_8 cluster, each Na atom donates one valence electron, and these free electrons are delocalized to form electronic shells surrounding the positively charged core composed of Na atoms. Eight free electrons completely fill the 1s and 1p energy states forming a complete valence shell, thereby making Na_8 very stable. The next stable size is Na_{18}, resulting from filled 1d energy state. Due to the similarity in electronic structure between metal clusters and single atoms, these metal clusters can also be called “multielectron” artificial atoms[24,27-29]. Since the number of the free electrons are piled up in the metal clusters with constant electron density, Fermi energies of “free electron” metals only depend on the electron density ρ_0 or the Wigner-Seitz radius (r_s) of the metals as shown in the equation

$$E_f = \frac{p_f^2}{2m_e} = \frac{\left(3\pi^2 \rho_0\right)^{\frac{2}{3}}}{2m_e} = \left(\frac{9\pi}{4}\right)^{\frac{2}{3}} \frac{\hbar^2}{2m_e r_s^2}$$

By combining equations 9 and 10, a very simple relation of frequency and Fermi energy can be derived[24,27-29]

$$\hbar\omega_0 \cong E_f N^{-\frac{1}{3}} = \frac{E_f r_s}{R}$$

This simple equation gives a quantitative explanation of how the electronic structures of alkali clusters changes with the number of free electrons. Energies of ground states as well as those of different excited states can be predicated with this equation.

Electronic shell structure was observed not only in the alkali metal clusters, but also in other metals. For example, Rademann and coworkers found that the ionization energies of Hg_n clusters increase with decreasing size, and roughly follow *1/R* law[30], simillarly to what has been discovered for the ionization potential of lithium and potassium clusters ($n < 100$)[31,32]. Many gas phase optical studies of alkali metal clusters have yielded the further important insights into alkali metal nanocluster structure. For example, in the optical spectra of Na^{+}_{n} clusters at 105 K, for small cluster size ($n = 3 \div 9$), single and well separated electronic transitions were clearly observed[33]. When the cluster size increases ($n = 10 \div 15$), the number of electronic transition lines increase and electronic transitions start to overlap. An additional and broad absorption started to show on the high energy side of the absorption spectra in the larger Na clusters. This high energy absorption is the volume plasmon absorption of Na clusters rather than the often invoked interband transition (see below). This important set of studies clearly indicated strong size-dependent transitions from single electron resonance to collective plasmon oscillation in few atom Na clusters.

2.2.4 Absorption and Emission of Gold Clusters

Discrete emissions and absorptions from gold dimers and trimers embedded in argon matrices have been thoroughly investigated at low temperatures, as well as the gas phase optical absorption spectra of gold clusters Au_n ($n = 7, 9, 11, 13$) with photodepletion spectroscopy. Sharp lines between 1.9 and 5.6 eV in absorption bands were observed. In addition, a pronounced odd-even alternation in the mass spectra of gold clusters indicated that Au cluster stability may follow a simple electron pairing scheme, which is in contrast to the jellium model[34-48].

Gold clusters are also highly stable at ambient conditions. Schmid and coworkers created Au_{11}, Au_{13}, Au_{55} in solution phase with the assistance of organic ligands[39-44]. Electronic transitions between 1.6 eV and 4.0 eV were observed from their absorptions. Au_{55} is especially interesting because of its remarkable chemical stability. The extraordinary stability of Au_{55} is due to its almost perfect close packing cuboctahedral structure[39]. High stability of other gold clusters such as Au_{13} and Au_{147} are also related to their closed atomic shells. This “chemical selection” in the solution phase avoids having an arbitrary number of atoms in a particle, which is also a very important factor in determining the magic sizes of gold clusters under ambient conditions[39,45]. The optical spectra of Au_{55} appear to be rather structureless, neither showing a collective excitation resonance nor exhibiting distinct absorption bands known from few-atom clusters, possibly bridging transition from discrete energy levels to collective oscillations[29,43,44,46,47].

Fluorescence was also observed from Au clusters in the solution phase. In 1998, Wilcoxon et al observed blue emission at 440 nm from small gold nanoparticles ($D < 2.5$ nm) [48], however, due to the heterogeneity of the solution, the exact size of emissive species was not able to be identified. The Whetten and El-Sayed groups observed near IR emission from glutathione encapsulated Au_{28} clusters in aqueous solution[9]. Compared to well-studied alkali clusters[27,31], the size-dependent electronic structure of these noble metals remains poorly understood.

As discussed above, optical properties such as the plasmon absorption of noble metal nanoparticles can be well explained with the free electron model on different length scales. A fundamental question is whether this model which nicely explains the properties of large noble metal nanoparticles and small alkali clusters can be used in interpretation of optical properties of few atom noble metal clusters. Although the electronic structure of noble metal clusters remains unclear at ambient conditions, free electron behavior has recently observed from gold nanowires at low temperature[49]. Ho and coworkers recently studied the energy levels of few atom gold nanowires on a NiAl substrate at cryogenic temperatures with scanning tunneling microscopy. Results indicated that the electronic properties such as conductance of one-dimension gold cluster chains were determined by the number of free electrons in the chains. Each gold atom in the chains only donate its 6s electron, and these valence electrons are delocalized in the whole chain because strong electron screening effect due to core electrons and d electrons. On the Fermi wavelength scale, 5d electrons of gold clusters are more tightly bound by the nucleus than are 6s electrons. As a result, there is also a large energy gap between the s band and the d band, and d electrons have little perturbation on the conduction band structure of few-atom gold clusters.

Currently two possible mechanisms could be used to explain the observed emission from these small metal clusters. One is due to intraband (sp/conduction band) transition. The other is interband (d-sp) transition. In this thesis, fluorescence is utilized as a signature of electronic structure to explore the fundamental physics of these few-atom noble metal clusters and their lowest lying electronic levels.

2.3 Experimental

2.3.1 Synthesis of Octadecanethiol-Capped Fluorescent Gold Clusters

HAuCl4·5H2O (5 μmol) (Aldrich) and octadecanethiol (5 μmol) (Aldrich) were co-dissolved in 20mL chloroform (90%) and ethanol (10%) solution. The solution was subsequently reduced with one equivalent of 0.05 M $NaBH_4$ aqueous solution. After being stirred for two days, the solutions produce strong blue emission with a maximum emission wavelength at 455 nm. The emission colors of the solutions were observed from near UV to the red region by changing the octadecanethiol to gold molar ratio from 0.5 to 3.

The suspensions were then centrifuged at 4000 rpm to remove larger clusters that occasionally formed. The solvent can be easily removed by carefully reducing the pressure, yielding a waxy paste that retains the solution luminescent properties. Such paste can then be redissolved in organic aprotic solvents (toluene, chloroform, etc).

2.3.2 Preparation of Polymer-Cluster Nanocomposites

The preparation of polymer-cluster nanocomposites can be achieved by simply mixing a solution of an organic polymer and a solution of the luminescent gold nanoclusters, possibly using the same solvent. When this is not possible, some care must be taken in the choice of the solvents if films of good quality and thickness larger than a micron have to be obtained. In particular, the solvent with the larger vapor pressure should also have the larger surface tension[50].

2.3.3 Preparation of Hybrid Matrix-Cluster Nanocomposites

Octadecanethiol-capped clusters can be easily dispersed as well in hybrid matrices. Copolymers of methyl-methacrylate and trimethoxysilyl-methyl-methacrylate were synthesized via radical polymerization in toluene or tetrahydrofuran. The details of the synthesis are reported in the **APPENDIX**. The gold-cluster solution was added and the resulting mixture sonicated for 10 min, before casting in custom-made teflon scaffolds or spin-coating.

2.3.4 Preparation of Silica-Cluster Nanocomposites after Cluster Ligand Exchange

When the nanoclusters were to be introduced in inorganic sol-gel matrices, the alkylthiol ligand had to be exchanged with a thiol carrying a silane funcionalities, so as to compatibilize the guest metal particle with the oxide host. In particular, 3-mercaptopropyl-trimethoxysilane (MPS) was chosen for its wide availability. The ligand exchange reaction was performed as follows: the nanocluster paste was resuspended in dichloromethane and a 10-fold excess of MPS was added. After 2 days at room temperature, the solvent was evaporated to dryness and the particles were washed multiple times with acetone or tetrahydrofuran, resuspended in methanol or ethanol and added to the sol-gel precursor solution.

For silica-gold nanocomposites, the silica matrix was prepared by adding dilute HCl to a tetraethoxysilane (TEOS) solution in ethanol, so that the molar ratios between the reactants are EtOH:TEOS = 2:1, H_2O:TEOS = 2:1, HCl/TEOS = 1:100. After 30 min stirring at room temperature in a closed vial, the solution is diluted twice with ethanol so that spin-coating at 3000 rpm yields crack-free films with a thickness of 100 nm.

2.3.5 Analytical Techniques

Fluorescence measurements were performed with a Jasco FP 6300 Fluorescence Spectrometer with quartz cuvettes and spectroscopy grade solvents. Thin filmand bulk samples were mounted on a custom made sample holder

Transmission electron microscopy (TEM) was carried out at CNR-IMM Institute in Bologna with a field emission gun FEI TECNAI F20 (S)TEM microscope operating at 200 kV.

Lifetime measurements were acquired with a HORIBA Jobin Yvon Fluoromax system at CIVEN in Venezia.

2.4 Results and Discussion

2.4.1 Fluorescence in Solution

Emission and excitation spectra of samples emitting at varying wavelengths are reported in ***FIGURE 2.1***. By varying the gold:thiol ratio, it's been possible to tune the emission wavelength from the near-UV to the red, and possibly to the near IR. Both emission and excitation spectra suggest the presence of overlapping absorbing and emitting species, in particular in the neighboring wavelength range.

Near-UV emission is centered at 385 nm, with a shoulder at 400 nm; the corresponding excitation spectrum shows a maximum at 325 nm, and a second peak at 345 nm. Blue emission is centered at 440 nm, with shoulders at 385 nm and 530 nm; the corresponding excitation spectrum shows a maximum at 355 nm, and shoulders at 325 nm and 400 nm. Green emission is centered at 530 nm, with a shoulder at 580 nm; the corresponding excitation spectrum shows a maximum at 410 nm, and a second peak at 375 nm. Red emission is centered at 625 nm; the corresponding excitation spectrum shows a maximum at 315 nm.

From the comparison of the fluorescence data, it's clear that most of the considered samples do not represent spectrally pure species, but rather each of them is composed by two or three distinct emitting moieties. It's interesting to notice that the multiple emission wavelengths are neighboring. In fact, the chosen synthetic strategy is meant to yield small, monodisperse clusters through a fast nucleation-slow growth process, where the limiting factor is the slow reductant addition; any shift from the ideal experimental conditions is expected to result in a broadening of the size distribution. These considerations provide a first hint at the proposed correlation between cluster size and emission wavelength: polydispersity implies the presence of species emitting at different wavelengths.

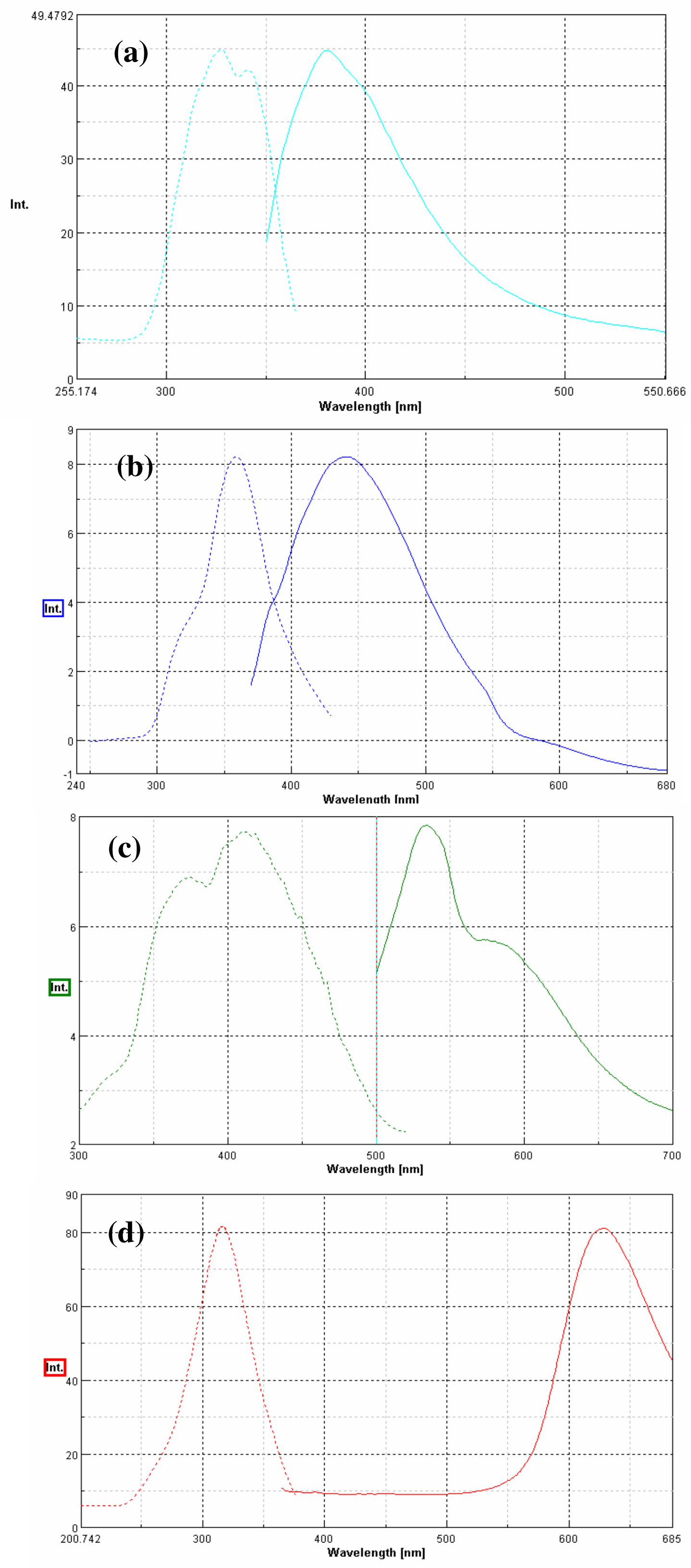

FIGURE 2.1. *Emission and excitation spectra of fluorescent gold particles emitting in the UV (**a**, λ_{em} = 385 nm, λ_{exc} = 325), blue (**b**, λ_{em} = 440 nm, λ_{exc} = 355), green (**c**, λ_{em} = 530 nm, λ_{exc} = 410) and red (**d**, λ_{em} = 625 nm, λ_{exc} = 315).*

Red emission on the other hand is relatively narrow: a possible interpretation lies in the fact that thiols act not only as ligands, but also as reducing agents. When a stoichometric amount of thiols is added to a gold(III) solution, i.e. when the thiol to gold ratio is equal or greater than 3, the solution quickly loses the strong yellow discoloration associated to the trivalent gold complexes and turns colorless, with the reaction proceeding as follows:

$$\mathrm{Au(III)} + 3\ \mathrm{HSR} \rightarrow \mathrm{AuSR} + \mathrm{RSSR}\ ,$$

where the charge-balancing protons and chlorides have been omitted for clarity. The exact nature of the metastable product AuSR species produced is not clear; but this process is described as resulting in Au(I)-chlorothioethers, i.e. non-metallic 'polymers' $(\mathrm{AuSR})_n$, bound by bridging SR groups, that are used as the active precursor in gold paints and in anti-arthritis drugs, depending on the identity of R. These moieties are extremely elusive and difficult to characterize, and in sub-stoichometric syntheses especially it’s difficult to evaluate their contribution to the formation of the final products.

The growth stage is simply an eliminative condensation process starting from unstable AuSR (stoichiometric) molecules, in the presence of excess RSSR:

$$\mathrm{NAuSR} \rightarrow \mathrm{Au_N(SR)_M}\ , \text{ with } \mathrm{N} >> \mathrm{M} \qquad (1)$$

This process can be stimulated at room temperature by the action of a gradually added reducing agent, e.g. dispersed $\mathrm{BH_4^-}$, expressed in simplified form as:

$$\mathrm{BH_4^-} + \mathrm{AuSR} \rightarrow \mathrm{HSR} + \mathrm{Au^{(0)}} + \mathrm{BH_3} \qquad (2)$$

A great excess of this agent is added to assure that growth (1) is driven to its natural completion. Alternatively, elevated temperatures or ultraviolet radiation could be used. The liberated gold atoms combine to form growing clusters, but their accretion rate is limited by the controlled release of Au atoms (2), and coalescence of cluster pairs is eliminated by the presence of excess RSSR groups bound weakly to the cluster surfaces.

In our synthetic approach, the usual inverse relation between particle size and thiol:gold ratio (less thiols determine large particles) is reversed: as only one equivalent of the reducing agent is slowly added, Au(I)SR species are reduced faster than Au(III) chlorates, with the resulting cluster size proportional to the availability of the metastable thiolated precursors. Fluorescent clusters are formed while gold(III) is still present in solution; however, the presence in solution of ethanol, a weaker reducing agent, leads after several days to the formation of easily removable large precipitates.

In principle, small gold(I) complexes are also found to give bright luminescence[5-14]. In these luminescent gold(I) clusters, gold ions provide available states and hybridize with organic ligands by forming charge transfer bands[5-14]. Luminescence is roughly attributed to metal to metal electronic transitions, coupled with strong ligand to metal charge transfer transitions. The emission center is usually assigned to metal-metal electronic transitions and emission energy is inversely proportional to gold-gold distance at low temperature[14,15]: therefore, since lowering the temperature can result in the decrease of Au(I)-Au(I) bond length, it can result in a blue shift of the emission energy[16].

Studies on luminescent polynuclear gold(I) complexes and clusters suggest that if surface atoms in gold nanoparticles are in high oxidation states, they might exhibit luminescence by forming ligand-metal charge-transfer band and metal(I)-metal(I) interactions. It’s therefore important to rule out this potential source of luminescence in the proposed small gold clusters: in fact, the addition of very large excesses (100 equivalents) of reducing agents after the cluster formation doesn’t alter at all the emission intensity and wavelength. Another significative difference arises from the comparison of emission lifetimes: while Large Stokes-shifted luminescences with μs lifetimes are generally characteristics of the gold(I) complexes, the lifetimes we measured for the small gold clusters are in the ns regime, as shown in ***FIGURE 2.2***.

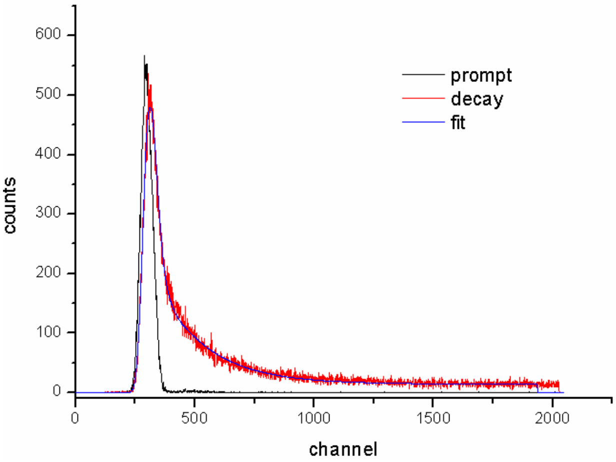

FIGURE 2.2. Emission lifetime measurement for blue emitting gold clusters (λ_{em} = 440 nm). A 2-exponential decay function is required to fit the data, with τ_1=0.93 ns, τ_2=5.75 ns (time calibration = 2.77E-11 s/channel).

2.4.2 Fluorescence in Bulk and Thin Film Samples

When the gold clusters are dispersed in a matrix, their emission properties remain basically unchanged, as shown in ***FIGURE 2.3*** and ***FIGURE 2.4***.

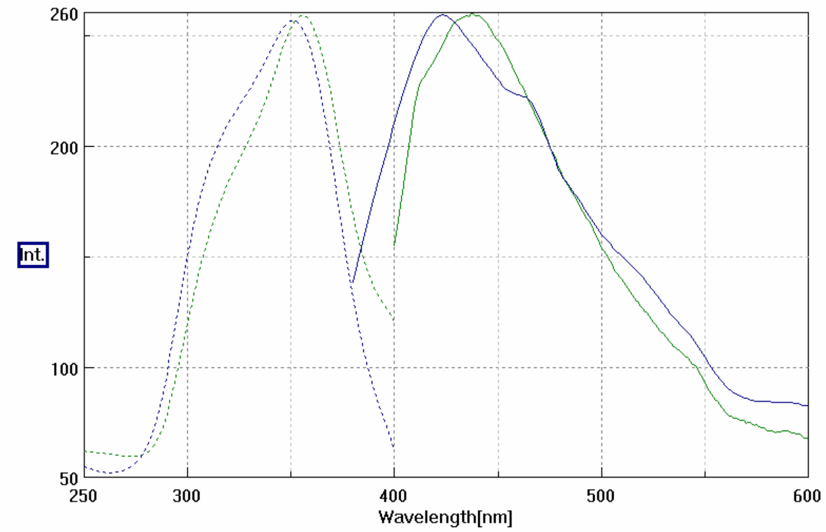

FIGURE 2.3. Emission (straight line) and excitation (dashed line) spectra for blue emitting gold clusters in solution (green) and in sol-gel silica (blue).

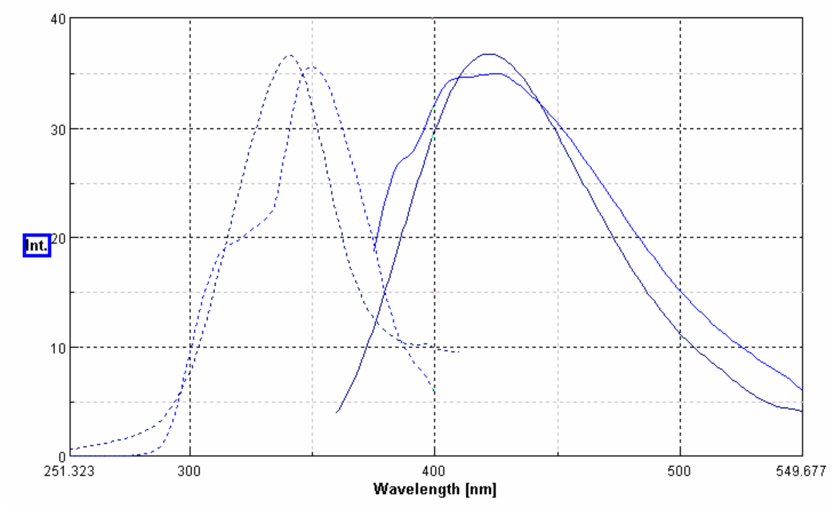

FIGURE 2.4. *Emission (straight line) and excitation (dashed line) spectra for blue emitting gold clusters in solution (dark blue) and in a hybrid copolymer matrix (light blue).*

The emission spectra overlaps, with a slight blue shift in the case of sol-gel silica matrix probably connected to the ligand exchange process. In fact, the few precipitation-redispersion steps necessary for the partial replacement of octadecanethiol ligands with mercaptopropyl-trimethoxysilane functional ligands and subsequent washing might determine a slight variation in the ratio of the emitting species population. A further possibility may arise from the interaction of the matrix with the cluster which is now chemically bound via the Si-O-Si-C_3-S-Au bond chain.

The facile redispersibility of the gold clusters, together with the wide variety of functionalities that can be attached to their surface through thiol ligand exchange processes, makes them potential candidates for the formation of luminescent nanocomposites also in the solid state.

2.4.3 Structural Characterization and Size-Emission Correlation

Due to the extremely small size of the clusters, only the red-emitting particles could be observed with TEM. As can be noticed in the micrograph (***FIGURE 2.5***), obtained by depositing a droplet of a colloidal solution on a copper TEM grid, the average diameter is 1 ± 0.3 nm. A diameter of 1 nm corresponds exactly to a 31-atom cluster: we can try to relate the cluster size to its emission wavelength, and verify this correspondence with one of the simple models proposed above. In particular, the jellium model provides an easy law where the energy spacing goes ~ $E_f/N^{1/3}$, where E_f is gold's bulk Fermi energy (5.5 eV) and N is the number of atoms in the cluster. The expected emission energy should be ~ 1.75 eV, versus an observed value of 1.96 eV. This non-neglectable difference, which is anyway close to 12%, derives from the fact that the sample characteristic dimensions are close to the instrumental limit to providing reliable measures, as the large standard deviation witnesses. Besides that, when N > 20 atoms a certain degree of unharmonicity should be taken into account.

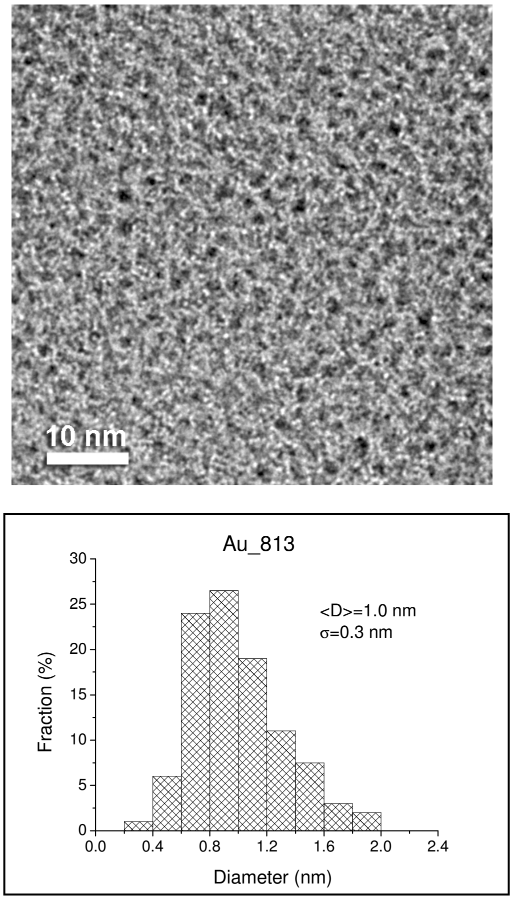

***FIGURE 2.5**. TEM bright-field micrograph of the red-emitting particles (top) with size distribution histogram (bottom).*

2.5 Conclusions

Small, highly fluorescent gold clusters can be easily prepared with a one phase, one pot synthesis at extremely mild conditions. The obtained clusters are chemically extremely stable, and can be easily redispersed in many organic solvents, showing tunable emissions in the near UV and visible range with efficient excitation in the UV. Furthermore, ligand exchange processes allow to extend their compatibility and range of functionalities. It's been shown that blue emitting clusters have been succesfully introduced in hybrid and sol-gel matrices without altering their emitting features. These properties, coupled with the characteristic ns lifetimes, suggested to investigate their potential as sensitizers for rare-earth species both for optical and biomedical applications: such studies are currently being conducted, with encouraging preliminary results.

2.6 References

1. Kreibig, U. & Vollmer, M. *Optical Properties of Metal Clusters* (Springer, 1995).
2. Haberland, H. *Clusters of Atoms and Molecules* (ed. Haberland, H.) (Springer-Verlag, 1994).
3. El-Sayed, M. A., *Accounts Chem. Res.* **34**, 257-264 (2001).
4. Whetten, R. L. et al., *Accounts Chem. Res.* **32**, 397-406 (1999).
5. Ozin, G. A. & Huber, H., *Inorg. Chem.* **17**, 155- 163 (1978).
6. Chen, W. et al., *J. Appl. Phys.* **83**, 3811-3815 (1998).
7. Peyser, L. A., Vinson, A. E., Bartko, A. P. & Dickson, R. M., *Science* **291**, 103-106 (2001).
8. Cleveland, C. L. et al., *Phys. Rev. Lett.* **79**, 1873-1876 (1997).
9. Link, S. et al., *J.Phys. Chem. B* **106**, 3410-3415 (2002).
10. Fedrigo, S., Harbich, W. & Buttet, J., *J. Chem. Phys.* **99**, 5712-5717 (1993).
11. Ashcroft, N. W. & Mermin, N. D. *Solid State Physics* (HOLT, Rinehart and Winston, New York, 1976).
12. Kubo, R. *J.Phys.Soc. Jpn* **17**, 975 (1962).
13. Schaaff, T. G., Knight, G., Shafigullin, M. N., Borkman, R. F. & Whetten, R. L *J. Phys. Chem. B* **102**, 10643-10646 (1998).
14. Wallace, W. T. & Whetten, R. L., *J. Am. Chem. Soc.* **124**, 7499-7505 (2002).
15. Campbell, C. T., Parker, S. C. & Starr, D. E., *Science* **298**, 811-814 (2002).
16. Sanchez, A. et al., *J. Phys.Chem. A* **103**, 9573-9578 (1999).
17. Peyser, L. A., Lee, T. H. & Dickson, R. M., *J. Phys. Chem. B* **106**, 7725-7728 (2002).
18. Chen, W., Joly, A. G. & Roark, J., *Phys. Rev. B,* **65**, art. 245404 (2002).
19. Felix, C. et al., *Phys. Rev. Lett.* **86**, 2992-2995 (2001).
20. Rabin, I. et al., *Chem. Phys. Lett.* **320**, 59-64 (2000).
21. Harbich, W., Fedrigo, S., Buttet, J. & Lindsay, D. M., *Z. Phys. Datoms Mol. Clusters* **19**, 157-159 (1991).
22. Harbich, W. et al., *J. Chem. Phys.* **93**, 8535-8543 (1990).
23. Altmann, S. L. *Band Theory of Metals* (Oxford, 1970).

24. Johnston, R. L. *Atomic and Molecular Clusters* (London and New York, 2002).
25. Kubo, R., *J. Phys. Soc. Jpn.* **17**, 975-& (1962).
26. Wertheim, G. K., Dicenzo, S. B. & Buchanan, D. N. E., *Phys. Rev. B* **33**, 5384-5390 (1986).
27. Knight, W. D. et al., *Phys. Rev. Lett.* **52**, 2141-2143 (1984).
28. Deheer, W. A. et al., *Phys. Rev. Lett.* **59**, 1805-1808 (1987).
29. Deheer, W. A., *Reviews of Modern Physics* **65**, 611-676 (1993).
30. Uchtmann, H., Rademann, K. & Hensel, F., *Ann. Phys.* **48**, 207-214 (1991).
31. Knight, W. D., Clemenger, K., Deheer, W. A. & Saunders, W. A., *Phys. Rev. B* **31**, 2539-2540 (1985).
32. Skala, L., *Theochem-Journal of Molecular Structure* **73**, 103-109 (1991).
33. Schmidt, M. & Haberland, H., *European Physical Journal D* **6**, 109-118 (1999).
34. Marcus, R. a. S. N., Physics and chemistry of small clusters / edited by P. Jena, B.K. Rao, and S.N. Khanna. (New York : Plenum Press, 1987).
35. Harbich, W., Fedrigo, S., Buttet, J. & Lindsay, D. M., *J. Chem. Phys.* **96**, 8104-8108 (1992).
36. Collings, B. A., Athanassenas, K., Rayner, D. M. & Hackett, P. A., *Chem. Phys. Lett.* **227**, 490-495 (1994).
37. Collings, B. A., Athanassenas, K., Lacombe, D., Rayner, D. M. & Hackett, P.A. *J. Chem. Phys.* **101**, 3506-3513 (1994).
38. Collings, B. A., Athanassenas, K., Rayner, D. M. & Hackett, P. A., *Z. Phys. D-Atoms Mol. Clusters* **26**, 36-40 (1993).
39. Boyen, H. G. et al., *Science* **297**, 1533-1536 (2002).
40. Kreibig, U., Fauth, K., Granqvist, C. G. & Schmid, G., *Zeitschrift Fur Physikalische Chemie Neue Folge* **169**, 11-28 (1990).
41. Feld, H., Leute, A., Rading, D., Benninghoven, A. & Schmid, G., *J. Am. Chem. Soc.* **112**, 8166-8167 (1990).
42. Wallenberg, L. R., Bovin, J. O. & Schmid, G., *Surf. Sci.* **156**, 256-264 (1985).
43. Schmid, G. et al., *Chem.-Eur. J.* **6**, 1693-1697 (2000).
44. Schmid, G. et al., *Chem. Soc.Rev.* **28**, 179-185 (1999).

45. Schmid, G., *Chem. Rev.* **92**, 1709-1727 (1992).

46. Liu, S. T., Maoz, R., Schmid, G. & Sagiv, J., *Nano Lett.* **2**, 1055-1060 (2002).

47. Schmid, G. & Liu, Y. P., *Nano Lett.* **1**, 405-407 (2001).

48. Wilcoxon, J. P., Martin, J. E., Parsapour, F., Wiedenman, B. & Kelley, D. F. *J. Chem. Phys.* **108**, 9137-9143 (1998).

49. Nilius, N., Ernst, N. & Freund, H. J., *Surf. Sci.* **478**, L327-L332 (2001).

50. Birnie, D. P., *J. Mater. Res.,* **16**, 1145-1154 (2001).

Chapter 3

Synthesis and Characterization of Fuorinated Polyimides Nanocomposites

3.1 Introduction

Nowadays a number of investigations are focused on the production of nanocomposite materials made up of metal nanoclusters embedded in organic matrices, owing to their unusual optical, electronic, magnetic and chemical properties[1,2]. In fact, the incorporation of metal particles in polymeric hosts allows their stabilization and prevents agglomeration, thus facilitating the fabrication into useful catalytic, optical and electronic devices. The optical properties of noble metal nanoparticles (Cu, Au, Ag) are related to a typical absorption peak in the UV-VIS range[3], known as surface plasmon resonance (SPR) peak, whose intensity, position and band-width are primarily affected by the size, size distribution and shape of the nanoparticles. Furthermore, since the SPR peak features are strongly correlated to the physico-chemical nature of the host medium[4,5], the possibility to exploit the optical properties of this kind of nanocomposites in the optical sensing field has received increasing attention[6,7]. Metal-polymer nanocomposites have been usually prepared by mixing metal particles with polymer solutions[8], by vacuum co-deposition procedures[9,10], by metal precursor doping and decomposition[11–14], and by ion implantation[15,16].

As for the choice of the matrix, in the field of organic polymers aromatic polyimides are characterized by absolutely peculiar properties from the mechanical (high tenacity and abrasion resistance), thermal ($T_g > 300°C$, $T_d >$

500°C, low coefficient of thermal expansion), dielectric (ε ~ 3) and chemical inertia (they are stable in a wide pH range both in acidic and basic conditions) point of view. Despite these exciting premises anyway they show some issues connected with their processability and intrinsic anisotropy. In fact, high density is achieved through a very efficient packing of the aromatic structures, which furthermore implies a very low solubility in organic solvents. At an industrial level, the problem has been avoided with processes that lead to the formation of the final product by thermally treating a polymeric precursor, polyamic acid, in its turn easily processable and soluble in a large variety of solvents. The so-prepared polyimides, known as Kapton® or Upilex® (***FIGURE 3.1***, originally developed and patented by DuPont), have several uses as dielectric, antistatic or protective films, in conditions that require elevated material performances, as these polymers are clearly non-conventional products with a relatively high cost.

Recent papers investigated the synthesis of metal clusters into commercially available polyimides obtained by ion-exchange technique followed by annealing in reducing atmosphere[17–20]. This method relies on a surface treatment of the bare polyimide films in KOH to produce a surface-modified polyimide layer (potassium polyamate) with ion-exchange capability. Thereafter, metal ions are introduced through ion-exchange with the bound potassium ions. By a subsequent annealing in reducing atmosphere, the re-imidization of the polyimide and the metal nanoparticle precipitation are promoted.

Unfortunately, commercial aromatic polyimides, like Kapton® or Upilex®, are not optically transparent in the whole visible range. Therefore, the study of the optical properties of metal clusters, which are known to exhibit their most interesting surface plasmon resonance features in that wavelength span is precluded. Among the different polyimides, fluorinated polyimides exhibit improved optical transparency in the visible range with respect to commercial polyimides[21]. However, it's been long known in literature that fluorination together with the presence of sterically cumbersome groups that are free to rotate around single bonds lead to the formation of compounds that are characterized by a good transparency in the visible and near infrared. Furthermore, solubility becomes significant in many polar aprotic organic solvents, thus making the processing much easier.

This features makes them good candidates for the production of metal-polyimide nanocomposites in which the optical properties of the nanoclusters are fully exploited.

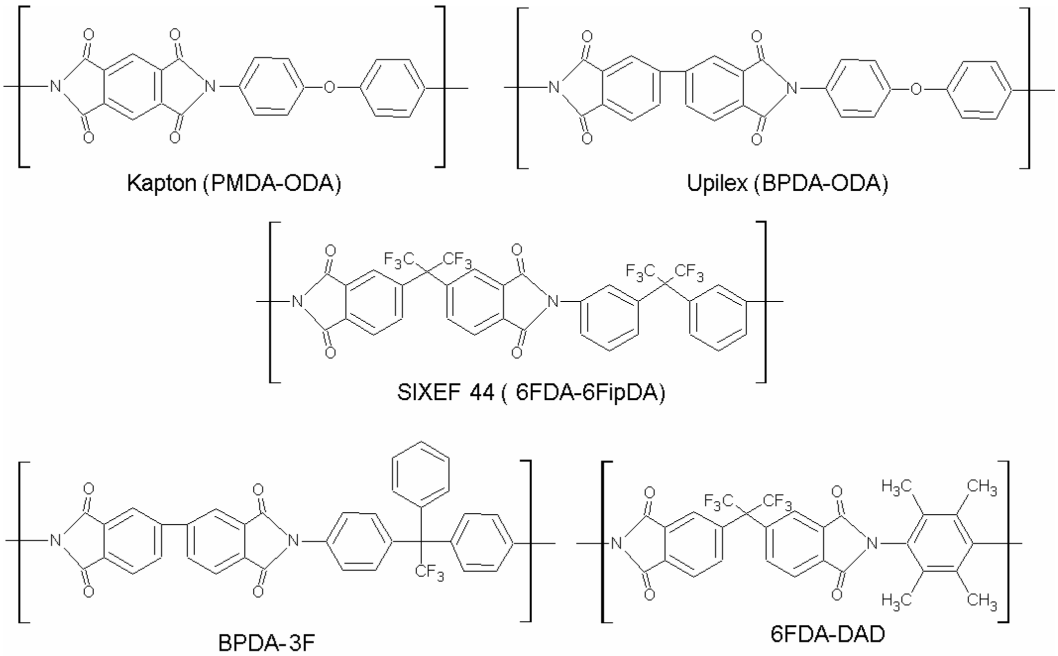

FIGURE 3.1. *Chemical structures of the 6FDA-DAD, BPDA-3F and 6FDA-6FipDA polyimides.*

3.2 Experimental

3.2.1 Synthesis of the 6FDA-DAD, BPDA-3F and 6FDA-6FipDA polyimides

The starting polyimides were 2,2'-bis(3,4-dicarboxyphenyl)-hexafluoropropane dianhydride 2,3,5,6-tetramethyl-paraphenylene diamine (diaminodurene) (6FDA-DAD), 3,3’,4,4’-dicarboxyphenyl dianhydride 1,1-bis(4-aminophenyl)-1-phenyl-2,2,2-trifluoroethane (BPDA-3F) and 4,4’-2,2'-bis(3,4-dicarboxyphenyl)-hexafluoropropane dianhydride 4,4′-diaminodiphenyl-2,2-

hexafluoropropane (6FDA-6FipDA) whose chemical structure is sketched in ***FIGURE 3.1***. All the reagents and the solvents used for the synthesis were purchased from Acros Chemicals, Aldrich and Fluka and purified prior to use, apart from the diamine 3F, which was synthesized as described in ***FIGURE 3.2***, according to the method proposed by Alston and Gratz[22].

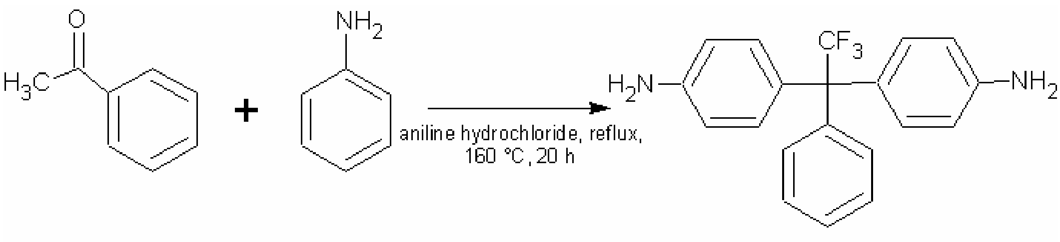

FIGURE 3.2. *Reaction scheme for the synthesis of the diamine 3F.*

The dianhydrides 6FDA and BPDA were sublimed under vacuum, whereas 2,3,5,6-tetramethyl-1,4-phenylenediamine (DAD) was purified by recrystallization from dichloromethane. The 4,4′-diaminodiphenyl-2,2-hexafluoropropane (6FipDA) precursor was of electronc grade and used as received. The polyimides were synthesized by following the two-step classical reaction scheme. The diamine was dissolved at room temperature in freshly distilled N-methyl-pyrrolidone under nitrogen flux. After a complete dissolution of the diamine an equimolar amount of dianhydride was added so as to obtain a solution 20% wt in solids that was stirred for 24 hours. A polyamic acid (PAA) solution forms through the condensation of anhydride and amine groups. The chemical imidization was obtained as follows. A solution of triethylamine and acetic anhydride (molar ratio 1:1) was added to the solution containing the polyamic acid, in such amount that the moles of triethylamine were fourfold the moles of each monomer. The resulting solution was stirred for 20 hours and then precipitated in methanol. The white polyimide powders were collected by filtration under reduced pressure, washed twice in water and twice in methanol and dried in air overnight and in vacuum at 200 °*C* for 15 hours.

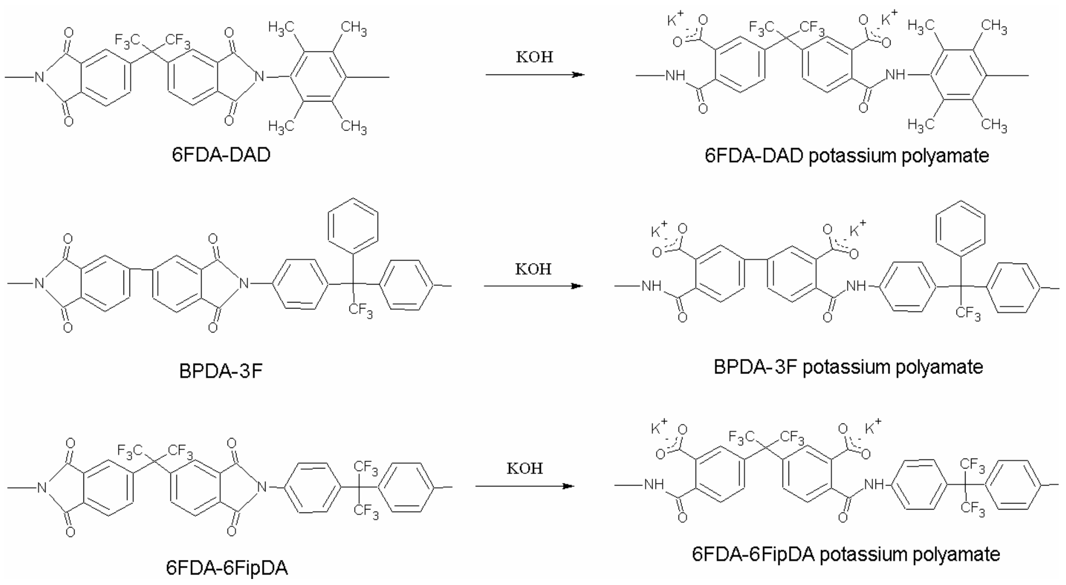

FIGURE 3.3. *Alkaline hydrolysis reaction scheme for polyimides in KOH.*

3.2.2 Preparation of composite films

Self-supporting thick films were obtained by the tape-casting technique, starting from the solution of each polyimide (10÷20% wt. solids) in N-methylpyrrolidone. Varying thicknesses in the 10÷200 μm range can be obtained by defining the number of tape stripe layers and the initial concentration.

Thin films were obtained by spin-casting polyimide solution of varying concentration at 1000÷6000 rpm in a dry atmosphere on silicon, fused silica or soda-lime glass substrates.

After drying in vacuum at 200 °*C* for 8 hours, the samples were immersed in KOH (or NaOH) 5M for time intervals ranging from 30 s up to 60 min at 45 °*C*. Polyimides react with KOH to give the salt potassium polyamate, as reported in ***FIGURE 3.3***. Subsequently, the samples were thoroughly rinsed in deionized water and immersed in a solution of $AgNO_3$ 50 mM at 45 °*C*, thus undergoing the ion-exchange process between potassium and silver ions. The K^+-Ag^+ ion-exchange reached the nearly complete saturation within the first minutes of treatment in $AgNO_3$ aqueous solution. Anyway, the ion-exchange procedure was performed for time intervals two times longer with respect to the KOH treatment time, in order to assure the complete substitution of all the potassium ions within the modified layer. When the gold nanocomposites were to be obtained, the procedure is analogous with the replacement of the $AgNO_3$ solution with a $HAuCl_4·3H_2O$ 10 mM.

Another strategy was adopted when instead of polyimides we chose to process polyamic acid precursors. In this case, the ring opening reaction in KOH 5M at 45 °*C* is replaced by a milder treatment in KOH 0.5M at room temperature. The remainder of the procedure is unaltered.

Thermal reduction of metals and particles aggregation were attained by annealing the samples in reducing atmosphere (H_2 12% - Ar) or air at temperatures lower than or near the glass transition temperature (T_g) values (200 °*C*, 300 °*C* and 350 °*C*) for 30 min.

3.2.3 Analytical techniques

Fourier transform infrared spectroscopy (FTIR) in the mode of attenuated total reflectance (ATR) with a standard ZnSe crystal was performed under vacuum at room temperature with a resolution of 4 cm^{-1} using a Jasco 660 Plus spectrometer.

Differential Scanning Calorimetry (DSC) was performed at a heating rate of 10 °*C* min^{-1} in N_2 (.ow rate of 100 sccm) with a TA Instrument, while Thermogravimetric Analysis (TGA) was conducted in static air with a NETZSCH Simultaneous Thermal Analyzer STA 409.

UV-vis transmission and absorption spectra were recorded using a Jasco V530 spectrometer, at ambient temperature.

In order to study the nanostructural features of the composite films X-ray diffraction spectra were collected in the mode Grazing Incidence X-ray Diffraction (GIXRD). The measurements were carried out using a Panalytical X'Pert Pro MRD X-ray diffractometer working in Parallel Beam geometry and equipped with an X-ray tube emitting CuKα radiation (λ CuKα = 0.154186 nm). During the GIXRD measurements, the incident X-ray beam was fixed at an incidence angle of 0.5° or of 1° while the detector was moved along the goniometer circle in the 2θ range between 10° and 90°. Cross sectional transmission electron microscopy (TEM) was carried out at CNR-IMM Institute in Bologna with a field emission gun FEI TECNAI F20 (S)TEM microscope operating at 200 kV.

The K and Ag concentration and in-depth distribution were analysed by Rutherford backscattering spectrometry (RBS) using a 2.0 MeV $4He^+$ beam (scattering angle $\theta = 160°$) at the INFN-Laboratori Nazionali di Legnaro. A low current density (<7 nA/mm^2) was applied in order to avoid sample overheating. According to the standard methodology of data analysis for the RBS technique, the experimental spectra were normalised to the total charge impinging on the sample and to the solid angle subtended by the detector. The backscattering data were analyzed using the commercial program RUMP[23].

Scanning Probe Microscopy measurements were performed on a DI (now Veeco) Nanoscope III Multimode Microscope. Due to the requirements of successive experiments, some of the samples were imaged in water with a liquid cell apparatus.

3.3 Results and discussion

3.3.1 Optical properties of the bare polyimides

The optical transmission spectra of the synthesized fluorinated polyimides (thickness of 30 μm) and of some commercial polyimides foils (25 μm thick) are compared in ***FIGURE 3.4***. Table 1 shows two parameters, which allow to better appreciate the different transparency between the tested polyimides: the transmission onset (cut-off wavelength) and the 80% transmission wavelength. Both parameters for the polyimides prepared in-house are much lower with respect to the commercial ones, thus pointing out their particularly high transparency which allows to appreciate the absorption band related to the surface plasmon resonance of silver and gold nanoclusters.

Polyimide	80% transmission wavelength (nm)	UV-visible cutoff wavelength (nm)
PI-2566	430	310
SIXEF 44	375	360
SIM 200	--	290
SPI-129	--	405
PI-2555	--	365
6FDA-DAD	355	295
BPDA-3F	435	375
KAPTON	800	455
UPILEX-R	700	425
UPILEX-S	>800	425

TABLE 3.1. *Onset and 80% transmission wavelengths from Uvvis spectra for 6FDA-DAD, BPDA-3F and commercially available polyimides.*

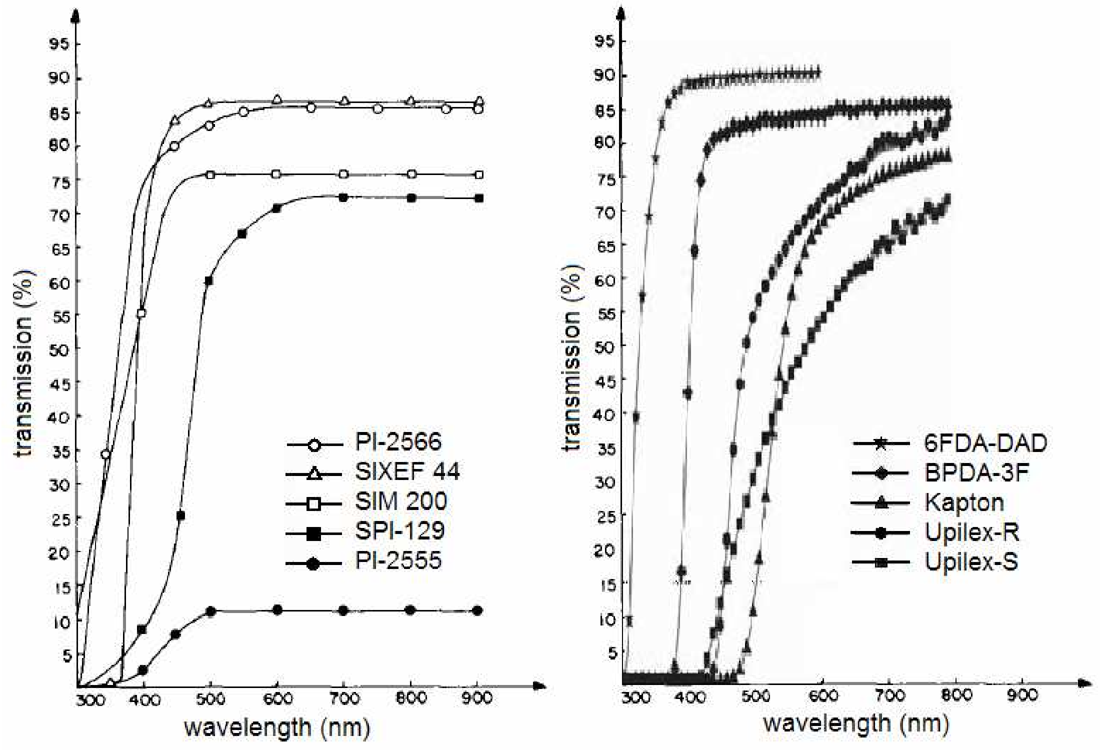

FIGURE 3.4. *UV-vis transmission spectra of the synthesized fluorinated polyimides compared with commercially available polyimides.*

3.3.2 Surface Modification of Polyimide Films

The structural changes in the polyimide samples during the nucleophilic attack with KOH for different times have been monitored by FT-IR spectroscopy.

As displayed in ***FIGURE 3.5***, the ring opening reaction caused by the nucleophilic attack of OH^- on the carbonyl carbon of the imide moiety is clearly evidenced by the decrease of the signals at about 1780 and 1720 cm^{-1}, assigned to the symmetric and asymmetric stretching of the carbonyl groups of the imide ring (imide I).

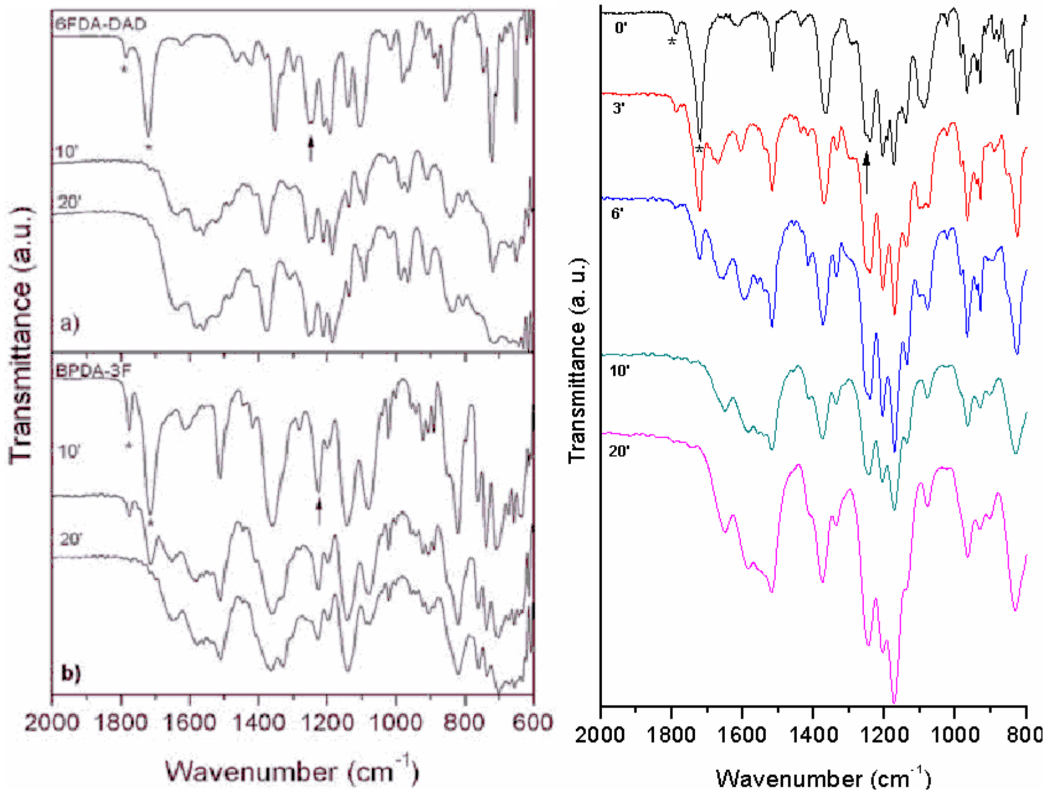

FIGURE 3.5. *ATR FT-IR spectra for polyimide films of 6FDA-DAD (a) BPDA-3F (b) and 6FDA-6FipDA (c) recorded after different treatment times in KOH 5M at 45 °C. The imide I spectral features are marked with an asterisk, whereas the reference band is indicated by the arrow.*

The new strong components that appear in the range 1660-1510 cm^{-1} after KOH treatment are ascribed to the presence of amide and carboxylate groups[24].

Therefore, the kinetics of the alkaline hydrolysis reaction with polyamate formation can be followed by observing the changes in the ratio of absorption of the imide I band near 1780 cm^{-1} with the absorption of a reference band (-CF_3 stretching in the range 1180-1260 cm^{-1} for both polyimides), as a function of the KOH treatment time, as reported in ***FIGURE 3.6*** for the three polyimides. After about 20 min treatment time the whole layer probed by the IR beam is modified by hydrolysis. It is clearly evident from the plot that 6FDA-based polyimides undergoes a more rapid nucleophilic attack with respect to BPDA-3F. After 10 min of immersion in KOH, the imide component is almost completely disappeared in 6FDA-DAD and 6FDA-6FipDA, whereas in BPDA-3F about 40% of the initial imide is still present. The different modification speed of the two types of polyimides could stem from the different reactivity of the imide carbonyl groups. In 6FDA-DAD and 6FDA-6FipDA the electron withdrawal action of the hexafluoroisopropylidene unit of the dianhydride portion promotes the reaction between the carbonyl carbon with the strong nucleophile OH^-, whereas the presence of the weak electron donating biphenyl group in BPDA-3F adversely affects the carbonyl reactivity towards the nucleophile attack.

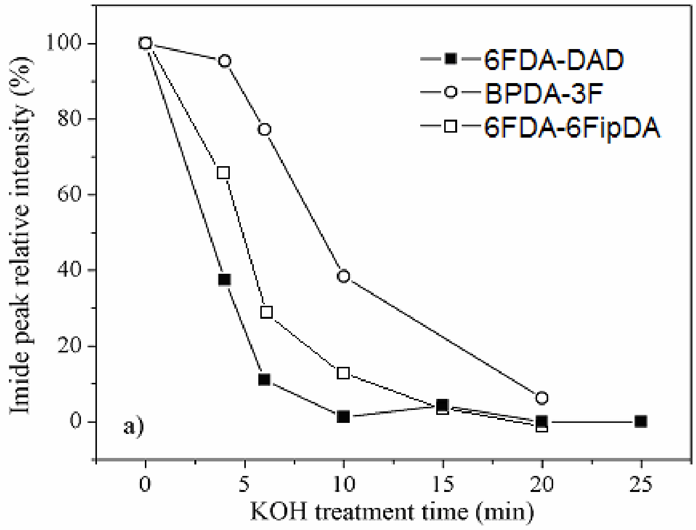

FIGURE 3.6. *Time evolution of the imide I peak intensity for the polyimides immersed in KOH 5M at 45 °C.*

Furthermore, the different response to the KOH treatment can be correlated to a different diffusion rate of the reactant OH^- through the macromolecules. As a matter of fact, it has been reported that 6FDA-DAD displays a much higher permeability than BPDA-3F[25]. This feature is correlated to the chemical structure of 6FDA-DAD, where both the presence of the bulky hexafluoropropane group $–C(CF_3)_2–$ in the dianhydride portion and the presence of methyl substituents in the *ortho* position of the diamine moiety, which adversely affects the free rotation of the phenyl group around the imide –C–N– bond, hinder the molecular linearity and co-planarity, thus preventing a tight stacking of the chains. Within this interpretation of the diffusion data, 6FDA-6FipDA shows an intermediate behavior, which can be explained with similar structure considerations. With the same dianhydride component, the slight varation in permeability is related to the different packing behavior of the DAD and 6FipDa moieties.

Hence, on the basis of the chemical structure, which is correlated to the permeability features, the interchain distance of 6FDA-DAD is expected to be higher than in BPDA-3F, thereby allowing a faster penetration of the nucleophile. XRD measurements have been performed to estimate the interchain distance of the bare polyimides, according to the procedure described by Kim and co-workers[26]. The XRD spectra of the untreated polyimides are reported in ***FIGURE 3.7***.

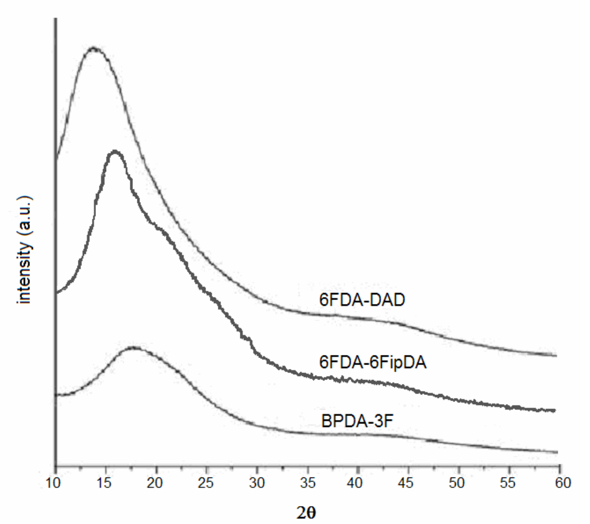

FIGURE 3.7. *XRD patterns of the bare polyimides.*

The amorphous scattering gives rise to a broad band, which implies a *d*-spacing distribution. From the Bragg's rule, the average *d*-spacing values can be obtained using the X-ray diffraction angle of maximum peak intensity (θ) and the X-ray radiation wavelength (1.54 Å). The calculation yields a *d*-spacing value of 4.83 Å for BPDA-3F, 5.53 Å for 6FDA-6FipDA and 6.32 Å for 6FDA-DAD. As expected, the average interchain distance in the latter polyimide is higher, thereby confirming that the higher hydrolysis rate observed for 6FDA-DAD with respect to BPDA-3F can derive from the higher diffusion rate of KOH through the 6FDA-DAD polyimide, with 6FDA-6FipDA showing an intermediate behavior.

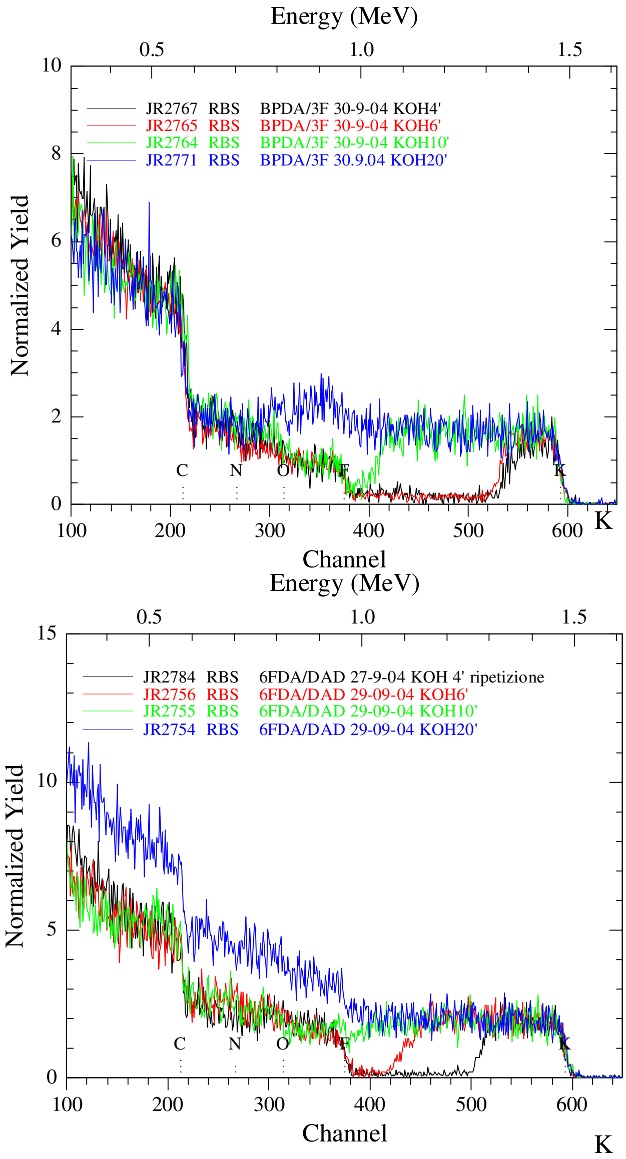

FIGURE 3.8. *RBS spectra of BPDA-3F (top) and 6FDA-DAD (bottom) after treatment in KOH 5M at 45°C for increasing times.*

In ***FIGURE 3.8*** the RBS spectra of BPDA-3F and 6FDA-DAD after treatment in KOH are reported as an example. The channel corresponding to the energy of He particles backscattered by the different species located at the surface of the film is labeled on the axis. The total amount of loaded K atoms as a function of the treatment time in KOH is given in the plots of ***FIGURE 3.9*** for BPDA-3F and 6FDA-6FDA polyimides.

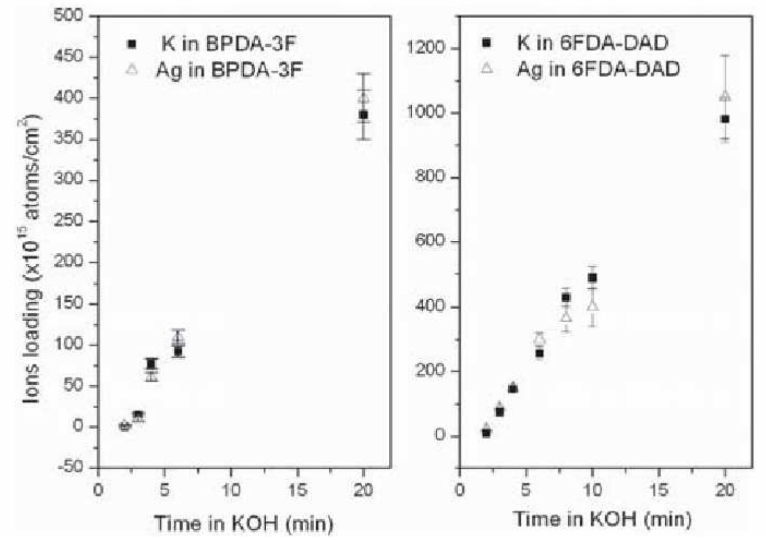

FIGURE 3.9*. Loading of K and Ag atoms in BPDA-3F (left) and 6FDA-DAD (right) as a function of treatment time in KOH.*

A strong correlation between the degree of alkaline hydrolysis as evidenced by FTIR analyses and the amount of loaded silver ions is evident: for the same treatment time in KOH the polyimide 6FDA-DAD allows the incorporation of a much greater amount of silver with respect to BPDA-3F and 6FDA-6FipDA, as a result of higher reactivity, higher permeability towards the OH- nucleophile and higher structural density of carboxylate groups. A homogeneous in-depth concentration of potassium of about 3.7% at. in 6FDA-DAD, 3.0% at. in BPDA-3F and 2.8% in 6FDA-6FipDA has been detected in the modified surface layer. It is worth to note that by taking into account the chemical formula of each polyimide repeating unit ($C_{29}H_{18}O_4N_2F_6$ for 6FDA-DAD, $C_{36}H_{19}O_4N_2F_3$ for BPDA-3F and $C_{34}H_{14}O_4N_2F_{12}$ for 6FDA-6FipDA), the measured atomic percentage demonstrates that the ratio of K ions:polymer repeating unit is about 2:1, thereby proving that the reaction of the polyimide with KOH is complete and both the imide rings present in each repeating unit are converted in carboxylate anions coordinated with K ions. The K penetration depth has been obtained from the simulation with the RUMP code of each recorded RBS spectrum and the results are reported in ***FIGURE 3.10***.

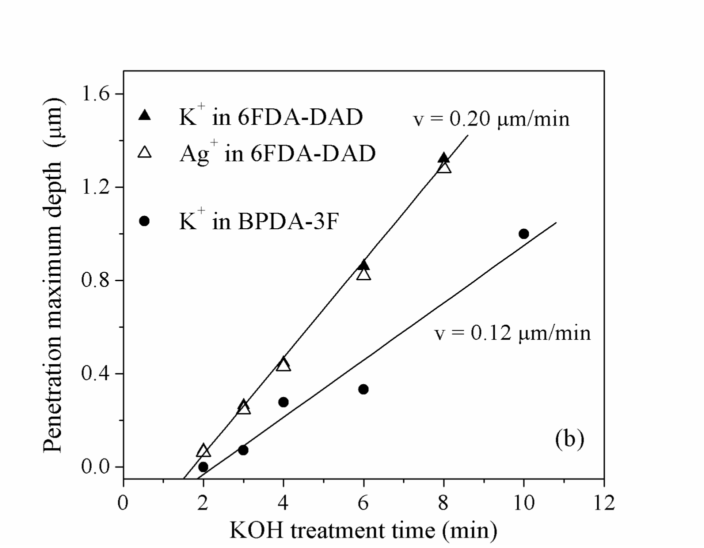

FIGURE 3.10. *Penetration depth for K vs. time treatment in KOH. For 6FDA-DAD the penetration depth of Ag is also reported, in order to highlight the complete exchange between K^+ and Ag^+ ions. The linear fits allow to estimate the speed of the K penetration process.*

The linear trend exhibited by the samples as a function of the treatment time for both the polyimides indicates that the chemical reaction between KOH and the polyimide, regulating the K penetration, is a first order process within the KOH treatment time interval used in these experiments. Moreover, the K penetration rate, as obtained by RBS measurements, is higher in 6FDA-DAD (0.20 ± 0.02 μm/min) than in BPDA-3F (0.12±0.02 μm/min), thus confirming the results obtained from FT-IR analyses. In fact, the same results can be derived from FT-IR measurements taking into account the depth of penetration of the evanescent wave in the ATR setup. The observed absorption is integrated over the whole sampled volume, thus allowing to obtain the modification rate, with the sole assumption that the modification front is homogeneous and flat throughout the polyimide. The depth of penetration d_p of the evanescent wave, defined as the distance required for the electric field amplitude to fall 1/e of its value at the surface, is given by

$$d_p = \frac{\lambda}{2\pi n_1 \sqrt{\sin^2\theta - \left(\frac{n_2}{n_1}\right)^2}}$$

where λ is wavelength of light, θ is the angle of incidence, n_1 and n_2 are the refractive indices of the ATR crystal and the sampled material respectively.

Effective penetration depths for ZnSe ($n_{ZnSe} = 2.4$) and Ge ($n_{Ge} = 4.0$) ATR crystals are given as a function of wavenumber (cm^{-1}) in ***FIGURE 3.11***.

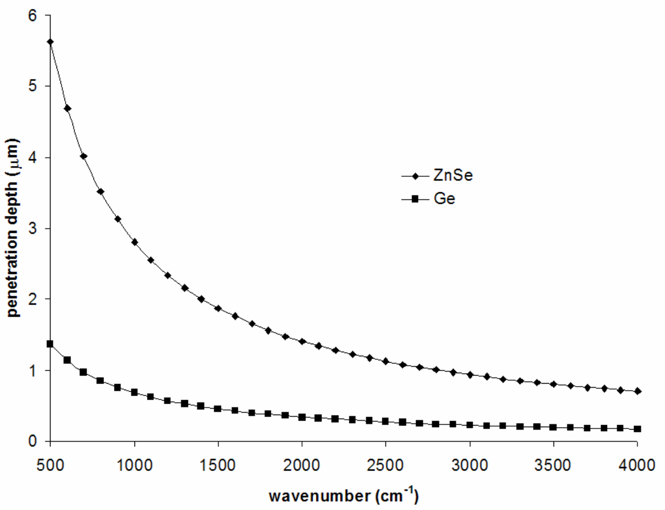

FIGURE 3.11. *Effective penetration depth for an IR beam as a function of wavenumber for two common ATR crystals.*

As far as the process of Ag doping is concerned, RBS analysis detected a complete emptying of K, as a result of the treatment in $AgNO_3$ solution and a 1:1 substitution of K^+ by Ag^+ within the experimental errors in all the samples, as can be observed from the data of ***FIGURE 3.10***, obtained from the spectra shwon in ***FIGURE 3.8*** and ***FIGURE 3.12***. As a matter of fact, Ag exhibits a flat concentration profile (3.7% at. in 6FDA-DAD and 3.0% at. in BPDA-3F) and its penetration depth is determined by the thickness of the KOH modified layer.

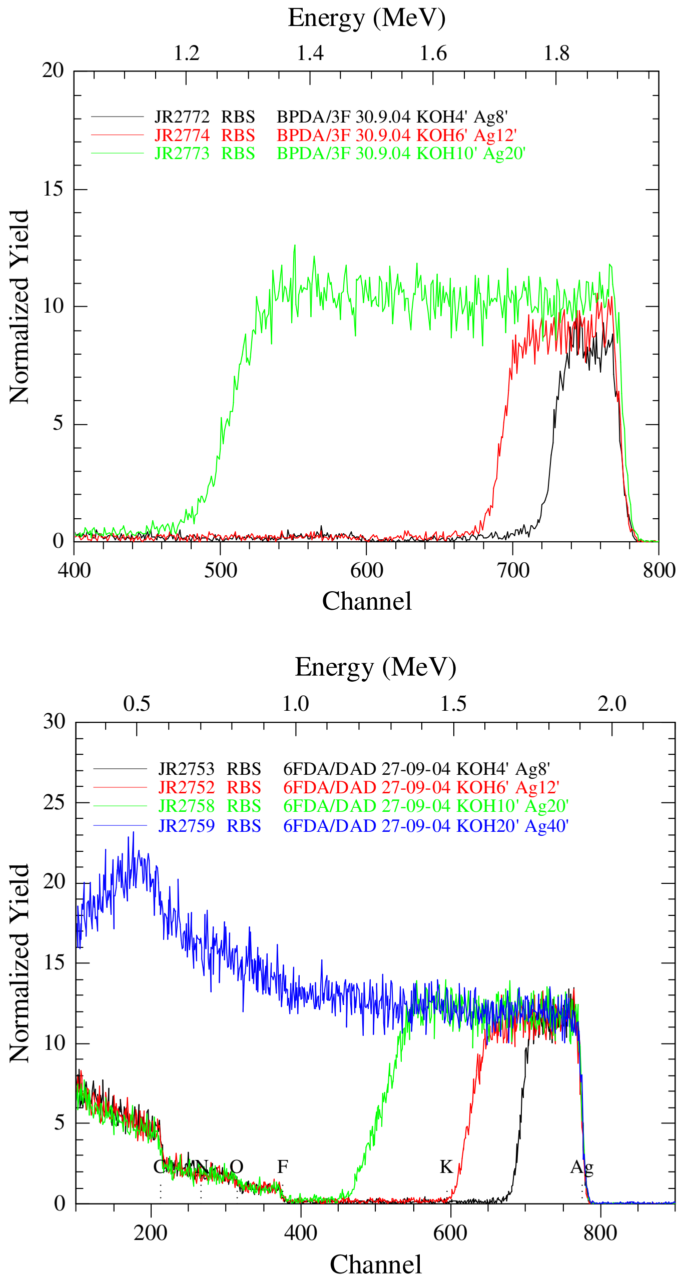

FIGURE 3.12. *RBS spectra of BPDA-3F (top) and 6FDA-DAD (bottom) after treatment in KOH 5M at 45°C for increasing times.*

On the other hand, no silver was detected in polyimide thin films which did not undergo any pre-treatment in KOH before the immersion in $AgNO_3$ aqueous solution, thus indicating that the step of potassium polyamate salt formation is needed to achieve the Ag doping of the polyimide. The concentration profile of Ag was also measured in the samples after thermal treatments at 200 and 300 °*C* in reducing atmosphere and air. The influence of the annealing temperature on the Ag in-depth distribution is negligible, thus indicating that silver reduction and clusters formation and growth occur uniformly within the depth without significant migration phenomena.

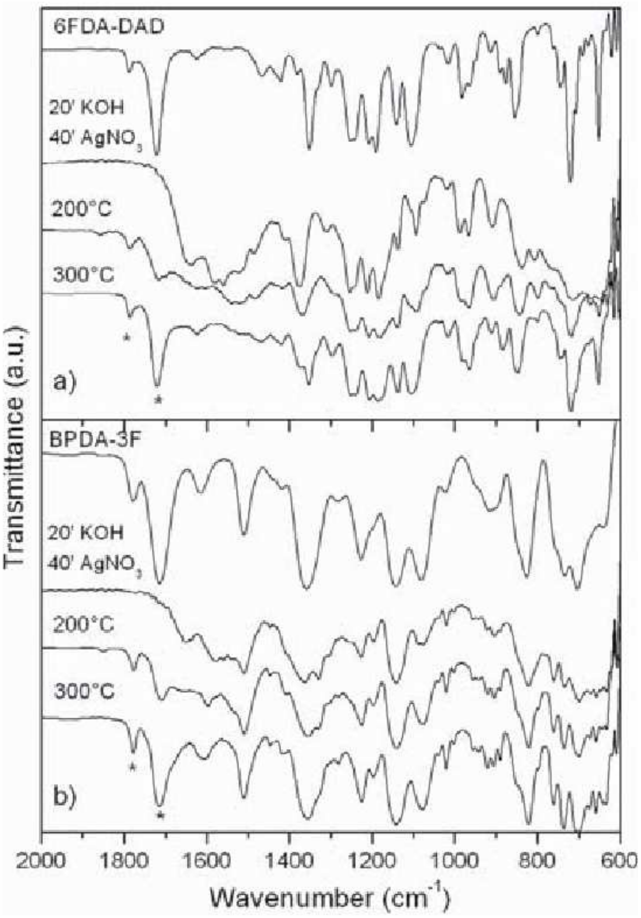

FIGURE 3.13. *ATR FT-IR spectra of polyimides after treatment in KOH for 20 min followed by ion exchange in AgNO3 solution and annealing at 200°C and 300°C for 30 min. The imide I spectral features are marked with an asterisk.*

FT-IR spectra recorded after ion-exchanging and after the subsequent annealing of the ion-exchanged samples at 200 °*C* and 300 °*C* are reported in Figure 8 for the three polyimides. The ion-exchange process introduces slight variation in the peak structure between 1200 and 1550 cm^{-1}, as shown in ***FIGURE 3.13*** and further discussed in the next paragraph, while the peak intensity remains unchanged thus confirming the lack of ion migration or further ring-opening reaction during the exchange process. The recovery of the pristine polyimide structure is almost complete upon annealing at 300 °*C* for both polyimides, as evidenced by the reappearance of the typical imide I spectral features at 1780 and 1720 cm^{-1}.

3.3.3 Surface Modification of the Polyamic Acid Films

In a different approach, polyamic acid films were treated directly with silver and gold solutions, offering an alternative and milder synthetic route to the formation of nanocomposites. In fact, the harsh alkaline treatment was originally motivated by the intent of imparting novel properties to the relatively cheap and widely available first commerical polyimides, namely Kapton® and Upilex®. As mentioned in **CHAPTER 1**, the lack of solubility of these compounds didn't allow for a straightforward mixing of the components, thus forcing the researchers to think of alternative strategies for introducing metallic species in the polymer.

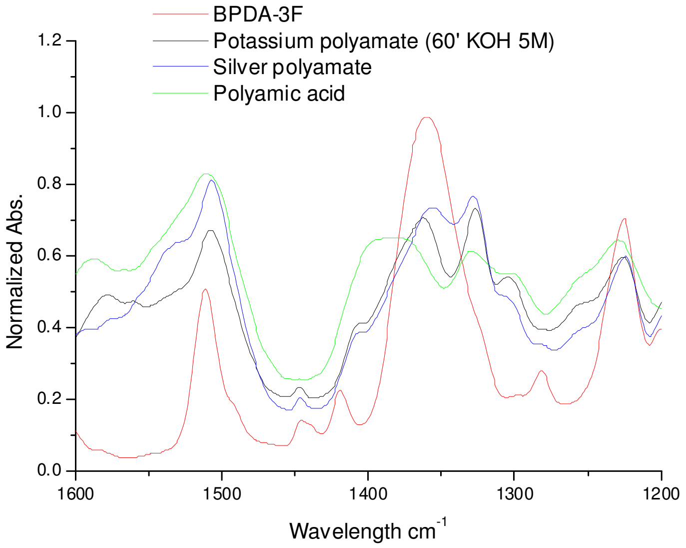

FIGURE 3.14. *FTIR spectra for the bare BPDA-3F polyimide, compared with the ion-exchanged, polyamate samples samples and the corresponding polyamic acid. Notice in the 1400 – 1350 cm-1 range the different peak structure related to the COO-/COOH group, with the appearance at 1400 cm-1 of a peak connected with the C=O group of the polyacid.*

However, when polyamic acid precursors are available, the direct mixing with metal salts or other species (nanoparticles, molecules) is feasible, the only drawback consisting in the lost of the fine depth profile control granted by the surface modification route. Furthermore, the presence of carboxy and amide groups on the polymer backbone makes polyamic acid a compound of great hydrophilicity and water permeability while maintaining its insolubility in aqueous solutions. Therefore, polyamic acid thick (self-sustaining, 30 μm) and thin (spin-casted, 0.1÷3 μm) films have been treated with $AgNO_3$ 50 mM and $HAuCl_4 \cdot 3H_2O$ 10 mM aqueous solutions at room temperature, in significantly milder condition than the ones used when the same ions had to be introduced in the corresponding polyimides.

The slight FTIR spectral differences between polyamic acid and polyamate samples highlighted in ***FIGURE 3.14*** account for the different resonance of carboxylate salt and carboxylic acid group. In fact, the high electron delocalization between the two oxygen atoms in the carboxylate results in the symmetric CO_2^- stretching at 1360 cm^{-1}, while in the carboxylic acid the C=O stretching and O-H deformation are combined in a band around 1400 cm^{-1}.

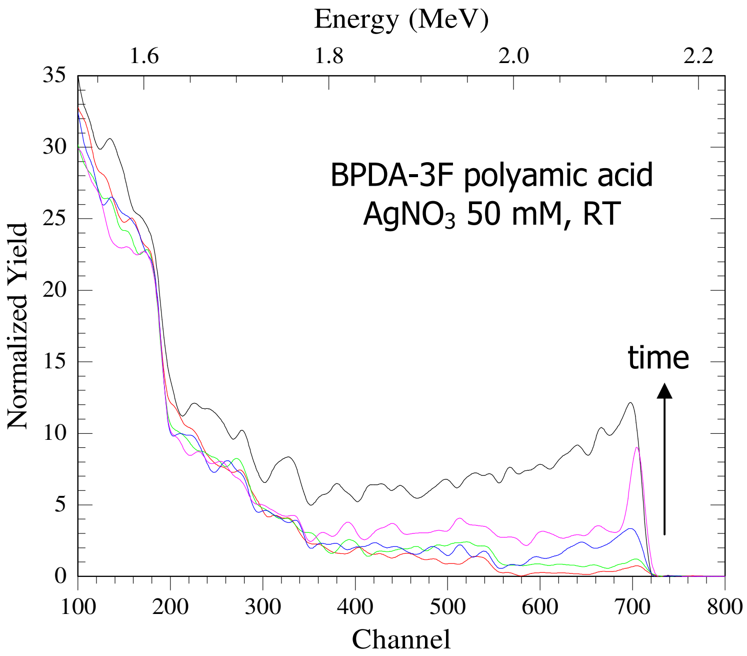

FIGURE 3.15. *RBS spectra for BPDA-3F polyamic acid treated with $AgNO_3$ at room temperature for 30 sec, 1 min, 4 min, 6 min, 10 min.*

RBS measurements were performed on a first series of samples for times going from 30 sec to 10 min, and the spectra are reported in ***FIGURE 3.15*** and ***FIGURE 3.16.***

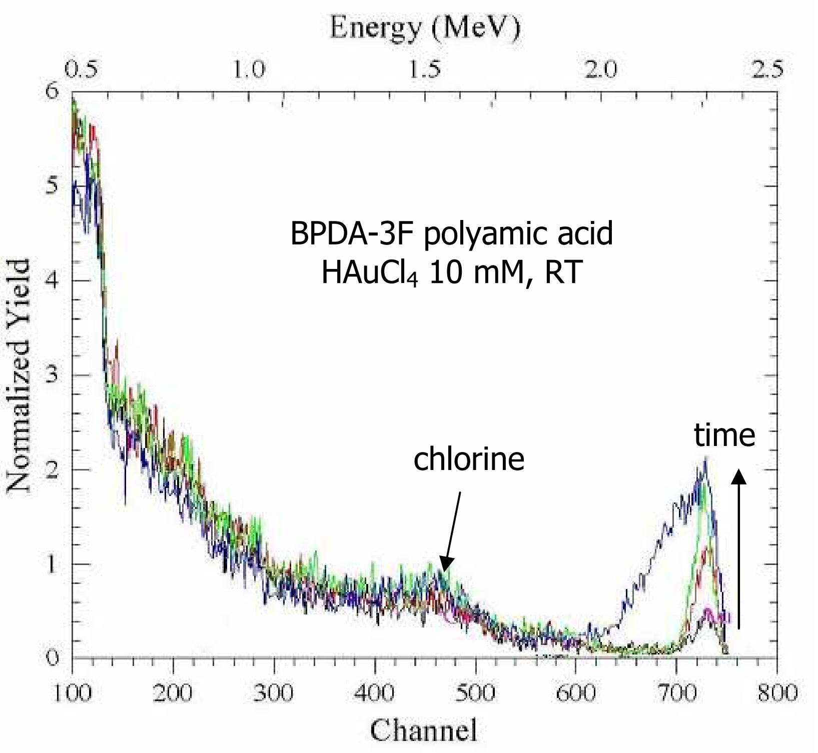

FIGURE 3.16. *RBS spectra for BPDA-3F polyamic acid treated with* $HAuCl_4 \cdot 3H_2O$ *at room temperature for 30 sec, 1 min, 4 min, 6 min, 10 min.*

In the case of Ag^+ ion introduction, the first striking difference with respect to the films obtained via surface modification of polyimides with alkali is the different behavior with time of the depth profile. When K^+ is exchanged with Ag^+ in a polyimide that has been treated with KOH 5M at 45°C, silver ions replace potassium atoms in the polyamate groups formed by the basic ring opening reaction. The experimental conditions are such that in all the heterocyclic imide rings only one C-N bond is broken, preserving molecular weight and linear structure of the polymeric chain; at the same time, the formation of polyamate moieties make the local environment relativley hydrophilic, allowing the aqueous solution to permeate the modified polymer layer and to attack the underlying one. Basically all the imide rings in an ideal layer have to be open, and therefore made hydrophilic, before the modification can proceed deeper. The resulting depth profiles for K^+ are therefore sharp and saturated, as they show a box-like shape where the atomic density is constant and the modified depth increases linearly with time. As K^+ is exchanged with Ag^+, the latter just replaces potassium atoms and reproduces its concentration profile.

When a polyamic acid sample is put in contact directly with an aqueous silver solution, the hydrophilicity of the carboxylic acid moieties allows for a rapid permeation of the matrix, while the H^+-Ag^+ is somewhat slower due to the relatively high pk_a of polyamic acids. The resulting profile is therefore flat and the atomic distribution deeper than the probing depth of the RBS technique even for extremely short permeation times. Longer times of treatment determine a homogeneous increase with depth of the atomic concentration.

The effect of temperature has been studied in a series of experiment aimed at finding for what time/temperature values the same concentration profile can be obtained. A BPDA-3F polyamic acid film has been treated with a 50 mM $AgNO_3$ solution a different time and temperatures, and the resulting RBS spectra for the matching couples of time/temperature values are shown in ***FIGURE 3.17***.

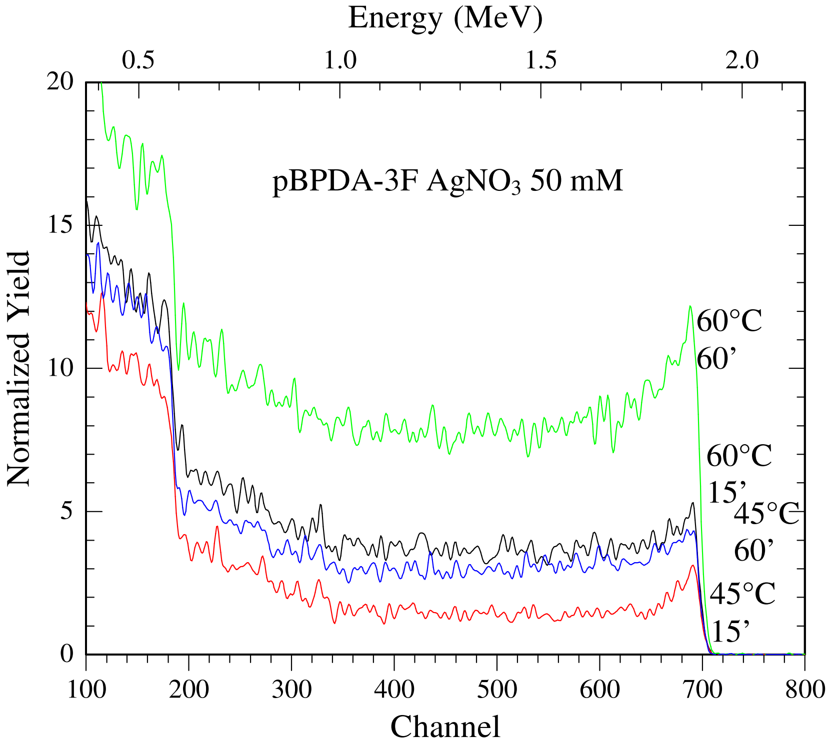

FIGURE 3.17. *RBS spectra for a BPDA-3F polyamic acid film treated with a 50 mM $AgNO_3$ solution at 45 and 60°C, for 15 and 60 min.*

As can be noticed, a 60 min treatment at 45°C yields a profile similar to the one obtained by a 15 min treatment at 60°C. Temperature therefore has as expected a significative effect in the cation diffusion velocity in the film.

Silver(I) is one of the few transition metal atoms that exists as an uncomplexed monovalent cation in aqueous solutions. Metals, especially when considering multivalent cations, usually show some degree of anionic complexation, therefore making the species that are actually diffusing much bulkier and with a charge that is often a function of pH.

Gold (III) in particular is invariably complexed in all solutions, usually as an anionic species of mixed chloro-aqua and chloro-hydroxo type, products of $AuCl_4^-$ hydrolysis (3). Gold (III) displays a predominantly square coordination. Although there is little evidence for any persisting five-coordinate complexes, there is no doubt that substitution reactions proceed via five-coordinate intermediates[27].

At 10 mM, the pH of the solution is 1.5 and gold exists as $AuCl_4^-$. Increasing the pH by introducing basic aprotic compounds or by lowering the gold tetrachloride concentration yields an increasing amount of aqua or hydroxo species, as shown in the scheme reported in ***FIGURE 3.18***.

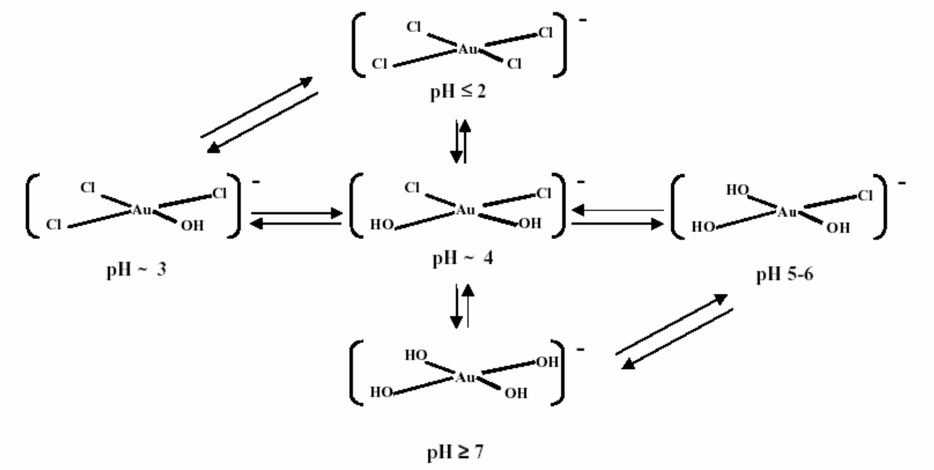

FIGURE 3.18. *pH dependence of Au(III) chloro complexes in aqueous solutions.*

The square planar tetrachloro complex is negatively charged, and can't substitute protons or ionic alkali ions in the same fashion as Ag^+ does. The doping of polyamic acid with gold is therefore connected to a mechanism of impregnation of the matrix, that relies only on the hydrophilicity and permeability of the polymer and not on the availibility of any specific binding site. RBS spectra show a peak at the surface whose intensity increases with time, until it reaches a saturation point after which the species start diffusing in the bulk.

3.3.4 Thermal Analysis

In order to determine the curing profiles and potential differences in the behavior of polyamic acid and corresponding polyamate salts, ramped and isothermal DSC analyses were performed on 6FDA-DAD and BPDA-3F polyamic acids before and after $AgNO_3$ treatments, while for 6FDA-6FipDA a ramped DSC was performed on a polyimide sample treated for 60 min with KOH and exchanged with Ag^+ to verify the presence of phenomena associated to crystalline silver compound formation.

When the temperature is ramped at 10°C/min, two distinct endothermic peaks can be observed in the 50÷150°C and 150÷250 ranges for all the three polyimides, as reported in ***FIGURE 3.19***. The first one can be ascribed, for 6FDA-DAD and BPDA-3F, to solvent decomplexation: polyamic and polyamate all offer hydrogen bonding sites where the carboxyl moiety on the solvent (N-methyl pyrrolidone, N-dimethyl formamide or N-dimethyl acetamide) can strongly interact. In the case of 6FDA-6FipDA, NMP cannot be present since it has been completely removed in the imidization process. Instead, water is present as witnessed by the 110 °C endothermic peak. The second endothermic peak is assigned to the imidization reaction, accompanied by the release of water molecules as a byproduct.

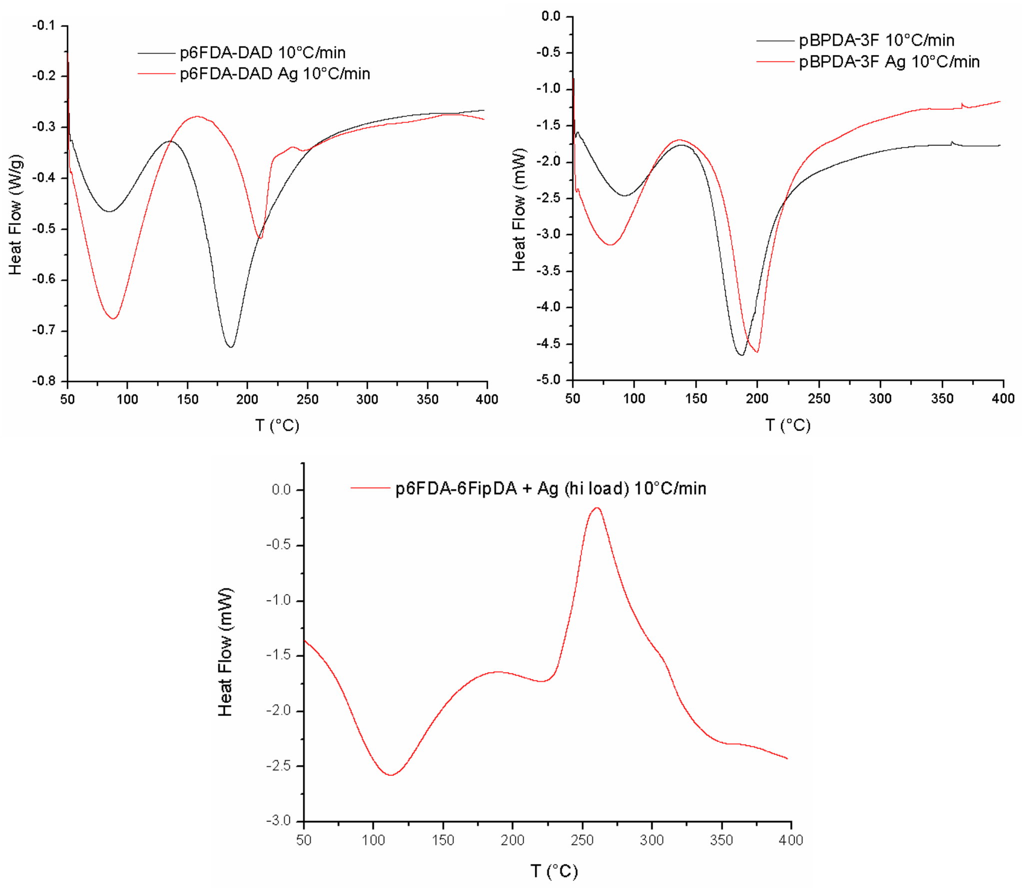

FIGURE 3.19*. DSC thermogram for the three polyimides, with a temperature ramp of 10°C/min.*

The overall decomplexation-imidization process can be described as follows: the polyamic acid exhibits four functional groups per unit able to form hydrogen bonds, the only kind of interaction strong enough to be responsible for the complexation. With rising temperature the NMP bound to the amide and acid groups is set free, and uncomplexed polyamic acid is obtained. After final decomplexation the carboxyl and amido groups are left highly reactive and most likely hardly selective. Therefore, two paths are open to lower the energy content of the system: the nucleophilic attack of a carbonyl carbon by the free electron pair of either the amide nitrogen or the acid hydroxy oxygen. The former leads under water elimination to the thermodynamic very stable imide, whereas the latter leads to the highly reactive anhydride under elimination of an amine. The anhydride formation is a reversible process in which amic acid formation is favored strongly. Possible hydrogen bonds between a polyamic acid and NMP molecules together with possible imidization reaction pathways are shown in ***FIGURE 3.20***.

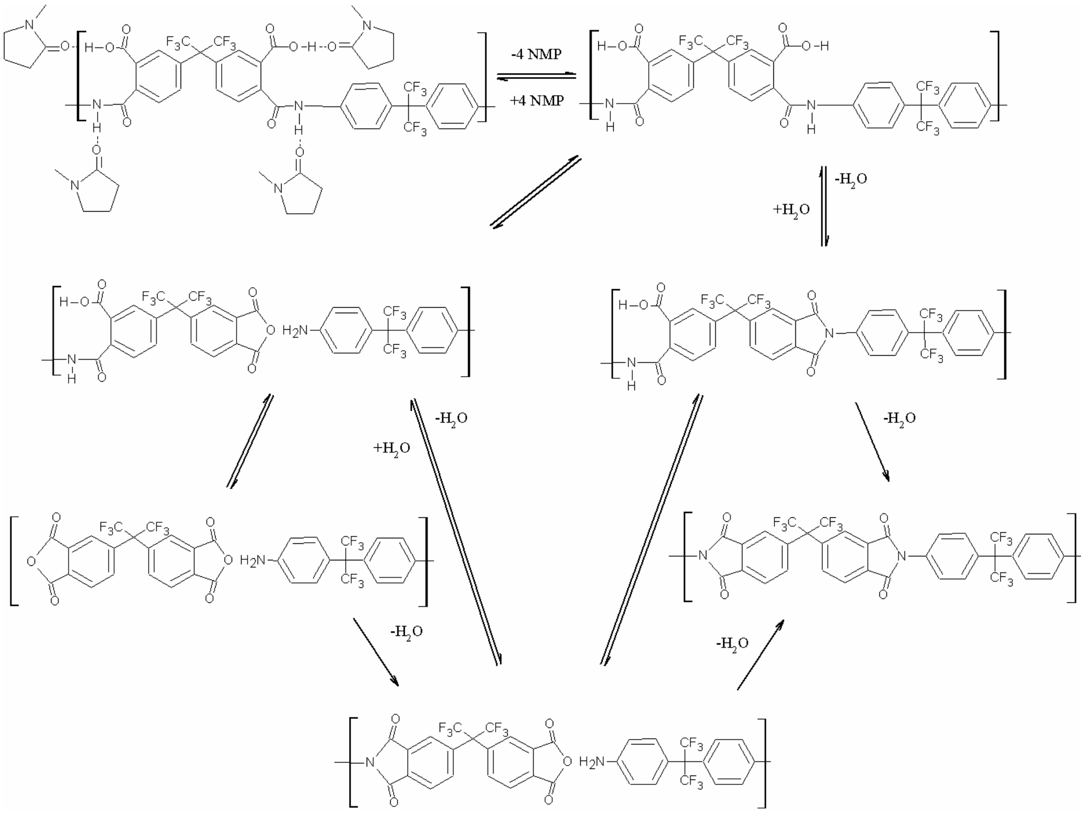

***FIGURE 3.20**. 6FDA-6FipDA polyamic acid imidization process: decomplexation of NMP solvent molecules and possible imidization pathways.*

It's interesting to notice how the imidization temperatures results slightly higher when silver polyamate salts are treated in the same experimental conditions as the polyamic acids. A possible explanation for such a difference might consist in the reduced electronegativity of the carbon atom in the carboxylate group due to electron delocalization with respect to the carbon atom in the carboxyl group of the acid. As the imidization process goes through the nucleophilic attack of the electron pair of the amide nitrogen on this carbon, the formation of the salt might reduce the reactivity of this moiety. The imidization temperatures for the mentioned compounds are reported in ***TABLE 3.2***.

T in °C	x_{imid} polyamic	x_{imid} Ag polyamate	w_{imid} polyamic	w_{imid} Ag polyamate
BPDA-3F	188	196	33	36
6FDA-6FipDA	-	227	-	49
6FDA-DAD	187	210	43	22

TABLE 3.2. *Imidization peak position and width for the polyamic and silver polyamate compounds.*

The strong endothermic peak observed at T > 270 °C for 6FDA-6FipDA can be related to the significantly higher silver loading of this sample. After treatment, the film is significantly frail and shows a dark discoloration. XRD analyses show the presence of metallic silver nanopartciles with a grain size of ~ 6 nm, whose clustering might easily result in a dark, opaque color.

Isothermal DSC thermograms were collected at 200°C, and for BPDA-3F one extra sample was measured below the imidization temperature at 150°C (***FIGURE 3.21)***. As can be noticed, the heat flow curve is basically flat after 30 minutes of treatment, thus implying that the imidization process is complete. Such result is confirmed by the previously shown FTIR spectra, where imide features were fully restored after analogous thermal treatments. When the polyamic/polyamate samples are treated below the imidization temperature, the only reaction that takes place is the solvent molecule decomplexation which is accompanied by a significantly smaller energy absorption by the polymer system.

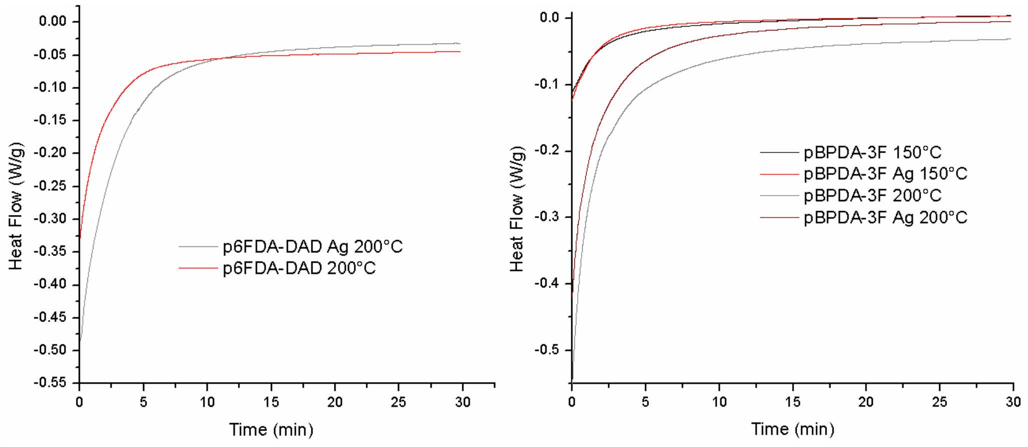

FIGURE 3.21. *Isothermal DSC thermograms for the three polyimides.*

3.3.5 Surface Morphology Characterization

The study of the surface morphology of the polyimide samples is particularily meaningful as it can provide information not only on the surface quality of the film, intended as any of roughness evaluation parameters, but also on the specific type of possible defects arising from the film processing steps.

The film casting technique already marks a significative difference: tape casting yields thick, self-sustaining films, but the top and bottom surfaces, i.e. the film surface that was originally contacted with the glass substrate and the surface in contact with air, show a different behavior with respect to permeability to the aqueous solutions. Such differences arise from the solvent gradient during its evaporation in the drying process steps, and result in a gradient in the effectiveness of the packing between the chains in a direction normal to the surface, with a higher permeability on the glass-oriented side. As the solvent evaporates from the top part of the film, it is quickly replaced by other solvent molecules diffusing up from the bottom part. As the solvent has a plasticizing effect, it’s clear how polymer chains that are closer to the interface with glass have less time to rearrange in a denser packing than the molecules that are closer to the interface with air.

In the KOH treatment, higher permeability implies a higher and less controllable rate of modification, and thereforein order to obtain more reproducible results the part we considered in the surface studies is always the one that was dried in contact with the atmosphere.

It’s already been shown how the three polyimides have different interchain distances, chemical resistance to alkalis and consequent modification rates. Therefore, different surface morphologies might result from the alkaline ring-opening reaction. The surfaces of samples treated in KOH 5M at 45°C for 10 min are reported in ***FIGURE 3.23***.

Quite surprisingly, 6FDA-6FipDa shows a reduced flatness after the alkaline attack, that yields an estremely smooth surface. While of relatively scarce importance in this context, this aspect will be fundamental when polyimides will be used as a substrate for liquid cell atomic force microscopy of DNA structures in **CHAPTER 4**.

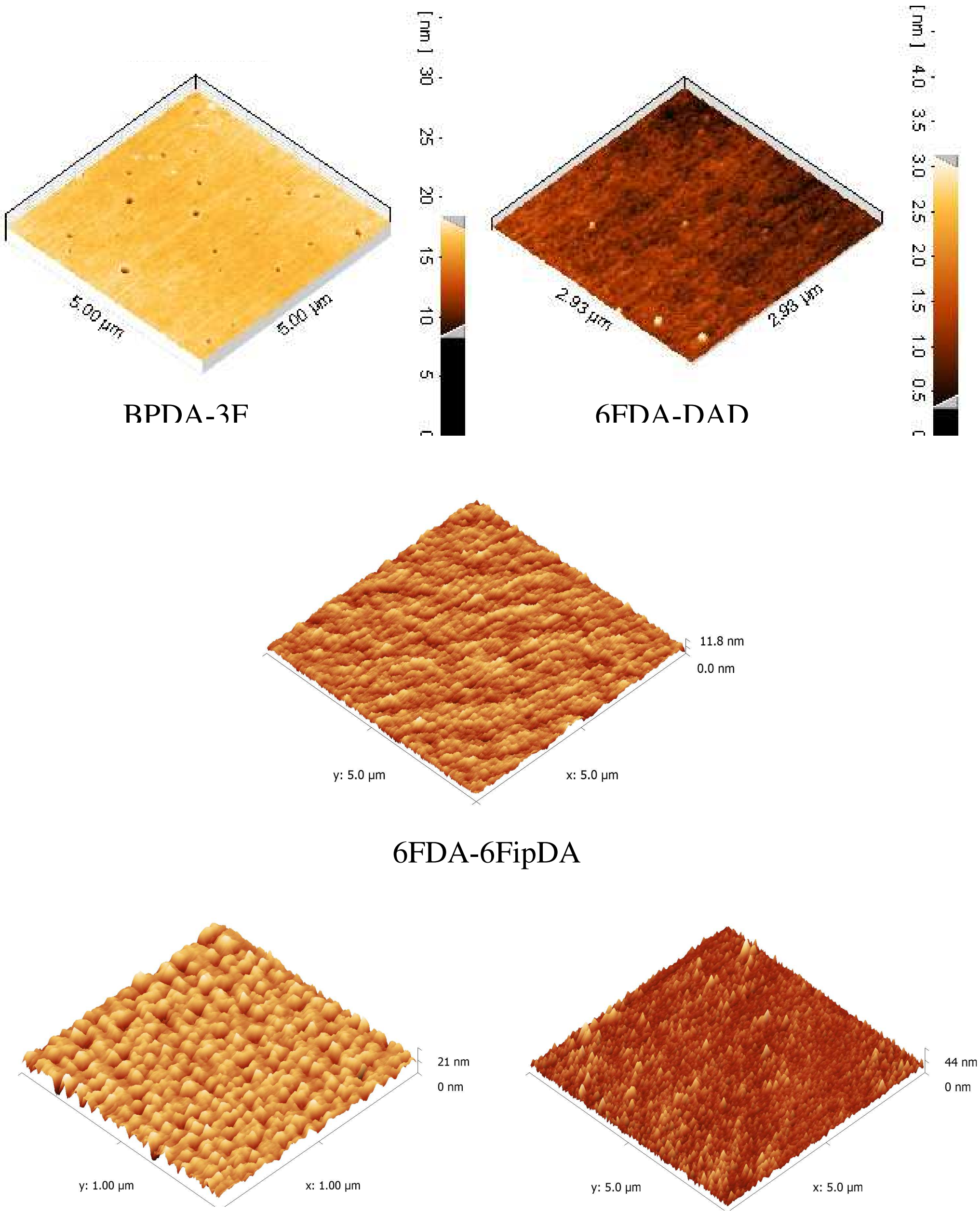

BPDA-3F

6FDA-DAD

6FDA-6FipDA

KAPTON

KAPTON TAPE

FIGURE 3.22. *SPM height data for the three synthesized polyimides, compared with height data for two commercial products. Notice the different vertical scales on the right side.*

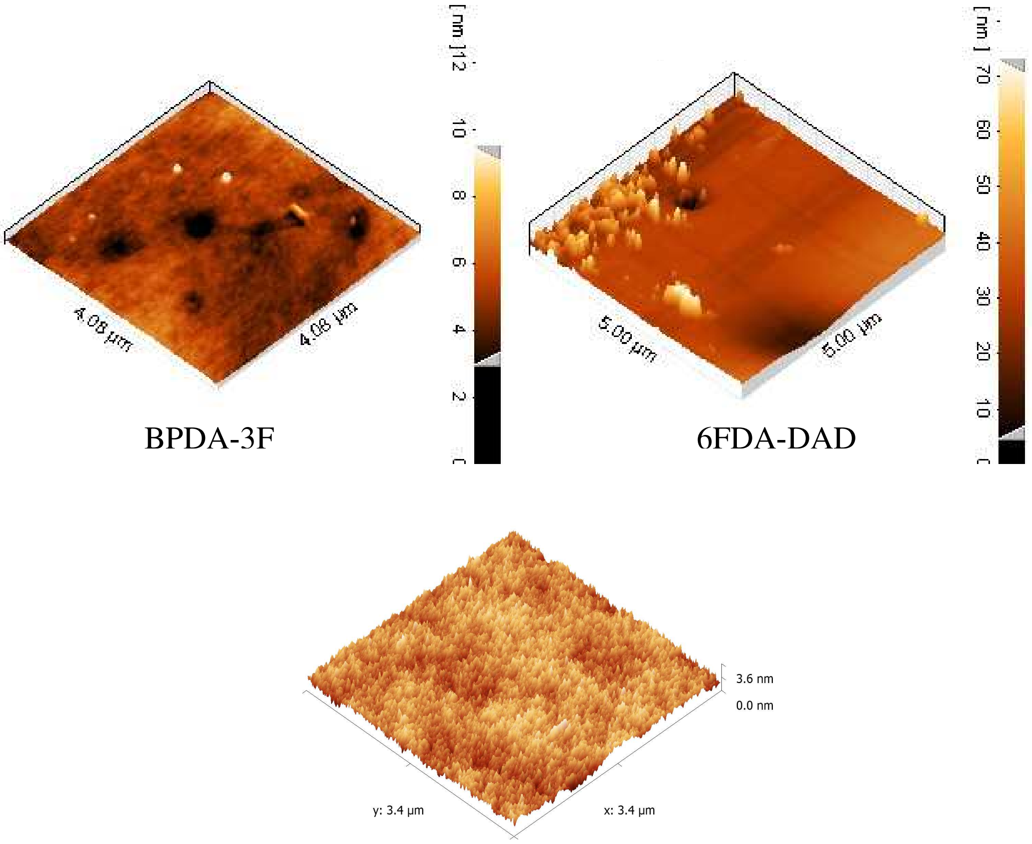

BPDA-3F

6FDA-DAD

6FDA-6FipDA

FIGURE 3.23. *SPM height data for the three synthesized polyimides after KOH 5M treatment for 10 min at 45°C. Notice the different vertical scales on the right side.*

In the case of BPDA-3F and 6FDA-DAD, SPM data were collected also after the ion exchange and the final heat curing. The partial chain mobility recovered during a thermal treatment at temperatures around the polymer T_g determines a small reduction of the average roughness, as shown in ***FIGURE 3.24***. The peculiar granular structures that are present on the 6FDA-DAD surface after the KOH treatment might be a combination of salty residues and surface damage: being the less chemical inert polyimide here considered, the complete cleavage of polymeric chains might lead locally to the formation of partially soluble species that weaken the polymer. Roughness data at the different stages of the process for the three polyimides are reported in ***TABLE 3.3***.

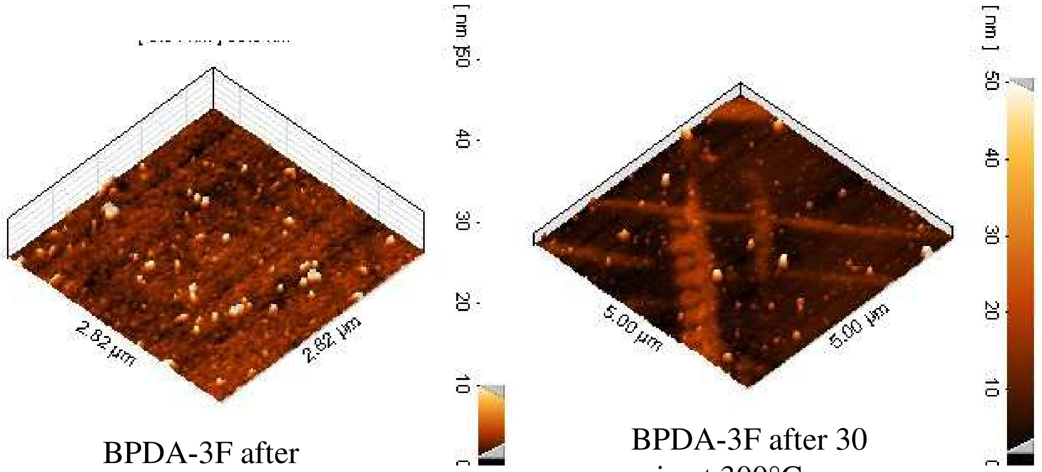

BPDA-3F after Ag$^+$ ion exchange

BPDA-3F after 30 min at 300°C

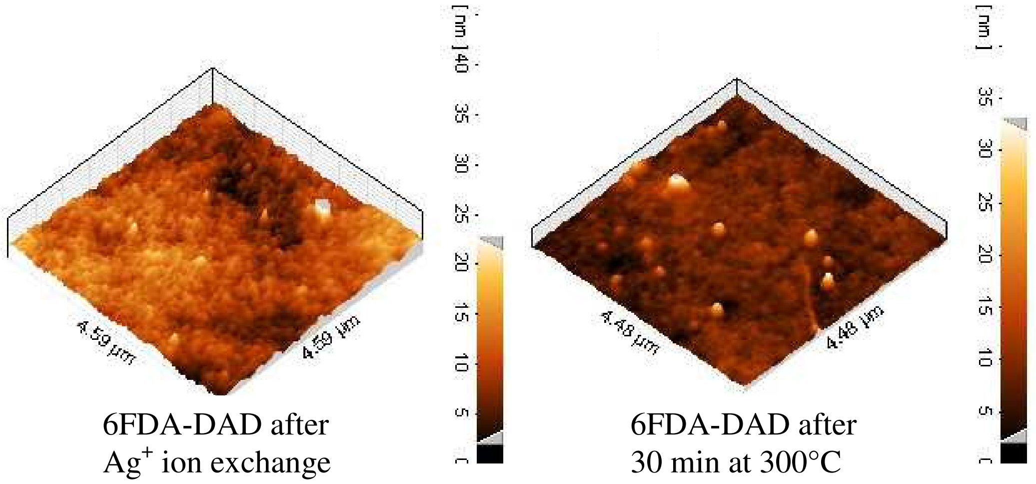

6FDA-DAD after Ag$^+$ ion exchange

6FDA-DAD after 30 min at 300°C

FIGURE 3.24. *SPM height data for BPDA-3F and 6FDA-DAD after ion exchange with Ag$^+$ and thermal treatment at 300°C for 30 min. Notice the different vertical scales on the right side.*

Polyimide	as cast	KOH 5M	Ag$^+$ exchange	30 min 300°C
6FDA-DAD	0.28	0.84	3.3	2.9
BPDA-3F	0.7	0.7	2.1	2.0
6FDA-6FipDA	1.1	0.34	-	-

TABLE 3.3. *Roughness data at the different stages of the process for the three polyimides.*

3.3.6 Metal Cluster Characterization

Absorption spectra from samples treated for 4 minutes in KOH and for 8 minutes in $AgNO_3$ solution are reported in ***FIGURE 3.25 a-c*** for annealing temperatures of 200, 300 and 350 °*C*. 6FDA-DAD treated at 200 °*C* exhibits a faint shoulder at about 420 nm, which grows up at 300 °*C* and becomes a well de.ned peak at 440 nm after annealing at 350 °*C*. On the other hand, the absorption spectrum at 200 °*C* of BPDA-3F does not exhibit any SPR feature, and at 300 °*C* a faint and broad band appears at about 440 nm, whose intensity slightly increases at 350 °*C*. The concentration of silver atoms in the samples is about the same, as revealed by RBS measurements. However, the comparison between the spectra of the two polyimides is not meaningful in this case, since the absorption peak intensity is correlated to the total amount of silver clusters present in the whole layer. Moreover, the cut-off wavelength of the polyimides, as reported in ***TABLE 3.1***, must be taken into account. In the range 420-440 nm the transmission percentage varies from 75 to 82% in the case of BPDA-3F, whereas the transmittance of 6FDA-DAD and 6FDA-6FipDA polyimides are about constant at 90% (see also ***FIGURE 3.4*** and ***TABLE 3.1***).

On the basis of the total silver ions loading reported earlier, a more significant comparison should be derived from the spectra of 6FDA-DAD treated for 4 min in KOH, 8 min in $AgNO_3$ and those of BPDA-3F treated for 6 min in KOH, 12min in $AgNO_3$. The latter ones are reported in ***FIGURE 3.25c***. After the treatment at 200 °*C* the BPDA-3F sample displays only a faint increase in the absorption baseline, but the SPR peak features are still absent. After the treatment at 300 °*C*, the same sample shows a very intense SPR peak at about 433 nm. The SPR absorption intensity is almost the same for the samples treated at 350 °*C*. Many factors contribute to the process of formation and growth of the silver clusters, so that in order to analyze the optical absorption spectra it is important to summarize the different steps which are involved during the thermal treatment in reducing atmosphere. Ikeda and co-workers[19] have already pictured the re-imidization process in the case of Cu(II) ion doping in PMDA-ODA polyimide. Metal reduction is attained by accepting electrons from molecular hydrogen, then the carboxylate anions are immediately protonated and converted in polyamic acid groups. The temperature is high enough (200 °*C*) to allow the de-hydration and condensation reaction of carboxylic groups to form imide rings. However, the stability of the metal-polyamate complex can play an important role on the overall reduction/reimidization process rate. One of the most stable forms of the silver (I) complexes is the linear one, thus it can be predicted that in the present case the carboxylate ligand has the unidentate form and it behaves as one-electron donor. In this configuration, the stability of the silver (I) complex depends on the electron-donating ability of the carboxylate oxygen atom. In the 6FDA-DAD derived polyamate, the electron withdrawing hexafluoro isopropylidene moiety is expected to lower the carboxylate donating capability, thereby producing a less stable silver (I) complex than in the case of BPDA-3F polyamate.

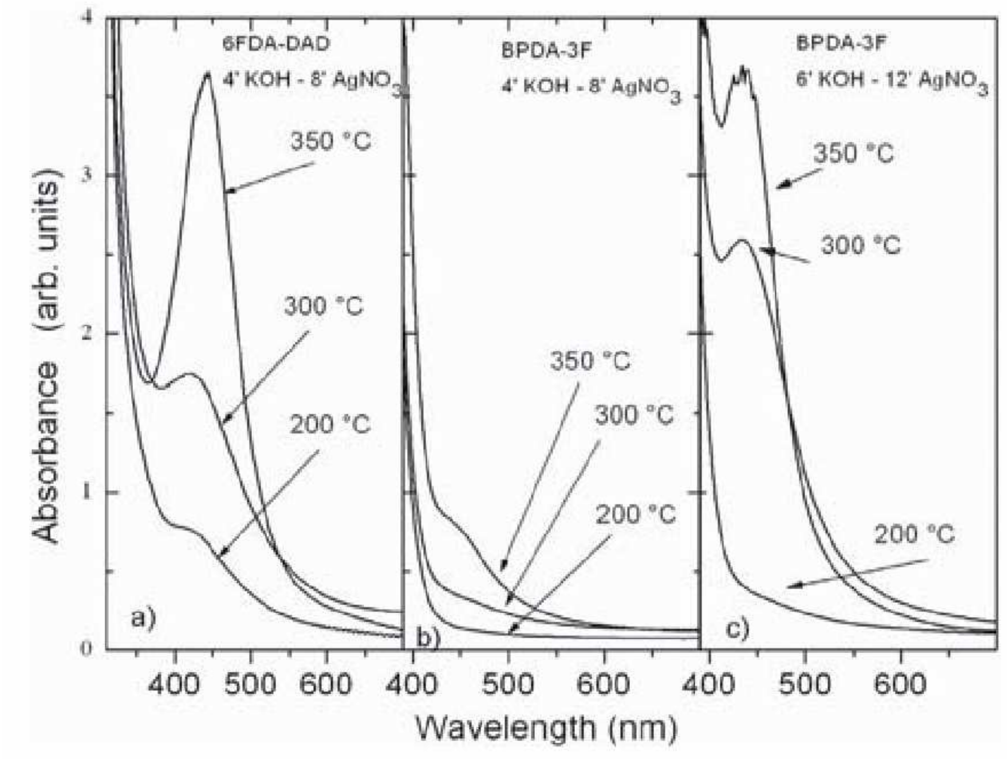

FIGURE 3.25. *Absorption spectra of the three polyimides after KOH modification and $AgNO_3$ exchange, for increasing annealing temperatures.*

On the basis of these considerations, a correlation between the SPR peak intensity and the silver (I) reduction process in the different polyimides annealed at 200 °*C* can be found.

At 200 °*C* the reduction of silver ions is not effective in the BPDA-3F sample as in 6FDA-DAD, owing to the higher silver (I) complex stability in the former system. Hence, the SPR peak features are not visible in the BPDA-3F sample. At 300 °*C* the re-imidization of both polyimides and the consequent reduction to metallic silver is complete.

The SPR peak intensity increases accordingly in both samples. The aforementioned lower transparency in the wavelength range of interest of the bare BPDA-3F polyimide accounts for the higher absorption edge observed in the spectra of the BPDA-3F derived samples. Although nanoclusters average diameter can be derived using the full width half maximum (FWHM) of the SPR peak, according to the literature[28], the contribution of the background arising from the polyimide matrix can not be easily removed without introducing some artefacts, such as modification of peak position and peak shape, thus leading to misinterpretation of data. Therefore, the information on the nanocrystals size and size distribution must be inferred from X-ray diffraction and TEM analyses.

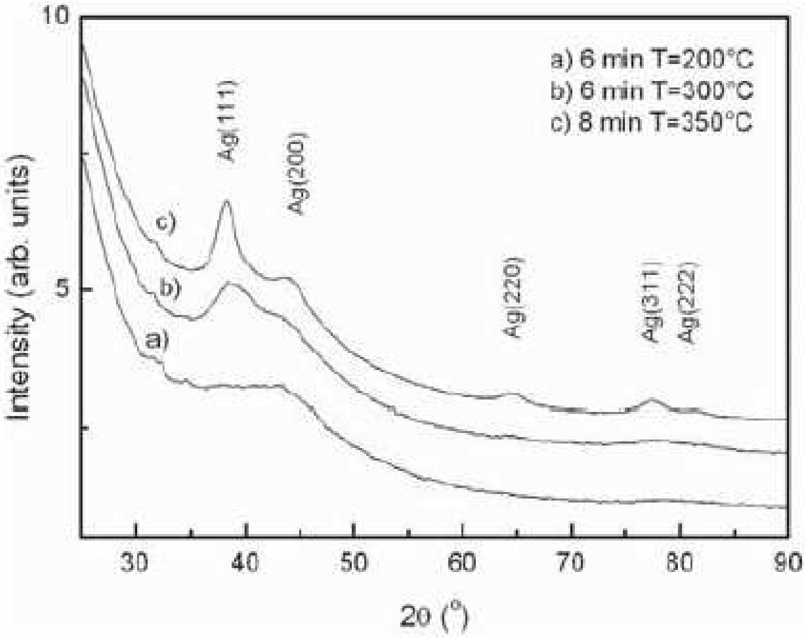

FIGURE 3.26. *XRD spectra of BPDA-3F treated for 6 min in KOH, 12 min in $AgNO_3$ and annealed at 200 °C and 300 °C in reducing atmosphere. The spectrum of the sample treated for 8 min in KOH, 16 min in $AgNO_3$ and annealed at 350°C is also reported.*

The clusters crystal structure was investigated by X-ray diffraction and the results for samples of BPDA-3F treated for 6 min in KOH, 12 min in $AgNO_3$ and annealed at 200 and 300 °*C* are presented in ***FIGURE 3.26*** (curves a and b). The spectrum of the sample treated for 8 min in KOH, 16 min in AgNO3 and annealed at 350 °*C* is also reported (curve c).

At 300 °*C* the two main peaks of fcc silver can be observed, thereby proving that in this temperature regime precipitation of metallic silver already occurred. In the spectrum of the sample annealed at 350 °*C* the peaks are well defined and the intensity grows up as a result of complete silver reduction and crystal growth. In order to compare the silver crystals growth in the two polyimides, the XRD spectra of 6FDA-DAD and BPDA-3F treated for the same time in KOH and $AgNO_3$ and annealed at 300 °*C* have been collected and are reported in ***FIGURE 3.27***.

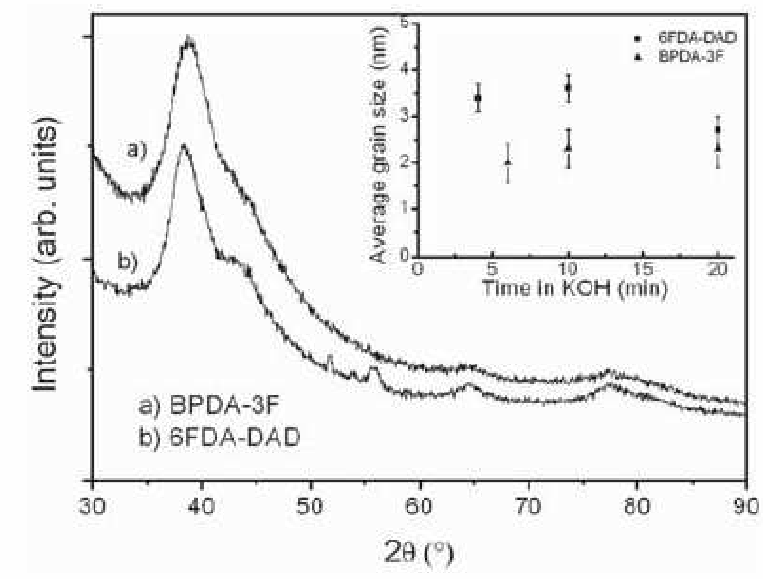

FIGURE 3.27. *XRD spectra of 6FDA-DAD and BPDA-3F treated for 20 min in KOH, 40 min in* $AgNO_3$ *and annealed at 300 °C in reducing atmosphere. In the inset, the average grain size of silver crystals as derived from the Scherrer's formula is reported for both modified polyimides annealed at 300 °C as a function of the treatment time in KOH.*

Using the well-known Scherrer's formula, the average crystallites size has been calculated by the full width half maximum (FWHM) of the Ag (111) diffraction peak, for both 6FDA-DAD and BPDA-3F treated for different times and annealed at 300 *°C*. The results are reported in the inset of ***FIGURE 3.27*** and they evidence that almost comparable clusters dimensions have been obtained in both polyimides. The clusters size ranges from 2 up to 3.5 nm and it is negligibly affected by the treatment time in KOH.

More information were collected by measuring the XRD data of 6FDA-6FipDA treated for 40 min in KOH, 40 min in $AgNO_3$ and annealed at 300 °C in air. The heavy loading resulted in larger crystallites (~6 nm), as shown in ***FIGURE 3.28***.

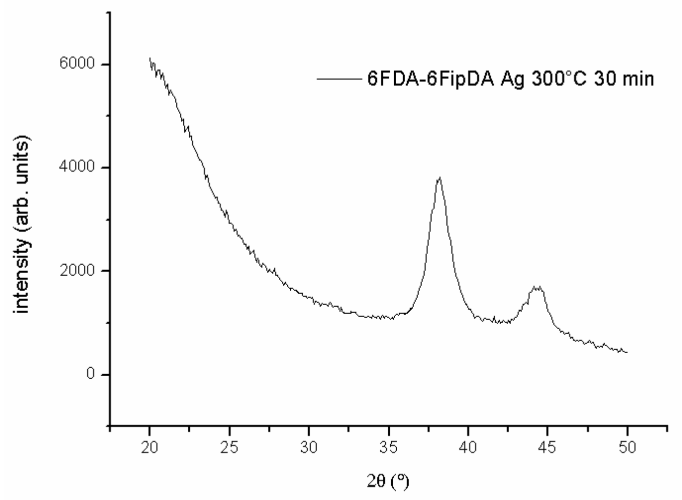

FIGURE 3.28. *XRD spectra of 6FDA-6FipDA treated for 40 min in KOH, 40 min in* $AgNO_3$ *and annealed at 300 °C in air. The average grain size of silver crystals as derived from the Scherrer's formula is 6 nm.*

. Further investigations on the nanocomposite structure were performed with TEM. Analyses on the sample 6FDA-DAD treated for 10 min in KOH, 20 min in $AgNO_3$ and annealed at 300 *°C* in reducing atmosphere confirmed the experimental RBS results as regarding the penetration depth of Ag (estimated in 1.6 μm for this sample), as clearly observed in the micrograph reported in ***FIGURE 3.29***, and the homogeneity of the silver clusters distribution, as evidenced in the micrographs of ***FIGURE 3.30***.

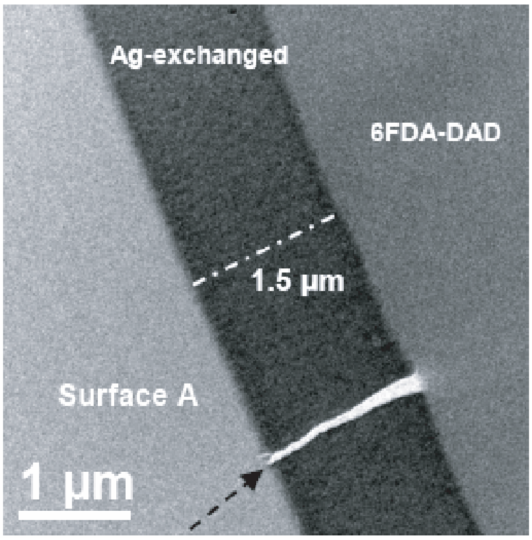

FIGURE 3.29. *Cross-sectional TEM image of 6FDA-DAD treated for 10 min in KOH, exchanged with AgNO$_3$ and annealed at 300°C for 30 min in a reducing atmosphere, highlighting the thickness of the modified layer. The arrow indicates a crack in the modified layer.*

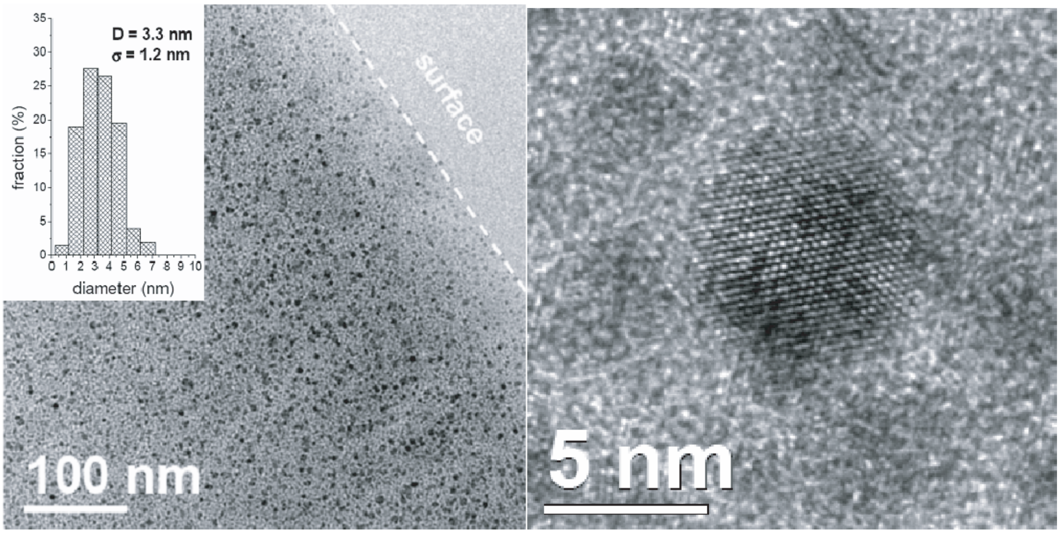

FIGURE 3.30. *Cross-sectional TEM images at different magnifications of 6FDA-DAD treated for 10 min KOH, for 20 min in AgNO$_3$ solution and annealed at 300°C in reducing atmosphere. The size histogram is reported in the inset of the left image.*

The TEM analyses performed on gold tetrachloroaurate impregnated samples show a uniform cluster distribution across the layer. The size distribution histogram as well shows a relatively good monodispersity, with an average cluster diameter D = 3.9 ± 1.2 nm (***FIGURE 3.31)***. The cluster shapes are consistently spherical and monocrystalline, as evidenced by the high-resolution TEM image reported in ***FIGURE 3.32***.

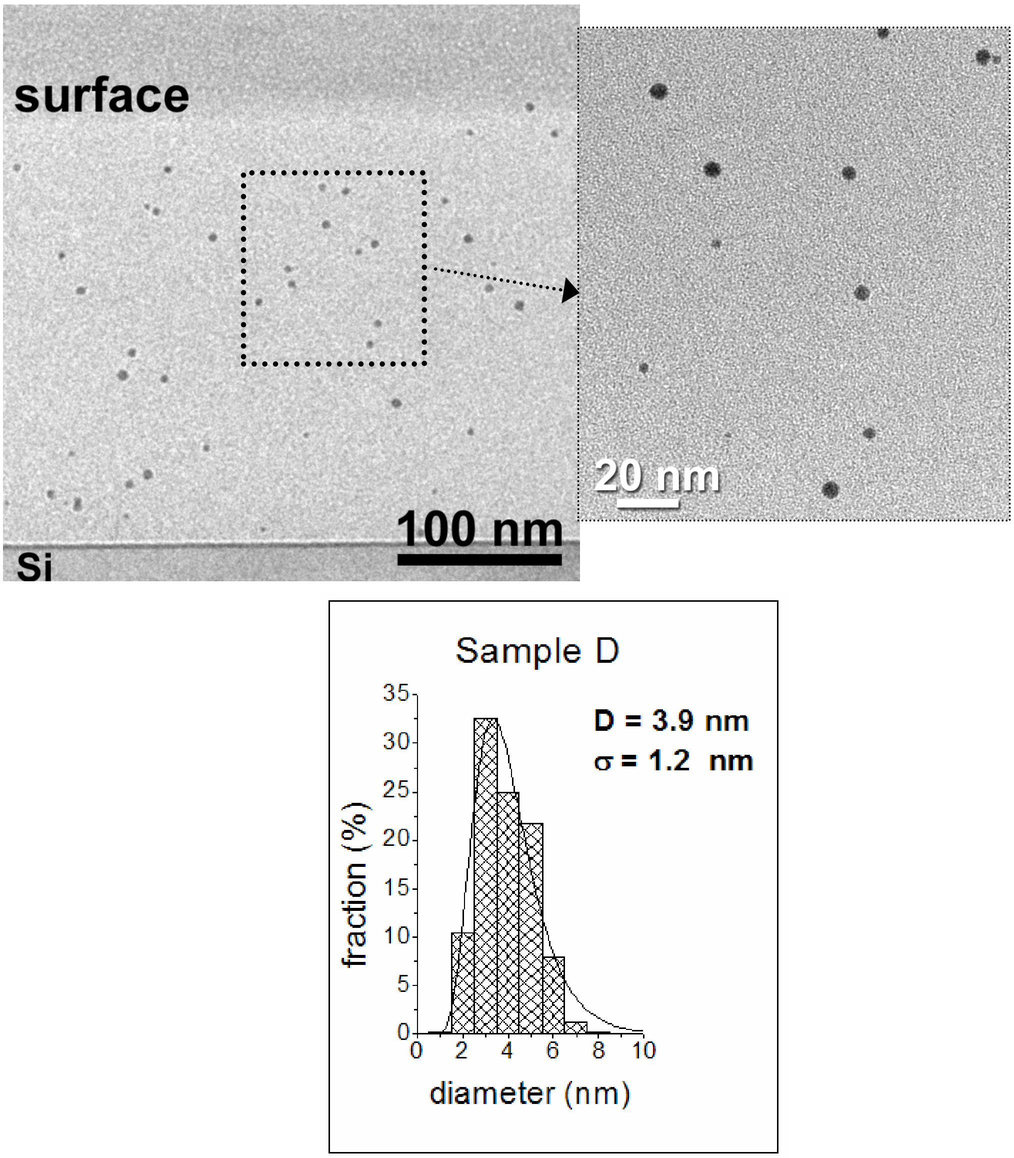

FIGURE 3.31. *Cross-sectional TEM images at different magnifications of BPDA-3F polyamic acid treated with* $HAuCl_4$ *solution and annealed at 300°C in air (top) and size distribution histogram (bottom) of the resulting gold clusters .*

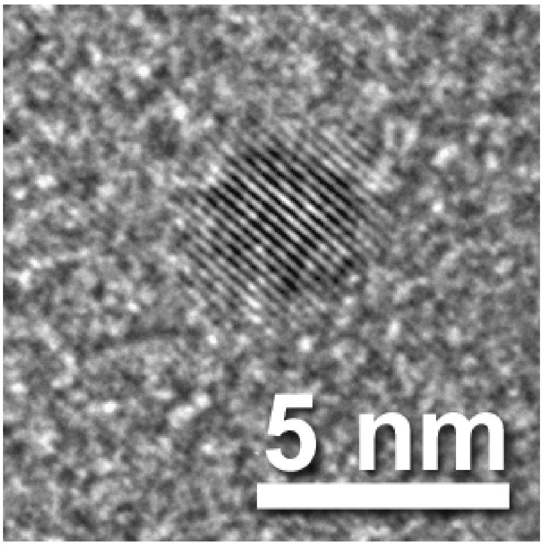

FIGURE 3.32. *High-resolution TEM image of BPDA-3F polyamic acid treated with* $HAuCl_4$ *solution and annealed at 300°C in air.*

3.4 Conclusions

The formation of gold and silver nanoparticles in transparent fluorinated polyimides has been studied using different microanalytical, microstructural and optical techniques.

For silver, the first stage of the process, leading to the formation of the potassium polyamate salt, and the following K^+-Ag^+ ion-exchange process have been correlated to the starting polyimide chemical structure. RBS analysis evidenced that the K penetration depth is a linear function of the treatment time in KOH, thereby proving that the chemical reaction between the nucleophile and the polyimide is in both cases a first order process. Moreover, the K penetration rate depends on the polyimide structure: both the chemical nature of the substituents along the polymeric chain and the network permeability to aqueous solution are considered to affect the K penetration rate. XRD measurements have been used to estimate the intersegmental distance (*d*-spacing) in both the original polyimides and the results evidenced a loosened chain packing in 6FDA-DAD with respect to BPDA-3F and 6FDA-6FipDA, thus proving that a faster permeation of the KOH solution through the 6FDA-DAD matrix can effectively occur. The ion-exchange step in $AgNO_3$ solutions affords complete substitution of K by Ag ions in the three polyimides, within the treatment times used in these experiments.

In another set of experiments, polyamic acid was used instead of the corresponding polyimides, allowing to skip the K+ modification step. This approach resulted in complementary Ag doping profiles, as the Ag ion concentration at a given depth grows with time.

The Ag nanocrystals precipitation in reducing atmosphere has been correlated to the silver reduction process, which in turns is related to the silver (I) polyamate complex stability in the two different polyimides. The subsequent step of clusters growth as a function of the annealing temperature has been investigated by XRD and TEM analyses. Similar clusters dimensions have been estimated in the different polyimides, ranging from 2 to 3.5 nm. For gold, the chloroaurate complex impregnation process has been monitored with the same techniques. As the diffusing species is bulkier, an initial saturation of the first layers of polymer has to be overcome before the diffusion becomes effective in the bulk. Gold nanoclusters were obtained thorugh the annealing of the doped films in air, with the concurrent formation of the imidic structures.

The effective application of such nanocomposites for optical gas sensors is currently under investigation.

3.5 References

1. F. Gonella, P. Mazzoldi, in *Handbook of Nanostructured Materials and Nanotechnology*, edited by H. Nalwa (Academic, San Diego, **2000**), Vol. 4, 2
2. A.N. Shipway, *Chem. Phys. Chem.* 1, 18 (**2000**).
3. U. Kreibig, M. Vollmer, *Optical Properties of Metal Clusters* (Springer, Berlin, **1995**).
4. P. Mulvaney, *Langmuir* 12, 788 (**1996**).
5. G. Chumanov, K. Sokolov, B.W. Gregory, T.M. Cotton, *J. Phys. Chem.* 99, 9466 (**1995**).
6. J. Matsui, K. Akamatsu, S. Nishiguchi, D. Miyoshi, H.Nawafune, K. Tamaki, N. Sugimoto, *Anal. Chem.* 76, 1310 (**2004**).
7. C. de Julian Fernandez, M.G. Manera, J. Spadavecchia, G. Maggioni, A. Quaranta, G. Mattei, M. Bazzan, E. Cattaruzza, M. Bona.ni, E. Negro, A. Vomiero, S. Carturan, C. Scian, G. Della Mea, R. Rella, L. Vasanelli, P. Mazzoldi, *Sens. Actuators B* 111-112, 225 (**2005**).
8. Y. Dirix, C. Bastiaansen, W. Caseri, P. Smith, *J. Mater. Sci.* 34, 3859 (**1999**).
9. H. Biederman, *Vacuum* 37, 367 (**1987**).
10. K. Akamatsu, T. Kawamura, H. Nabika, S. Deki, T. Strunskus, F. Faupel, *J. Mater. Chem.* 12, 3610 (**2002**).
11. R.J. Angelo, U.S. Patent 3,073,785 (**1959**).
12. M.W. Wllison, L.T. Taylor, *Chem. Mater.* 6, 990 (**1994**).
13. R.E. Southward, D.W. Thompson, *Chem. Mater.* 16, 1277 (**2004**).
14. S. Yoda, A. Hasegawa, H. Suda, Y. Uchimaru, K. Haraya, T. Tsuji, K. Otake, *Chem. Mater.* 16, 2363 (**2004**).
15. A.L. Stepanov, *Tech. Phys.* 49, 143 (**2004**).
16. G. Maggioni, A. Vomiero, S. Carturan, C. Scian, G.Mattei, M. Bazzan, C. de Julian Fernandez, P. Mazzoldi, A. Quaranta, G. Della Mea, *Appl. Phys. Lett.* 85, 5712 (**2004**).
17. K. Akamatsu, S. Ikeda, H. Nawafune, S. Deki, *Chem. Mater.* 15, 2488 (**2003**).
18. K. Akamatsu, *Eur. Phys. J. D* 24, 377 (**2003**).

19. S. Ikeda, K. Akamatsu, H. Nawafune, T. Nishino, S. Deki, *J. Phys. Chem. B* 108, 15599 (**2004**).
20. Y. Li, Q. Lu, X. Qian, Z. Zhu, J. Yin, *Appl. Surf. Sci*. 233, 299 (**2004**).
21. S. Sasaki, S. Nishi, in *Polyimides: fundamentals and applications*, edited by Ghosh, Mittal (Marcel Dekker Inc., New York, **1996**), p. 71.
22. W.B. Alston, R.F. Gratz, US Patent 4,885,116 (**1989**).
23. L.R. Doolittle, *Nucl. Instrum. Meth. B* 9, 334 (**1985**).
24. R.M. Silverstein, G.C. Bassler, T.C. Morrill, in *Spectrometric Indentification of Organic Compounds* (J. Wiley & Sons, New York, **1981**), p. 116.
25. A.Y. Alentiev, K.A. Loza, Y.P. Yampolskii*, J. Membr. Sci*. 167, 91 (**2000**).
26. T.H. Kim, W.J. Koros, G.R. Husk, K.C. O’Brien, *J. Membr. Sci*. 37, 45 (**1988**).
27. S. Ivanova, C. Petit, V. Pitchon submitted to *J. Catal*. (**2003**).
28. G.W. Arnold, *J. Appl. Phys.* 46, 4466 (**1975**).

Chapter 4

Preparation and Modification of DNA Origami with Gold Nanoparticles

4.1 Introduction

In 1959, Richard Feynman put forward the challenge of writing the Encyclopaedia Britannica on the head of a pin[1], a task which he calculated would require the use of dots 8 nm in size. Scanning probe techniques have essentially answered this challenge: atomic force microscopy[2] (AFM) and scanning tunnelling microscopy[3,4] (STM) allow us to manipulate individual atoms. But these techniques create patterns serially (one line or one pixel at a time) and tend to require ultrahigh vacuum or cryogenic temperatures. As a result, methods based on self-assembly are considered as promising alternatives that offer inexpensive, parallel synthesis of nanostructures under mild conditions[5]. Indeed, the power of these methods has been demonstrated in systems based on components ranging from porphyrins[6] to whole viral particles[7]. However, the ability of such systems to yield structures of high complexity remains to be demonstrated. In particular, the difficulty of engineering diverse yet specific binding interactions means that most self-assembled structures contain just a few unique positions that may be addressed as ‘pixels’. Nucleic acids can help overcome this problem: the exquisite specificity of Watson–Crick base pairing allows a combinatorially large set of nucleotide sequences to be used when designing binding interactions. The field of ‘DNA nanotechnology’[8,9] has exploited this property to create a number of more complex nanostructures, including two-dimensional arrays with 8–16 unique positions and less than 20nm spacing[10,11], as well as three-dimensional shapes such as a cube[12] and truncated octahedron[13]. However, because the synthesis of such nanostructures involves interactions between a large number of short oligonucleotides, the yield of complete structures is highly sensitive to stoichiometry (the relative ratios of strands). The synthesis of relatively complex structures was thus thought to require multiple reaction steps and purifications, with the ultimate complexity of DNA nanostructures limited by necessarily low yields. Recently, the controlled folding of a long single DNA strand into an octahedron was reported[14], an approach that may be thought of as 'single-stranded DNA origami'. The success of this work suggested that the folding of long strands could, in principle, proceed without many misfoldings and avoid the problems of stoichiometry and purification associated with methods that use many short DNA strands.

Paul Rothemund presented a versatile and simple 'one-pot' method for using numerous short single strands of DNA to direct the folding of a long, single strand of DNA into desired shapes that are roughly 100nm in diameter and have a spatial resolution of about 6 nm[15]. The generality of his method, which was termed 'scaffolded DNA origami', was demonstrated by assembling several different shapes, such as squares, triangles and fivepointed stars: the method not only provides access to structures that approximate the outline of any desired shape, but also enables the creation of structures with arbitrarily shaped holes or surface patterns composed of more than 200 individual pixels. The patterns on the 100-nm-sized DNA shapes thus have a complexity that is tenfold higher than that of any previously self-assembled arbitrary pattern and comparable to that achieved using AFM and STM surface manipulation4.

More precisely, an origami consists in a long single strand, typically DNA coming from the bacteriophage virus M13mp18 (7249 bases), mixed with a set of oligonucleotides where half of their sequence is complementary to a well defined sequence localized on the main long strand, and the other half is complementary to another sequence localized on a different site of the main long strand. In this way the oligonucleotide acts as a crossover bridge between non-consecutive locations of the main strand, folding it (this is the origin of the name *origami*) in position pre-determined by the synthetic sequence of the oligonucleotide. A given set of oligonucleotides will then force tha main strand to fold on itself and in general to form structures with arbitrary shape, which is univocally bound to the chosen oligonucleotide mix (***FIGURE 4.1-4.5***).

This approach comes with numerous problems: even in the simple case of planar shapes, mechanical stresses arise from the secondary structure of the double helix, whose step is well defined; oligonucleotides are required to have a minimal length such to grant the non-redundancy and the univocity of the target sequences on the main strand; the oligonucleotide set has to grant the stability of the final structure. Software codes have therefore been developed to address and solve these issues accounting for the physical constraints imposed by DNA's nature itself.

4.2 Design of Scaffolded DNA Origami

The design of a DNA origami is performed in five steps, the first two by hand and the last three aided by computer.

4.2.1 First Step

The first step is to build a geometric model of a DNA structure that will approximate the desired shape. ***FIGURE 4.1*** shows an example shape (outlined in red) that is 33 nm wide and 35 nm tall. The shape is filled from top to bottom by an even number of parallel double helices, idealized as cylinders. Each cylinder represents in length the minimal unit of bases required to have a single turn, therefore constraining the shape to be an integer number of turns in length.

To hold the helices together, a periodic array of crossovers (indicated in ***FIGURE 4.1*** as small blue crosses) is incorporated; these crossovers designate positions at which strands running along one helix switch to an adjacent helix and continue there. Crossovers can in principle be placed where the helices in parallel strands are facing each other, i.e. at the middle or at the end of a cylinder.

The resulting model approximates the shape within one turn (3.6 nm) in the x-direction and roughly two helical widths (4 nm) in the y-direction. As noticed before in DNA lattices[16], parallel helices in such structures are not close-packed, perhaps owing to electrostatic repulsion. Thus the exact y-resolution depends on the gap between helices. The gap, in turn, appears to depend on the spacing of crossovers. In ***FIGURE 4.1*** crossovers occur every 1.5 turns along alternating sides of a helix, but any odd number of half-turns may be used. In the studied origamis, data are consistent with an inter-helix gap of 1 nm for 1.5-turn spacing and 1.5 nm for 2.5-turn spacing, yielding a y-resolution of 6 or 7 nm, respectively.

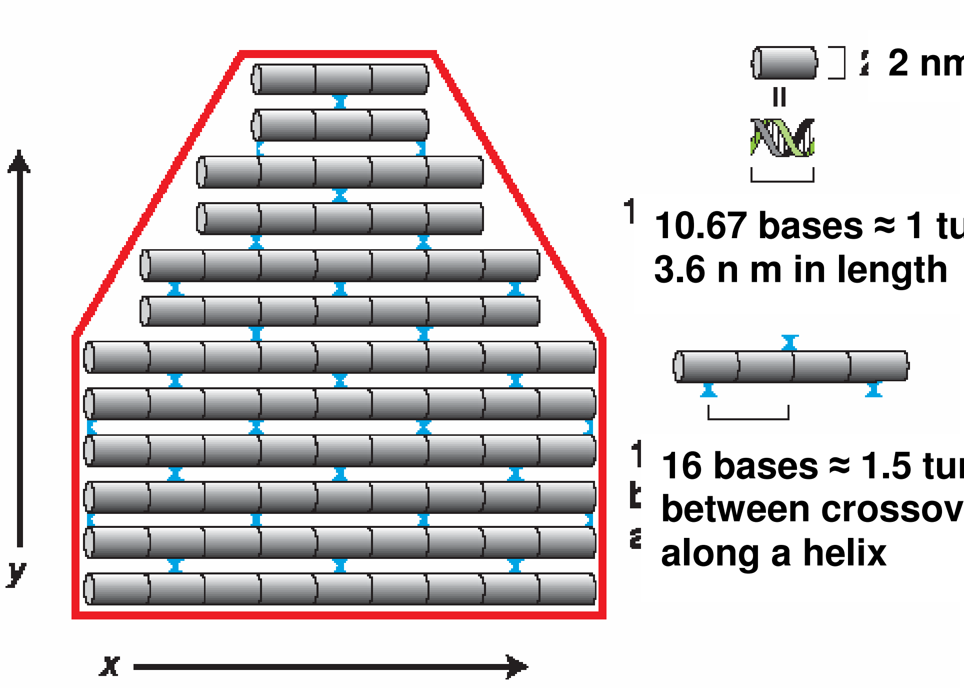

FIGURE 4.1*. First step: a shape (red) is approximated by parallel double helices joined by periodic crossovers (blue).*

4.2.2 Second Step

Conceptually, the second step (illustrated in ***FIGURE 4.2***) proceeds by folding a single long scaffold strand (900 nucleotides (nt) in ***FIGURE 4.2***) back and forth in a raster fill pattern so that it comprises one of the two strands in every helix; progression of the scaffold from one helix to another creates an additional set of crossovers, the ‘scaffold crossovers’ (indicated by small red crosses in ***FIGURE 4.2***). The fundamental constraint on a folding path is that the scaffold can form a crossover only at those locations where the DNA twist places it at a tangent point between helices. Thus for the scaffold to raster progressively from one helix to another and onto a third, the distance between successive scaffold crossovers must be an odd number of half turns. Conversely, where the raster reverses direction vertically and returns to a previously visited helix, the distance between scaffold crossovers must be an even number of half-turns. Note that the folding path shown in ***FIGURE 4.2*** is compatible with a circular scaffold and leaves a ‘seam’ (a contour which the path does not cross).

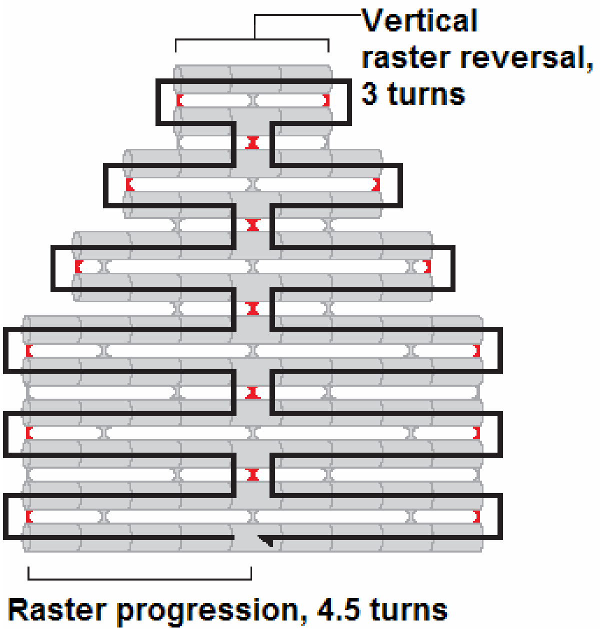

FIGURE 4.2. *Second step: a scaffold (black) runs through every helix and forms more crossovers (red).*

4.2.3 Third Step

Once the geometric model and a folding path are designed, they are represented as lists of DNA lengths and offsets in units of half-turns. These lists, along with the DNA sequence of the actual scaffold to be used, are input to a computer program. Rather than assuming 10.5 base pairs (bp) per turn (which corresponds to standard B-DNA twist), the program uses an integer number of bases between periodic crossovers (for example, 16 bp for 1.5 turns). It then performs the third step, the design of a set of 'staple strands' (the coloured DNA strands in ***FIGURE 4.3***) that provide Watson–Crick complements for the scaffold and create the periodic crossovers. Staples reverse direction at these crossovers; thus crossovers are antiparallel, a stable configuration well characterized in DNA nanostructures. Note that the crossovers in ***FIGURE 4.3*** are drawn somewhat misleadingly, in that single-stranded regions appear to span the inter-helix gap even though the design leaves no bases unpaired. In the assembled structures, helices are likely to bend gently to meet at crossovers so that only a single phosphate from each backbone occurs in the gap. Such small-angle bending is not expected to greatly affect the width of DNA origami.

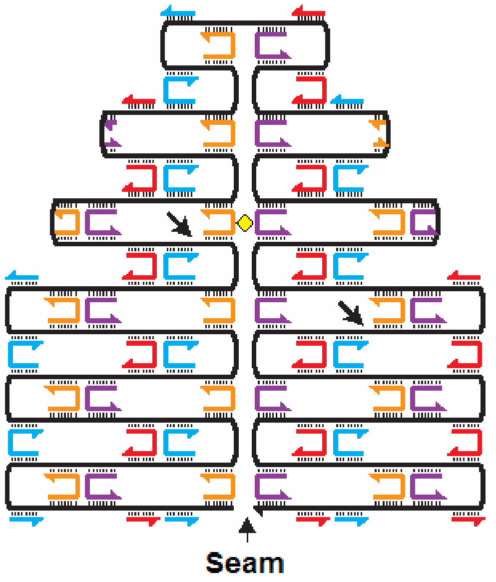

FIGURE 4.3*. Third step: as first designed, 'staples' are 16mers and bind only two helices. Thw yellow diamond indicates a position at which a staple can be cut and resealed to bridge the seam.*

4.2.4 Fourth Step

The minimization and balancing of twist strain between crossovers is complicated by the non-integer number of base pairs per half-turn (5.25 in standard B-DNA) and the asymmetric nature of the helix (it has major and minor grooves). Therefore, to balance the strain[16] caused by representing 1.5 turns with 16 bp, periodic crossovers are arranged with a glide symmetry, namely that the minor groove faces alternating directions in alternating columns of periodic crossovers (see ***FIGURE 4.4***, especially cross-sections 1 and 2). Scaffold crossovers are not balanced in this way. Thus in the fourth step, the twist of scaffold crossovers is calculated and their position is changed (typically by a single bp) to minimize strain; staple sequences are recomputed accordingly. Along seams and some edges the minor groove angle (150°) places scaffold crossovers in tension with adjacent periodic crossovers (***FIGURE 4.4***, cross-section 2); such situations are left unchanged. Wherever two staples meet there is a nick in the backbone. Nicks occur on the top and bottom faces of the helices.

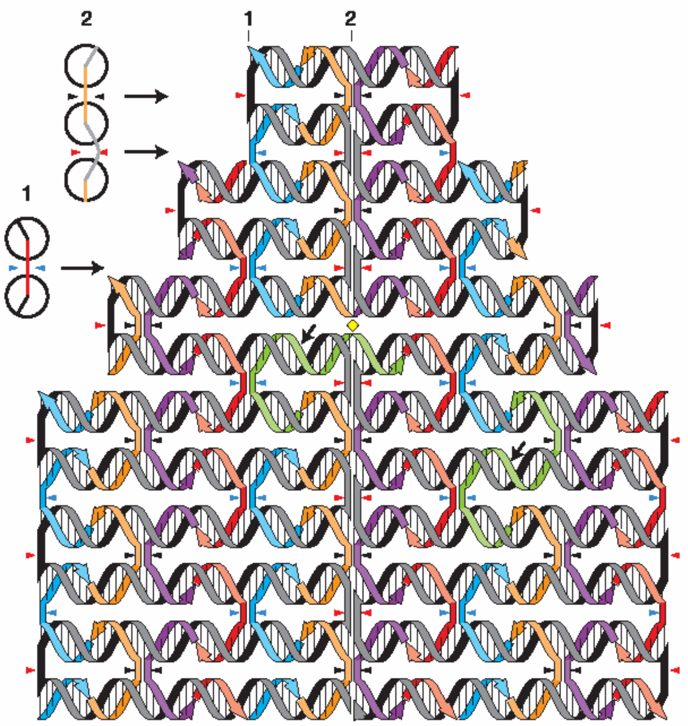

FIGURE 4.4. *Fourth step: here strands are drawn as helices. Red triangles point to scaffold crossovers, black triangles to periodic crossovers with minor grooves on the top face of the shape, blue triangles to periodic crossovers with minor grooves on bottom. Cross-sections of crossovers (1, 2, viewed from left) indicate backbone positions with coloured lines, and minor/major grooves with small/large angles between them. The black arrows denote nicks that have been sealed with respect to* ***FIGURE 4.3***.

4.2.5 Fifth Step

In the final step, to give the staples larger binding domains with the scaffold (in order to achieve higher binding specificity and higher binding energy which results in higher melting temperatures), pairs of adjacent staples are merged across nicks to yield fewer, longer, staples (***FIGURE 4.5***). To strengthen a seam, an additional pattern of breaks and merges may be imposed to yield staples that cross the seam; a seam spanned by staples is termed 'bridged'. The pattern of merges is not unique; different choices yield different final patterns of nicks and staples. All merge patterns create the same shape but the merge pattern dictates the type of grid underlying any pixel pattern later applied to the shape.

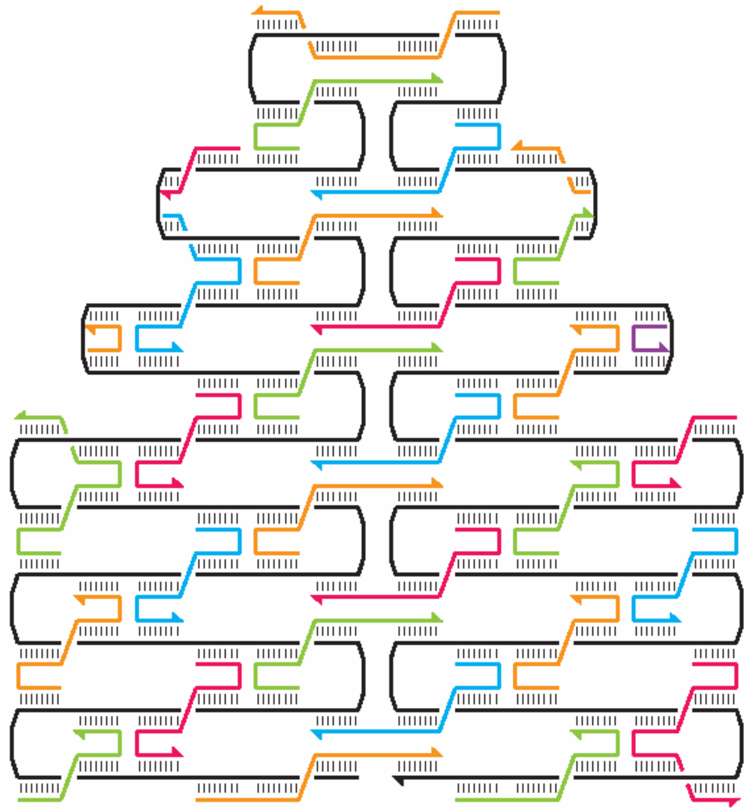

FIGURE 4.5*. Fifth and final step: a finished designed after merges and rearrangements along the seam, that is now bridged at multiple locations. Most staples are 32mers spanning three helices. The scaffold raster allows the use of circular ssDNA species.*

4.3 Folding M13mp18 genomic DNA into shapes

Circular genomic DNA from the virus M13mp18 was chosen as the scaffold. Its naturally single-stranded 7,249-nt sequence was examined for secondary structure, and a hairpin with a 20-bp stem was found. Whether staples could bind at this hairpin was unknown, so a 73-nt region containing it was avoided. In principle, any bidimensional structure can be obtained with the proper design strategies: in fact, origami varying from simple geometric shapes (rectangles, discs, triangles) to more complex shapes (“smileys”, stars) to supramolecular assemblies (considering each structure as a single macromolecule, ***FIGURE 4.6***).

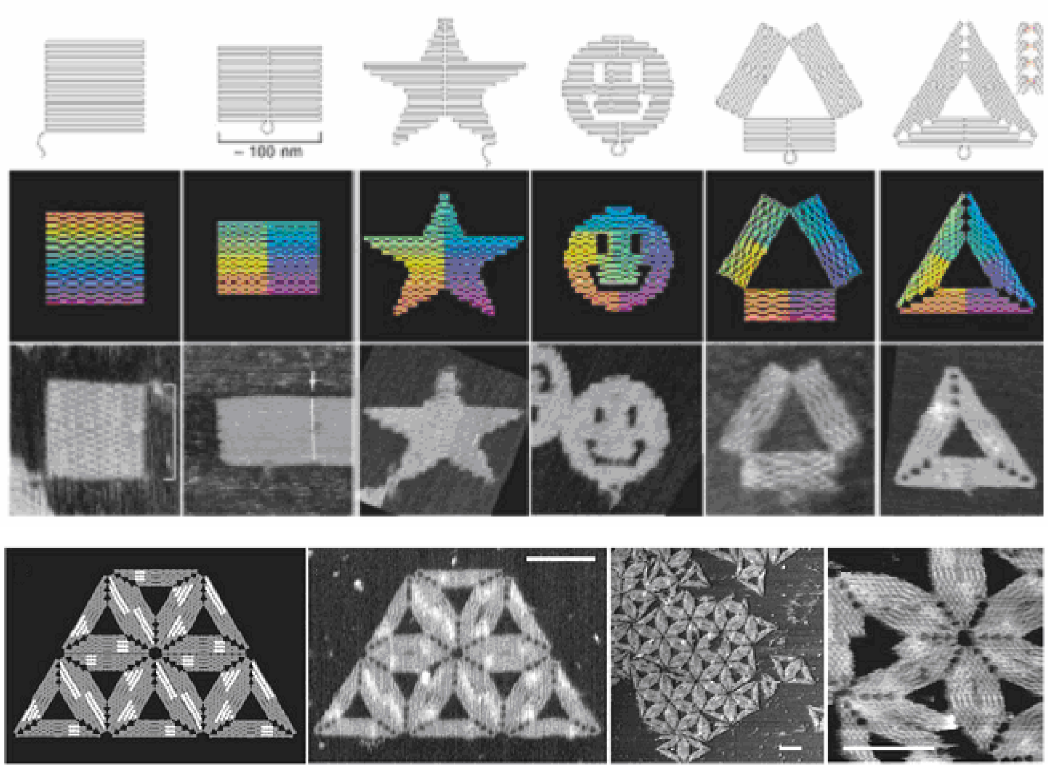

FIGURE 4.6. *Examples of the variety of structures that can be obtained with the DNA origami technique. All the images in the third row (single image size 165x165 nm^2) and fourth row (scale bar 100 nm) have been obtained with a Nanoscope III Multimode (DI, now Veeco), in tapping mode (SiN, 8÷12 kHz) with an open liquid cell.*

Two main types of structures that are compatible with the use of a circular ssDNA were chosen: the so-called “tall” rectangle (***FIGURE 4.7***) and the triangle with trapezoidal domains (***FIGURE 4.8***). The “tall “ rectangle was chosen as its structure carries a central seam that, giving the structure a higher stiffnes, makes it less subject to deformation. Similarily, in the chosen triangles the slanted edges of the trapezoids meet at the vertices allowing for the addition of bridging staples along these interfaces, providing an overall extremely robust structure (***FIGURE 4.9***).

The strand mixes that define the final structure come from the supplier (Integrated DNA Technologies) in a poorly quantitated effective concentration, the nominal being 100 or 150 μM. Therefore, a safe, experimental excess to observe the formation of the origami is considered to be 10x with respect to the main scaffold concentration. The stock solution of M13mp18 has a .01 nM concentration (Bayou Biolabs), and the usual procedure consists in mixing 5μL of M13mp18, 5 μL of the “strand mix” stock and 5 μL of 10x Tris-acetate-EDTA (TAE) Mg^{++} buffer solution, followed by dilution with 35 μL of water, that brings the final concentration of structures in solution to .001 nM. The mixture is then annealed at 90°C and cooled down to RT a 1°C/min with a PCR machine.

To image the DNA structures with a liquid cell AFM, 2 ÷ 5 μL of the origami solution are pipetted directly on a ~1 cm^2 substrate, and then diluted to 50÷100 μL with buffer so as to fill the cell. Si_3N_4 triangular tips with a resonating frequency of 8 ÷ 12 kHz from several suppliers were used, and the relative imaging parameters are not reported here as they vary significatively for tips from batch to batch.

When samples were deposited on freshly cleaved mica, only folded DNA structures stuck to the surface while excess staples remained in solution. Of the products imaged by AFM, a particular structure was considered qualitatively ‘well-formed’ if it had no defect (hole or indentation in the expected outline) greater than 15 nm in diameter. If the origami are required in air, the solution can be gently blown off with a nitrogen flow, the adhesion being so effective that this process can be cycled multiple times.

Many other substrates have been tested, including surface-functionalized silicon and silica and polymers. Silicon and silica were funcionalized after cleaning with diluted piranha solutions (1:1:5 H_2SO_4:H_2O_2:H_2O) with aminopropyl-trimethoxysilane via vapor-phase in a custom-built cell. Polystyrene (M_w 100000) was spin casted from a 1 % wt toluene solution at 3000 rpm and UV-ozone treated for 10 min. BPDA-ODA and 6FDA-6FipDA were spin casted from 5% wt solutions in NMP in a nitrogen atmosphere, heated on a hot plate at 200°C for 60 min and surface modified by contacting the film top layer with a 5M NaOH solution for 10 min. After a thoroughful rinsing with millipore water, the surface ions have been exchanged with a 50 mM $MgAc_2$ solution for 20 min, and rinsed again.

Inorganic substrates differing from silica and silicon (DLC, oxides) have been succesfully used, but the results are not mentioned here.

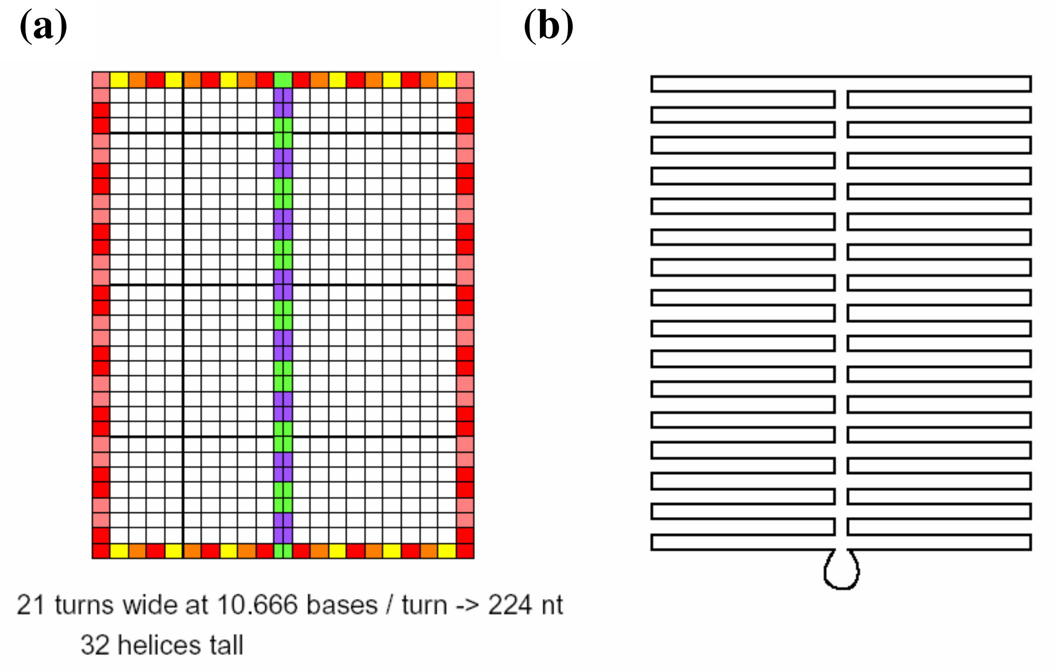

***FIGURE 4.7**. Details of "tall" rectangle design. (a) Block design for the "tall" rectangle. (b) Scaffold raster.*

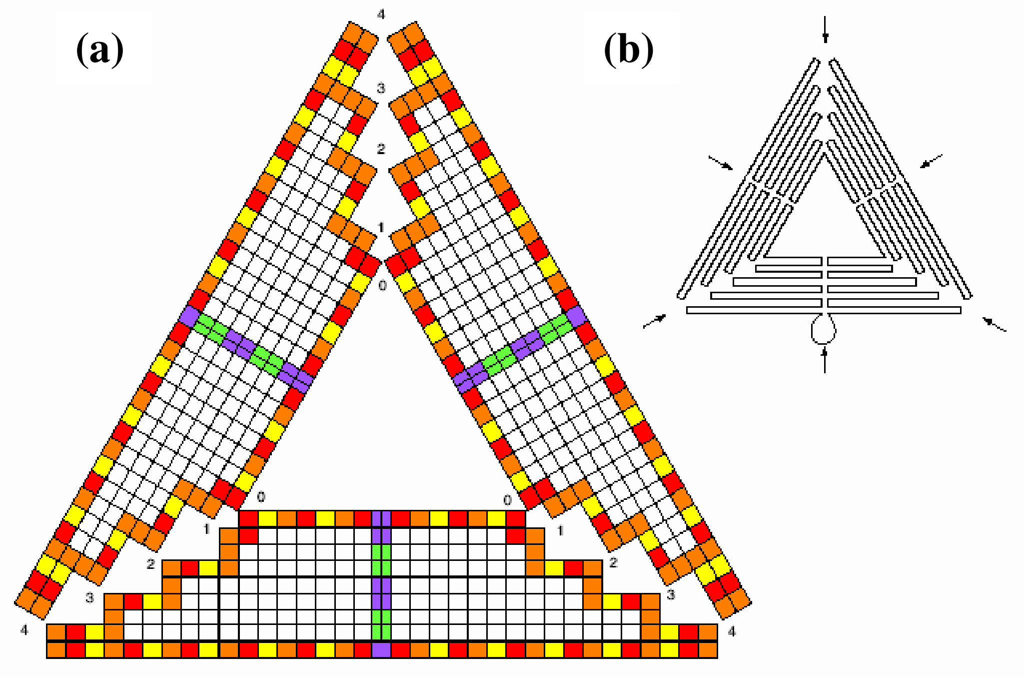

__FIGURE 4.8__. Details of sharp triangle design. (a) Block design for the sharp triangle composed of trapezoidal domains. (b) Scaffold raster, with arrows pointing at the seams where bridging staples are required.

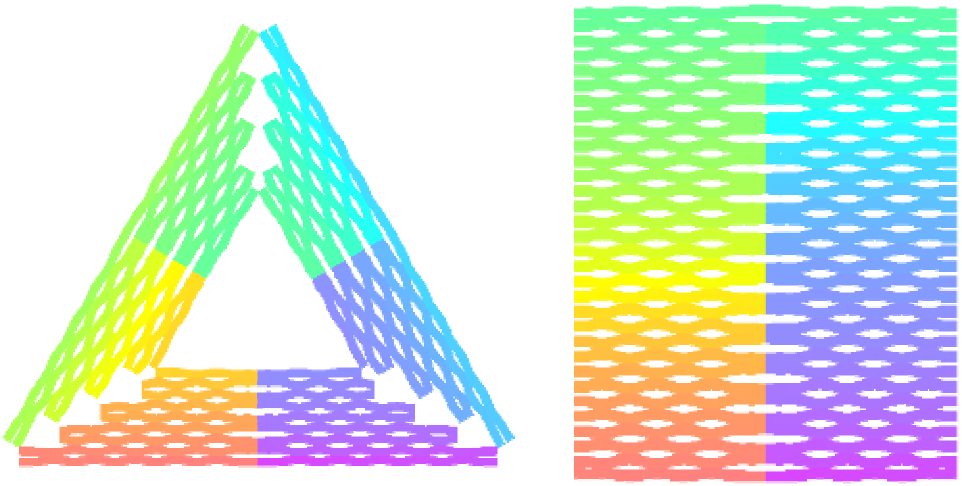

__FIGURE 4.9__. Basic crossover diagrams for the two studied structures.

Tall rectangles were further modified following two distinct strategies: In the first one, dumbbell "hairpins" were introduced in the sequence to show the addressability of specific sites, or pixels, in the structure (***FIGURE 4.10***). Then, a first example of functionalization was obtained, by introducing modified staples attached to biotin molecules that can bind streptavidin-modified gold nanoparticles (***FIGURE 4.11***).

In particular, end staples on the right long side of the rectangle have been modified by adding a AAAA tail bound to a biotin molecule. A 100-fold stoichometric excess was added to the oligo mixture without specifically replacing the unmodified oligos.

Gold nanoparticles were prepared following the well-known Turkevich method. After ultrafiltration, the particles were resuspended in water and a large excess of streptavidin was added. Electrophoresis in agarose gel was performed on the obtained mixture, and the selected fraction of streptavidin-functionalized particles was readily dissolved in the 10x TAE/Mg^{++} buffer and added to the solution containing the annealed biotin-modified "tall" rectangles.

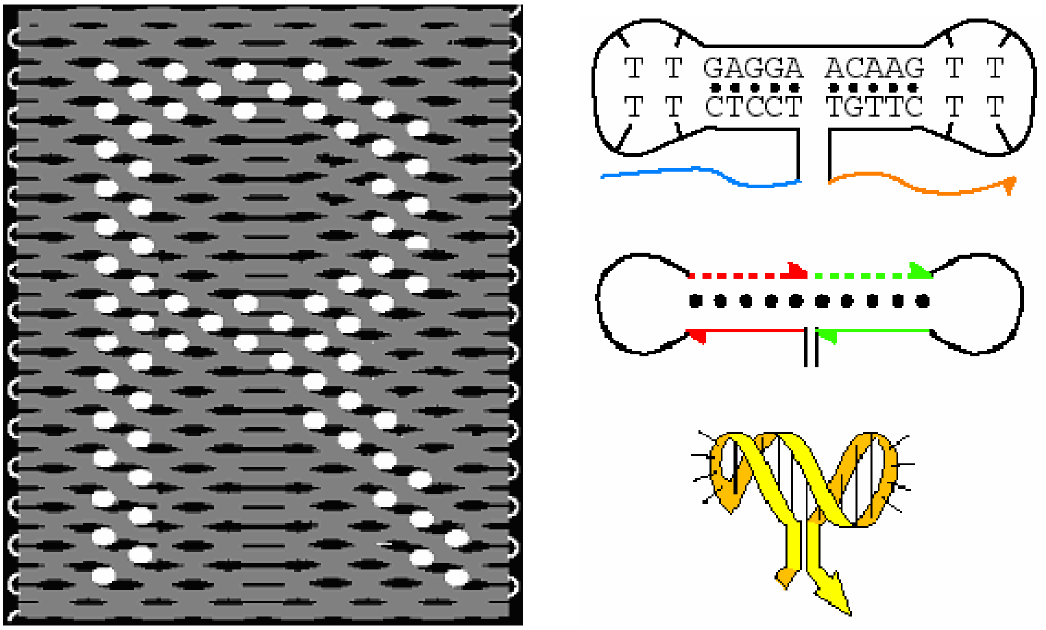

***FIGURE 4.10**. "R" letter on tall rectangle crossover diagram, showing the hairpins locations as white circles (left) and dumbbell hairpin sequence, coupling and helix structure (right).*

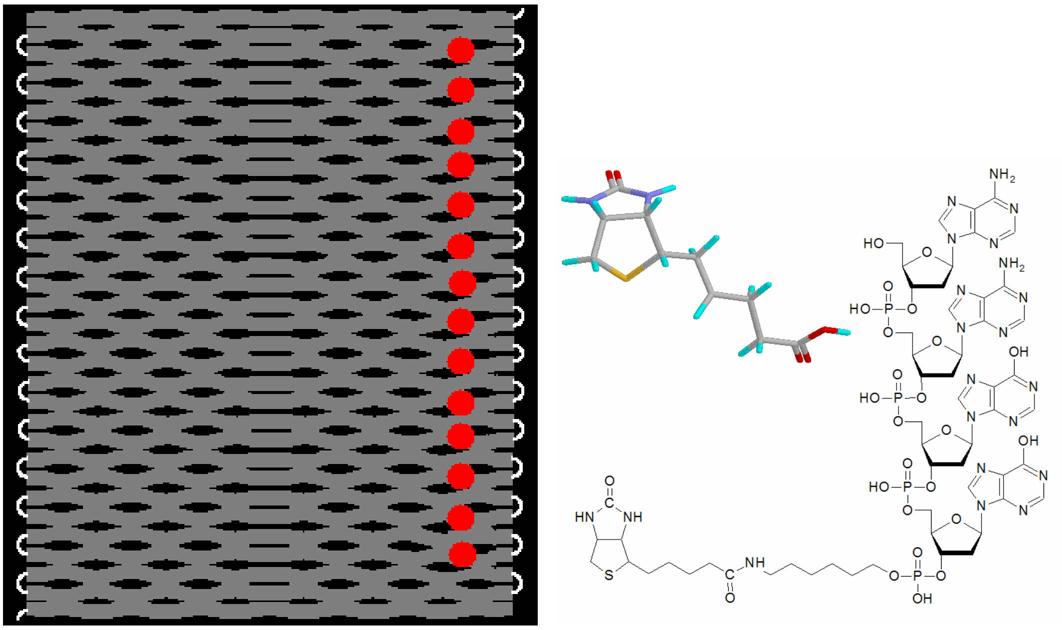

***FIGURE 4.11**. Biotin modificated tall rectangle crossover diagram, showing the locations with staples modified with a AAAA biotinated tail (left) and the biotin molecule in a wire model, next to the AAAA-biotin tail structure.*

4.4 Results and Discussion

The first AFM measurements were performed on “tall” rectangles (TR) and triangles with trapezoidal domains (TT) origami. The use of the liquid cell is almost compulsory when the purpose is to image extremely fine features (< 10 nm) of a soft material. When working in air, Van Der Waals forces and electrostatic interaction between the tip and DNA strands inavoidably result in the ripping and tearing of the structures, providing very little or no information on the quality of the origami. For similar reasons, tapping mode is preferred over contact mode. The open set-up of the liquid cell is quite convenient for routine measurements in standard conditions, as buffer solutions have no significant evaporation issues at room temperature and no solvent circulation is required for this set of experiments.

Mica is known to be an outstanding susbtrate for AFM imaging of DNA and DNA structures: cleaving yields a neutral, atomically flat surface where an elevated density of ions (Na^+, K^+) is present. When they are put in contact with a solution, alkaline ions (purple in ***FIGURE 4.12***) dissociate from the surface, leaving an unbalanced negative charge.

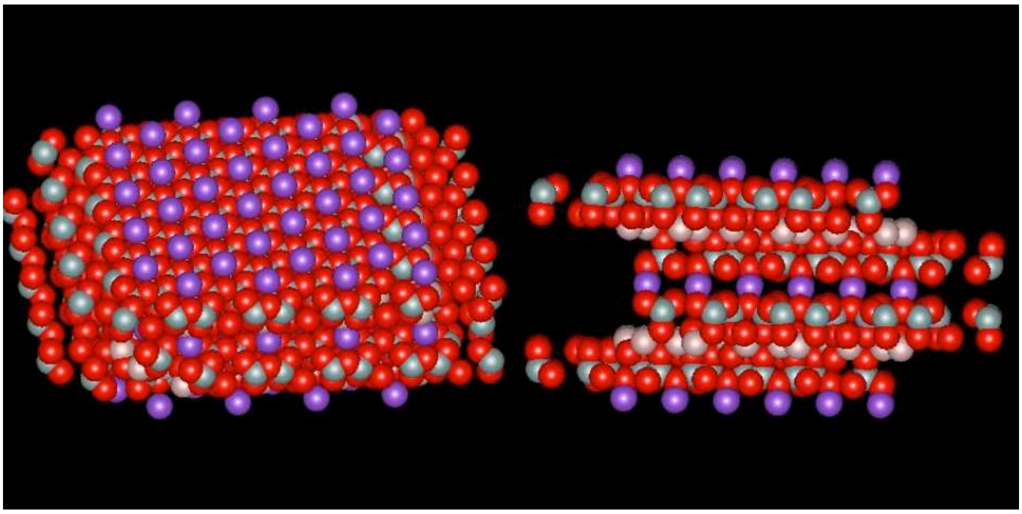

FIGURE 4.12. *3D model of mica structure.*

At the TAE pH conditions, DNA is negatively charged, but certain divalent cations (Mg, Ni, Zn,…) that can simultaneously replace the alkaline ions on mica and coordinate its phosphate groups, act as mediator for the DNA-mica interaction. Magnesium(II) in particular has proven to be ideal, as the strength of the interaction is high enough to prevent DNA dragging or removal, yet not to the point of inhibiting the proper and complete unfolding of the structures on the surface. Furthermore, magnesium(II) does not interact effectively with the excess strands, that remain in solution without sticking to the mica. Nickel(II) for instance is known to be an excellent cation for the imaging of linear DNA; unfortunately, its interaction is so strong and non-specific that all the unhybridized strands end up sticking on the substrate, making the imaging extremely difficult in the case of origami.

TRs and TTs AFM data are reported in ***FIGURE 4.13*** and ***4.14***.

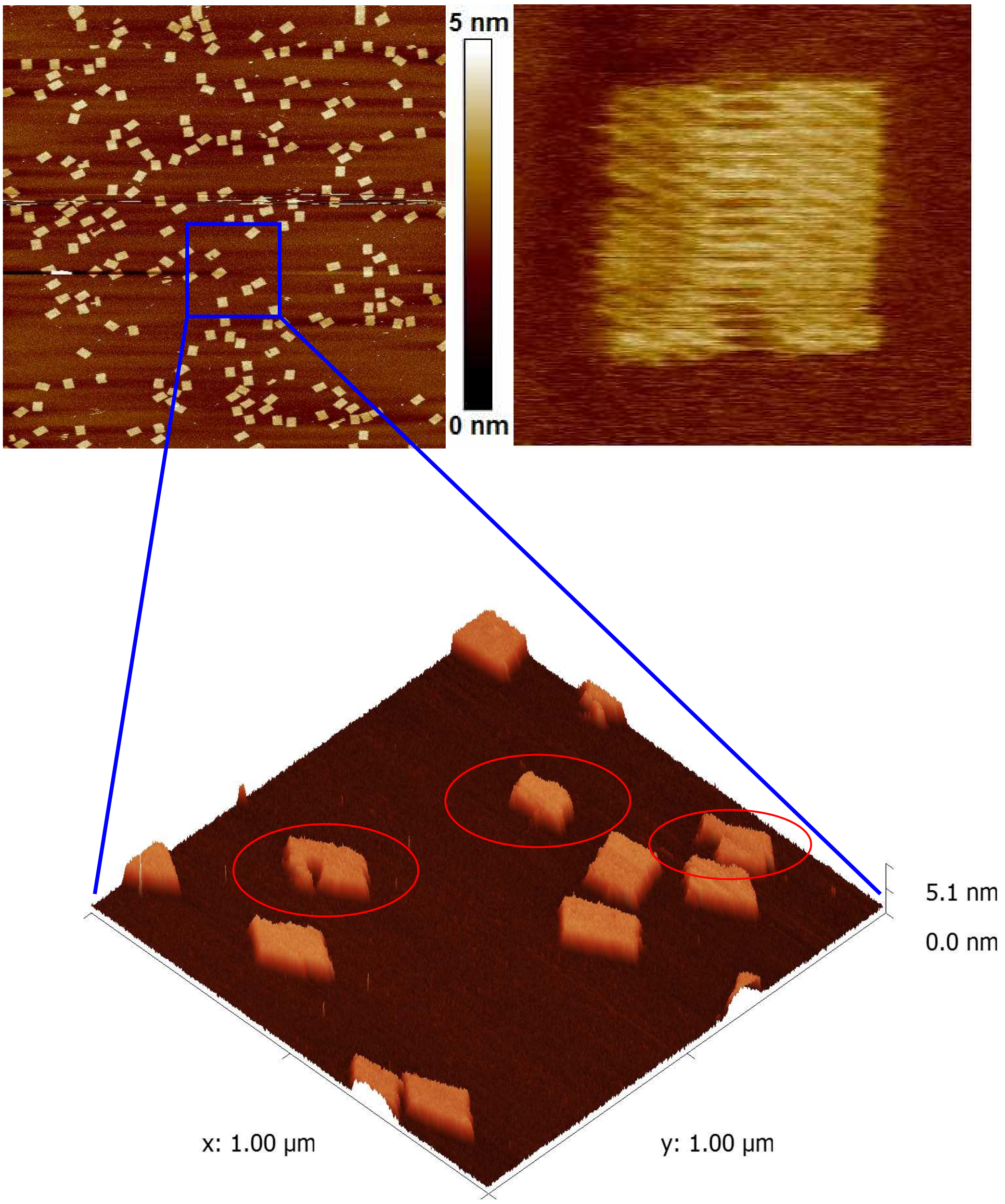

***FIGURE 4.13**. AFM height image of the tall rectangles. The image on the left (height) is 5 x 5 μm^2, the hi-resolution image on the right is 180 x 180 μm^2. The 3D plot highlights TRs with defects. Dents and rectangular fractions of TRs are marked with red circles. Notice the excellent matching between the high resolution height image and the basic crossover diagram in **FIGURE 4.9**.*

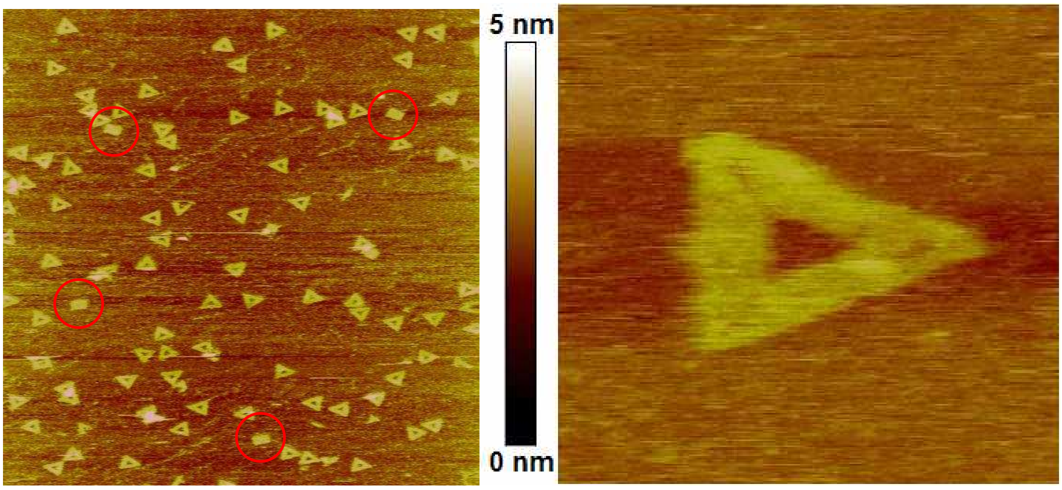

***FIGURE 4.14**. AFM height image of the triangles with trapezoidal domains. The image on the left (height) is 5 x 5 μm^2, the hi-resolution image on the right is 180 x 180 nm^2. Notice the presence of some TRs impurities(red circles, left), related to the use of an AFM tip precedently used to image TRs.*

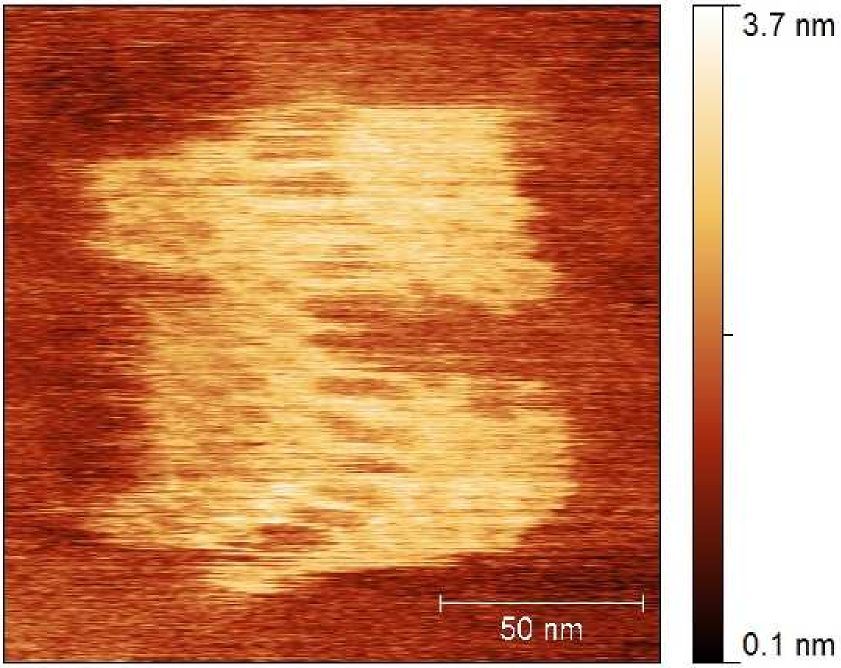

***FIGURE 4.15**. After multiple scans, the TR imaged in FIGURE 4.13 is eventually damaged by the AFM tip.*

While the defects highlighted in ***FIGURE 4.13*** are connected with a non-perfect scaffold integrity (missing parts in its circular sequence result in missing sections in the structure, keeping in mind the chosen raster path), in ***FIGURE 4.15*** a typical example of tip-induced damage is reported. After multiple scans, the TR is eventually ripped and the structure is deformed by the interaction with the scanning tip. The differences between the two kinds of defectuality are anyway quite significant, allowing to discriminate between a defective sample and an inefficient tip.

In the TT sample, some TRs are also present: such impurities come from the use of a tip which had just been used to image the other structure. The specificity of the 200-strand , 32mer oligo mix together with the design that defines the desired origami don't allow for the formation of unwanted structures, if not for the previously shown (***FIGURE 4.13***, bottom) occasional partial formation.

A further confirmation of the complete addressability of specific locations, or pixels, on the origami comes from the "R" letters on TRs. Once the oligo mix sequencing is complete, it's possible to add extra dumbbell hairpins by modifing specific staple sequences. The knot-like folding of the hairpin results in a bump on top of the TR, thereby introducing a third dimensionality in the structure. The nature itself of the double helix conformation determines the orientation (top or bottom face) of the bump. In ***FIGURE 4.16*** a few images of "R" on TRs are reported. Thanks to the chirality of the "R" letter, it's possible to infer the top-down face orientation of the TRs. By looking at over 200 single origami, it results that in the 75% of the cases Rs are facing upwards, thus suggesting some local structure stiffness as hairpins are expected to provide the same affinity for the substrate as the main scaffold. A preferential orientation may therefore be linked to an overall reduced surface interaction on the patterned face, which is explicable only by implying that hairpins inhibit the adhesive forces of the neighboring supporting strands.

As evidenced in ***FIGURE 4.16***, facing down Rs are way more subject to damaging, usually a consequence of inefficient sticking that results in the tip dragging origami around, and often lying not perfectly flat and unfolded. Notice also how TRs are not perfectly symmetric with respect to the middle short axis: in fact, the unused portion of the scaffold strand protrudes as an unstructured double helix, where short (< 26 nt) “remainder strands” are added to complement unused sequence, at the middle of one of the short sides.

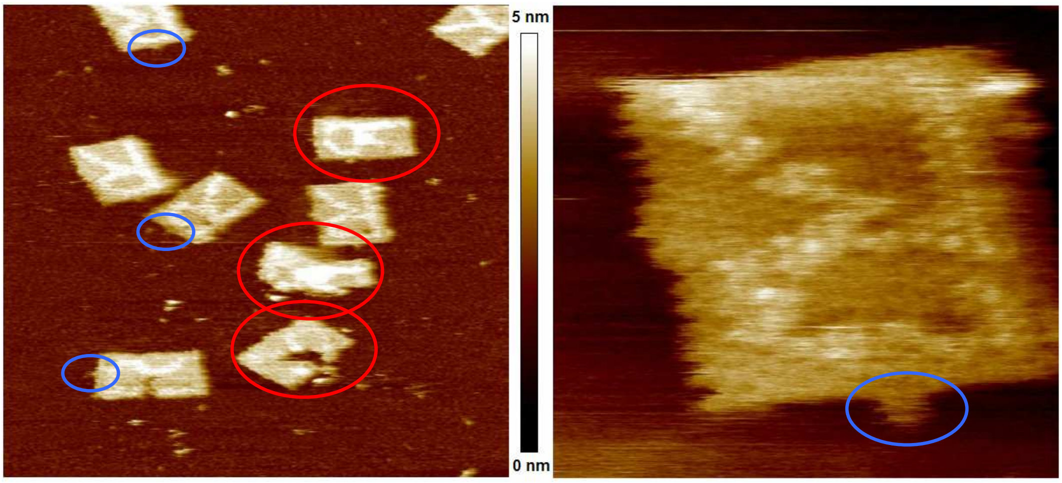

FIGURE 4.16. *AFM height images of tall rectangles with letter “R”, obtained through the introduction of hairpins at defined locations (1 x 1* μm^2 *left, 180 x 180* nm^2 *right). Preferential top orientation for the R-modified face is noticeable, as well as some tip-induced or incomplete unfolding damage on the downfacing Rs (red circle). Excess scaffold strand is marked with blue circles.*

When dealing with biologial molecules, a commonly used system with a lock-and-key interaction is streptavidin-biotin (***FIGURE 4.17***). Streptavidin is a protein with four active sites that can bind four molecules of biotin, a vitamin that can be found in in tissues and blood, with the strongest protein-ligand non-covalent interaction known in nature. This bond is essentially irreversible and can withstand organic solvents and denaturing agents in a wide range of pH. Furthermore, streptavidin has an excellent affinity to gold, suggesting an effective way to introduce gold nanoparticles in the structure.

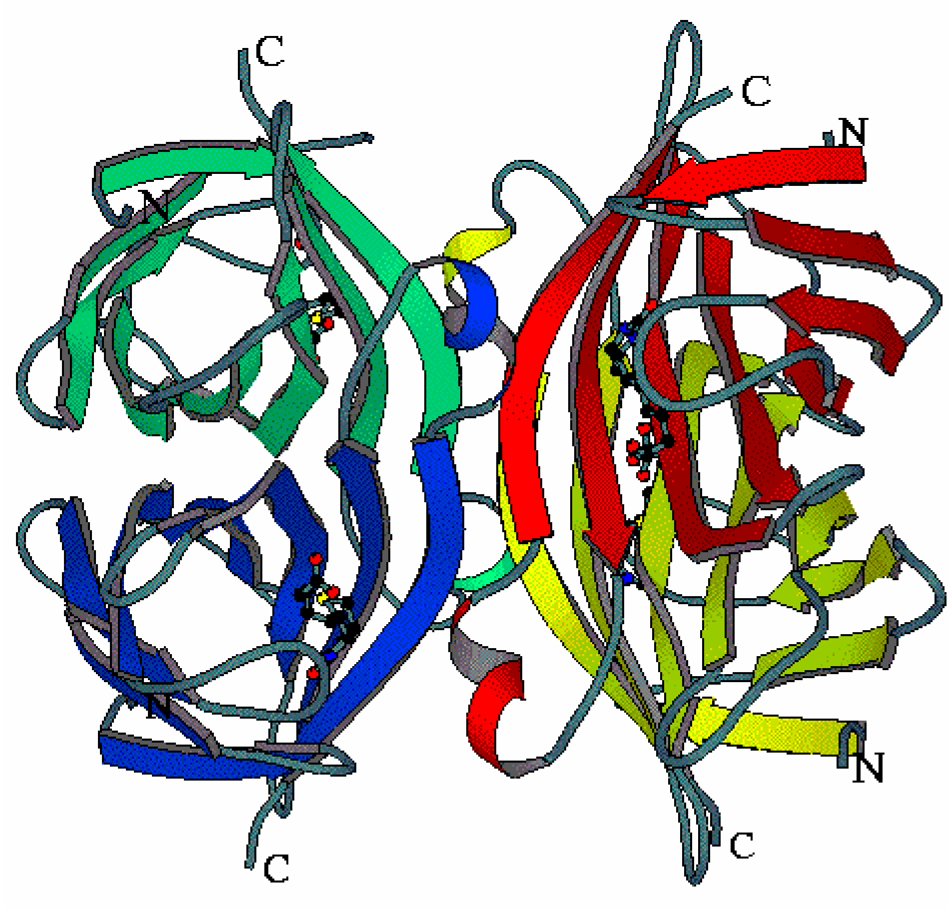

***FIGURE 4.17**. Streptavidin tetrameric structure (middle) coordinating and binding 4 molecules of biotin.*

As a first example, TR origami were prepared with a modification of the staple strands along one side. The modified strands now carry a short AAAA tail with a biotin molecule. Biotin (< 1 nm in length) is too small to be positively identified on top of an origami, but the effectiveness of the modification can be estimated indirectly by observing the coupling of streptavidin-modified AuNPs (***FIGURE 4.18***). In these samples, the presence of AuNPs bound to the origami surface is clearly noticeable in the height image of the AFM measurement. But besides the topography, the phase data are much more informative: in ***FIGURE 4.19*** they are compared to the data related to the hairpin modified TRs with the letter "R". The most striking difference is related to the significatively different phase contrast of the AuNPs with respect to the dumbbell hairpins. Phase measurements are sensitive to local differences in viscoelasticity and adhesion between the AFM tip and the sample, and here indicate the consistent contrast existing between gold and DNA, while being hairpins made of DNA strands almost no contrast is detectable.

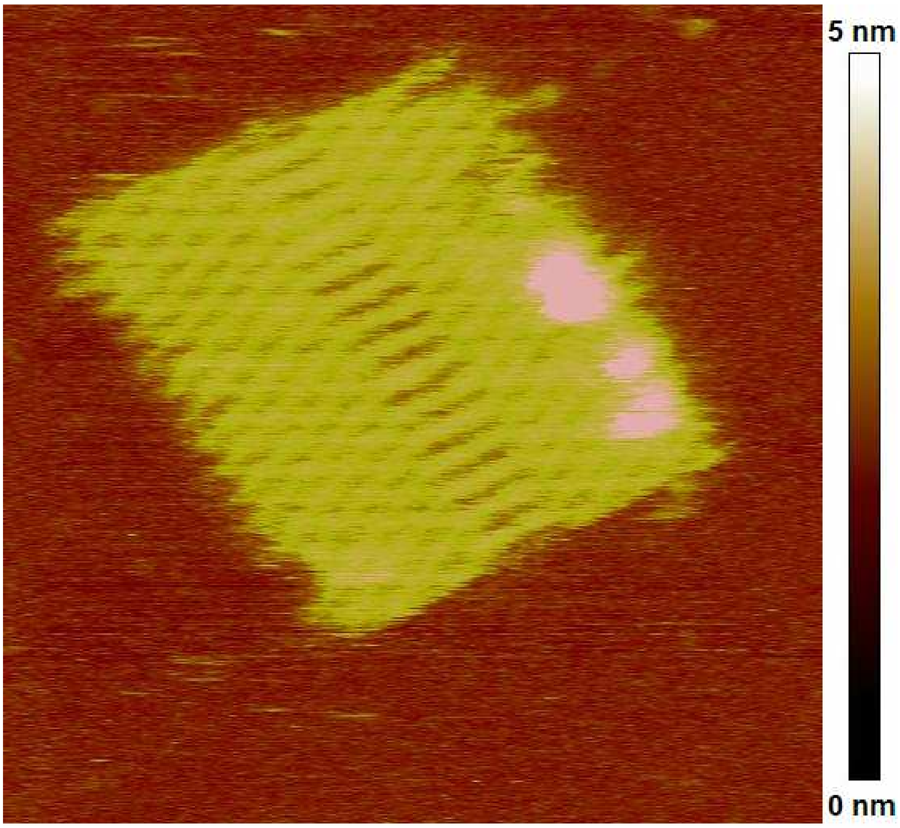

***FIGURE 4.18**. AFM height image showing the position of AuNPs on biotinated TRs. The imaged area is 180 x 180 nm^2.*

Clearly, the functionalization is not fully completed, as at most 7 AuNPs have been observed out of the potentially available 14 sites. In the preaparation of these origami, the original, unmodified strands were not removed, thereby competing with the large excess (10:1) of biotinated strands for the formation of the final structure. It's possible to hypothesize a general advantage of the original shorter strands over strands that carry an extra uncompatible functionality. Then, as every single AuNP is coated with several streptavidin units, they might be bridging two neighboring biotinated sites. Finally, some purity issues on the modified oligo batch have been raised after running some control electrophoresis measurements. Apart from the technical contingencies, the fact that a single AuNP may easily bridge multiple biotinated strucures is supported by some other experimental observations. The attachment of the nanoparticles is in fact succesful only after the deposition of pre-formed origami; introducing the streptavidin-AuNPs directly in the strand mix or to the post-annealing origami solution does not provide the desired outcome. A possible interpretation lies in the fact that as every single streptavidin moieties can bind up to four biotin molecules, the quick formation of these complex either prevents the participation of the biotinated strands in the self-assembly of the origami, or bridges distinct, well-formed structures, thus making their imaging extremely difficult.

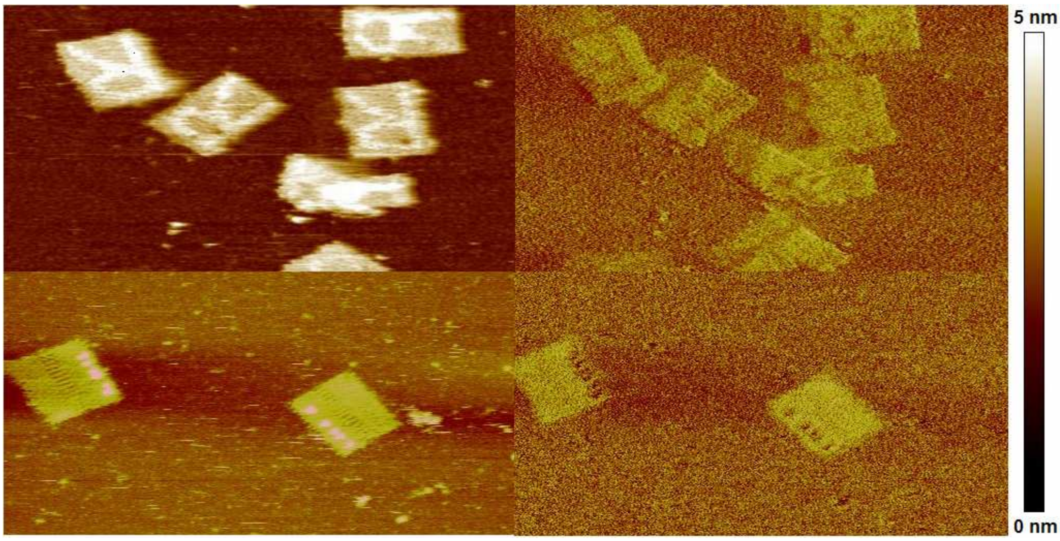

FIGURA 4.19. *AFM image (left: height 981 x 490 nm^2; right: phase 981 x 490 nm^2; top: TRs with R; bottom: TR with AuNPs) of the modified TRs.*

Many strategies can potentially avoid such issues; the most common approach consists in the preventive saturation of the excess binding sites on streptavidin through the addition of stoichometric amounts of biotin prior to AuNPs functionalization.

4.4.1 Other Substrates

Different materials have been examined as potential substrates for DNA origami imaging. A substitute is quite desirable: in fact, while mica is ideal for imaging, it's proven to be extremely disadvantageous for processing: it's insulating, extremely hydrophilic and with very weak layer-to-layer interactions that make it difficult to handle and clean. The combination of these properties makes it hard to pattern with optical lithography techniques (some success has been obtained with a contact mask) while little or no success has been obtained with e-beam due to the peel-off of the working surface at different stages of the process.

Starting from these assumptions, the ideal alternative substrate should be easily processable and in general compatible with standard lithographic techniques, be extremely flat, carry negative charges on its surface (and possibly have some tunability of charge density or spacing) and shouldn't dissolve or swell in water.

An interesting candidate is polystyrene: besides being easily spin-coatable with a very low surface roughness, when it is UV-ozone treated, its surface becomes more and more hydrophilic through the addition of O^- groups on the polymer chain. AFM topograms show that while the sticking is effective and surface roughness satisfactory, hi-resolution imaging cannot be achieved due to some failures in the sticking of the DNA structures. Such failures can be of different kind: they can be related to insufficient sticking, that leads to the AFM tip dragging the DNA tiles as it scans; on the other hand, if the sticking is excessive DNA tiles might not be able to flatten out and fully adhere to the surface, resulting in crumpled structures. The effectiveness of sticking on mica can be related to an ideal charge density and distribution and to the presence of sites for cations where specific elements fit in better than others. Furthermore, UV-ozone treated polystyrene is known to have some aging issues, as the structure rearranges over time to minimize the surface energy and thus reducing the availability of charged groups.

Another common approach in literature relies on the surface modification of silicon with aminopropyl-triethoxy-silane (APTES). While through wet-chemistry the results are not always reproducible, the vapor phase approach has proven to be way more satisfactory from the point of view of surface roughness, presence of impurities and reproducibility. The primary amine end-group ($pk_a \sim 9$) is positively charged at the buffer pH (~7), thus suggesting that direct electrostatic interaction between DNA and a surface is possible without the mediation of buffer cations. Again, the sticking appears to be effective but not strong enough to grant a stable adhesion of the tiles, as can be noticed from the horizontal drag lines in ***FIGURE 4.20***.

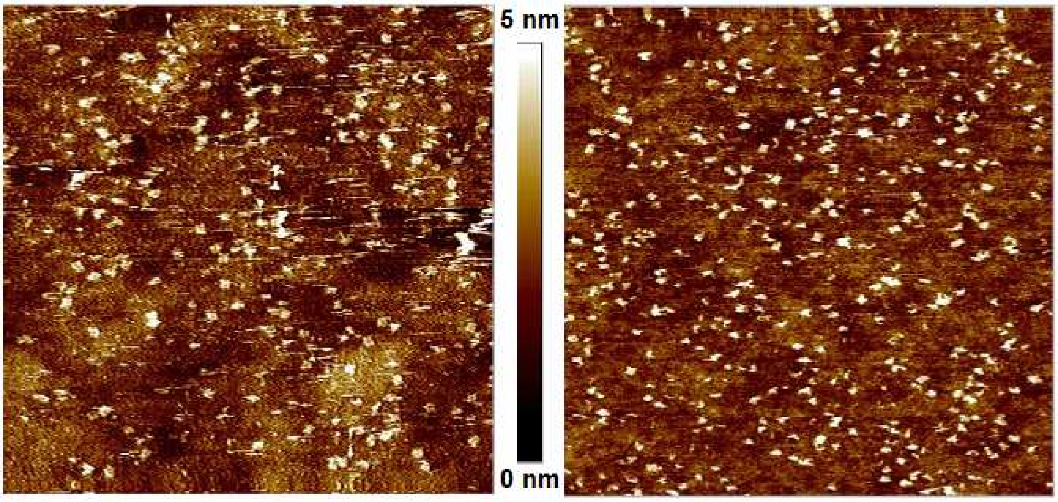

FIGURE 4.20. *AFM height topogram of DNA tall rectangles on Si/APTES (left) and UV-ozone treated polystyrene (right)..*

A more successful experiment consisted in the use of surface modified polyimides. Polyimides are commonly used in nanofabrication for their excellent thermal and mechanical properties and theur high dielectric constant, and a wide variety of them is readily available. The modification step consists in the opening of the imide ring with a strong base (KOH, NaOH) and the formation of the carboxylate, as previously shown in **CHAPTER 3**.

The carboxylate potassium or sodium salts quickly undergo an ion exchange reaction with the ionic species that are present in the buffer solution, recreating a situation analogous to what happens with mica. Furthermore, different types of polyimides have different monomeric length, surface energy and packing densities that result in an overall different charge spacing on the surface, so that the sticking efficiency can be tuned.

A few in-house and commercial polyimides have been tested; the general approach consisted in depositing a droplet of a highly concentrated (1 ÷ 5 M) aqueous solution of NaOH or KOH at room temperature on the polyimide film, followed by a thoroughful rinsing of the film until no salty residue is visible on the surface after blow-drying.

The best preliminary results have been obtained with fluorinated polyimides, and especially 6FDA-6FipDA (***FIGURE 4.21***). This polyimide is transparent and soluble in NMP, THF, anisole, chloroform, acetone, cyclohexanone, amides, making it easily processable. Furthermore, the presence of fluorine significately decrease the surface energy of the unmodified polymer, determining a significative contrast with the modified polymer and suggesting a potential strategy to pattern a surface just by alternating modified and unmodified areas.

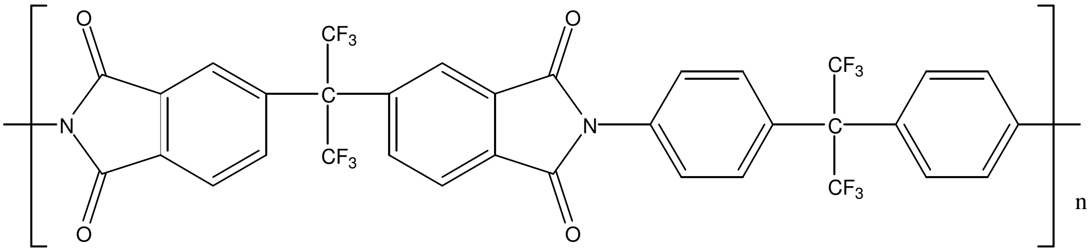

FIGURE 4.21*. 6FDA-6FipDA polyimide structure. Further details can be found in* ***CHAPTER 3****.*

A satisfactory adhesion was obtained, as can be seen in ***FIGURE 4.22***. Notice how the cavity at the center of the triangles can be resolved. Some rugosity with a ~ 1 μm periodicity can be noticed as well. The image size is 3 μm.

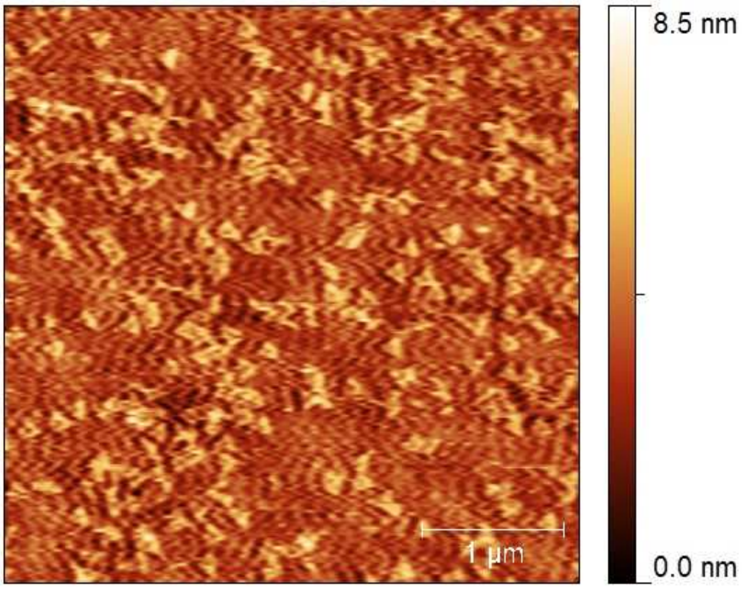

***FIGURE 4.22**. AFM height image of TTs on 5M KOH treated 6FDA-6FipDA.*

6FDA-6FipDA is a good but not unique candidate, and a systematic study of different polyimides might be useful to identify the optimal substrate. The modification procedure on the other hand has been studied quite well in literature, and a short modification time coupled with a strong base concentration appear to be necessary in order to fully open the imide ring just on the topmost layer(s) of the polymer film. A longer soaking time would result in a deeper modification returning a gel-like structure with low stability and high roughness; a lower concentration would result in an overall lower density of charged groups due to incomplete modification.

4.5 Why does scaffolded DNA origami work?

The scaffolded self-assembly of DNA strands has been used to create linear structures[17,18] and proposed as a method for creating arbitrary patterns[18,19]. But the widespread use of scaffolded self-assembly, and in particular the use of long DNA scaffolds in combination with hundreds of short strands, has been inhibited by several misconceptions: it was assumed that (1) sequences must be optimized[20] to avoid secondary structure or undesired binding interactions, (2) strands must be highly purified, and (3) strand concentrations must be precisely equimolar. These three criteria are important for the formation of many DNA nanostructures and yet all three are ignored in the present method.

Consider any secondary structure that the scaffold might assume. It is unlikely that this secondary structure perfectly blocks the binding sites for all the staple strands that should bind its sequence. Thus staple strands may bind by partial matches at first, and then participate in a branch migration that displaces the secondary structure. A longer region of complementarity between the staple and the scaffold stabilizes the staple-scaffold interaction over the scaffold secondary structure. The excess of staple strands may help drive this process, and has been used to actuate nanomachines[21-23].

Another factor that may work against scaffold secondary structure is the role of staple strands as intramolecular bridges. Each successful addition of a staple strand organizes the scaffold for subsequent binding of adjacent staple strands and constrains the scaffold in a way that precludes a large set of undesired secondary structures. Thus one might expect the binding of staple strands to be highly cooperative. To see why intramolecular interactions may be important, consider cutting a scaffolded shape into a multi-stranded structure based on unique tiles (for which the minimum free energy state should be the scaffolded shape, just with more backbone nicks). For such a system the addition of a tile at any one position does not significantly constrain the global structure.

Next consider the interactions of staple strands with themselves. Many strong complexes exist between them; none is a perfect match, however. The scaffold can displace such structure and gain a required staple strand.

Now consider purity. A truncated staple strand might bind to the scaffold. However, because of the excess of staple strands, there exist many full-length length staple strands that can bind and displace the truncated strand. This means that only the purity of the scaffold matters; because the scaffold is derived from a biological source, it is very pure.

In a similar way, because staple strands do not bind to each other, the relative stoichiometry between the staple strands does not matter. With staple strands in excess over the scaffold, the remaining relevant concentration is the effective local concentration of scaffold in intramolecular events. Here the intramolecular nature of scaffold folding enforces a kind of equimolarity, as any two sections of the scaffold that are brought together by a staple strand are by definition, equimolar. Again, such could not be said for the same sections if the scaffolded structure were cut into multi-stranded unique tiles. This highlights a crucial difference between the scaffolded method shown here and that previously proposed[17,18]. In the latter scheme the scaffold runs through every other helix; the structure is held together by interactions between multi-stranded tiles and so the staple strands must bind to each other. For such schemes precise equimolarity is likely important.

This initial study on origamis has the purpose of providing an overview on the capabilites of these structures as potential tools for materials chemistry and nanotechnology; they are currently being evaluated as potential building blocks in nanoelectronics, while the biological potentialities are clear and go far beyond the writer’s understanding.

4.6 References

1. Feynman, R. P. There's plenty of room at the bottom. *Engineering and Science* 23(5), 22–-36 (Caltech, February, **1960**).
2. Junno, T., Deppert, K., Montelius, L. & Samuelson, L. *Appl. Phys. Lett.* 66, 627-3629 (**1995**).
3. Eigler, D. M. & Schweizer, E. K. *Nature* 344, 524-526 (**1990**).
4. Heinrich, A. J., Lutz, C. P., Gupta, J. A. & Eigler, D. M. *Science* 298, 1381-1387 (**2002**).
5. Whitesides, G.M., Mathias, J. P. & Seto, C. T *Science* 254, 1312-1319 (**1991**).
6. Yokoyama, T., Yokoyama, S., Kamikado, T., Okuno, Y. & Mashiko, S. *Nature* 413, 619–621 (**2001**).
7. Mao, C. B. et al. *Science* 303, 213-217 (**2004**).
8. Seeman, N. C *J. Theor. Biol.* 99, 237-247 (**1982**).
9. Seeman, N. C. & Lukeman, P. S. *Rep. Prog. Phys.* 68, 237-270 (**2005**).
10. Chworos, A. et al. *Science* 306, 2068–2072 (**2004**).
11. Park, S. H. et al. *Angew. Chem.* 118, 749–753 (**2006**).
12. Chen, J. & Seeman, N. C. *Nature* 350, 631-633 (**1991**).
13. Zhang, Y. & Seeman, N. C. *J. Am. Chem. Soc.* 116, 1661-1669 (**1994**).
14. Shih, W. M., Quispe, J. D. & Joyce, G. F. *Nature* 427, 618–621 (**2004**).
15. Rothemund, P. W. K., *Nature* 440, 297-302 (**2006**).
16. Rothemund, P. W. K. et al. *J. Am. Chem. Soc.* 26, 16344-16353 (**2004**).
17. LaBean, T. H., Winfree, E. & Reif, J. H. in *DNA Based Computers V* (eds Winfree, E. & Gifford, D. K.) 123–-140 (Vol. 54 of DIMACS, AMS Press, Providence, Rhode Island, **1999**).
18. Yan, H., LaBean, T. H., Feng, L. & Reif, J. H. *Proc. Natl Acad. Sci. USA* 100, 8103-8108 (**2003**).
20. Seeman, N. C. J. *Biomol. Struct. Dyn.* 8, 573-581 (**1990**).
21. Yurke, B., Turber_eld, A., Mills, Jr., A., Simmel, F., and Neumann, J. *Nature* 406, 605-608 (**2000**).
22. Simmel, F. and Yurke, B. *Physical Review E* 63, 041913-1-5 (**2001**).
23. Yan, H., Zhang, X., Shen, Z., and Seeman, N. *Nature* 415, 62-65 (**2002**).

Final Considerations

In this thesis, the potential functional interactions of gold nanoparticles with organic, hybrid, inorganic and biological systems have been investigated. Nanoparticles with varying sizes have been synthesized following different preparation methods.

Molecular-like ($D < 2$ nm), highly fluorescent few-atoms clusters were prepared by a slow reduction of gold salts in organic solvent, yielding a colloidal solution that can be easily redispersed in a variety of solvents and matrices, including sol-gel silica and a hybrid copolymer. The emission wavelength has a lifetime in the ns and can be tuned from the near UV to the whole visible range by adjusting the reaction parameters, and the luminescence is stable for months both in intensity and wavelength. Use of alternative precursors and solvents, influence of reaction temperature and purification methods are all currently being investigated, together with potential application as biolabels and sensitizers for rare-earth-based optical amplifiers.

Uncapped nanoparticles with 3 nm $< D <$ 10 nm were obtained in situ in fluorinated polyimides via thermal reduction-precipitation with the concurrent matrix imidization. The doping profile, monitored with RBS analyses, can be easily varied both for thick (30 μm) and thin (< 1 μm) film samples. The selective permeability properties that are typical of polyimides suggest potential employment as both optical and electic gas sensors, and the first measurements are now underway.

Eventually, 10 nm nanoparticles were synthesized with the traditional Turkevich citrate method, capped with streptavidin and used to functionalize DNA origami structures. Liquid cell AFM technique allows to image the effectiveness of the proposed method for positioning nanoscopic objects with nm resolution thanks to the peculiar design features of these DNA-based structures. The specific interest is here related to the possibility of using them as lego-like building blocks for nanoelectronics, and the focus is at present centered on the self-induced or externally directed organization of the functionalized origami on substrates. At present, self-assembly on patterned surfaces is being studied together with AFM electrophoresis, but new interesting strategies are being proposed on a daily basis as further interesting origami peculiarities emerge.

In conclusion, this thesis has allowed me to come in contact with an unforeseen number of synthetic methods and characterization techniques, along with the researchers who dedicated part of their time to instruct and discuss. Many questions are still open, and many ideas are worth being tested. In general, a lot of work needs to be done: but certainly the variety of people, places and topics I've been involved with have made the researching experience entertaining and rewardful, every day.

Appendix

Synthesis and Characterization of Trimethoxysilyl-propyl-methacrylate (TMSPM) and Methyl-methacrylate (MMA) Inter-Penetrating Networks

A1.1 Synthesis

Acrylic polymers and copolymers of TMSPM (Aldrich) and MMA (Aldrich, deinhibited through column) were prepared at a 25 wt.% concentration using tetrahydrofuran (THF) or toluene.

Photopolymerization of the acrylates was initiated by azobisisobutyronitrile (AIBN, Aldrich) under 365 nm irradiation from an 8W UV-lamp. The molar ratio of initiator to monomer was varied by orders of magnitude between 1:10 or 1:1,000,000. Crosslinked samples were prepared by HCl catalyzed hydrolysis of the alkoxysilane groups in THF/polymer solutions. The concentration of acid was varied, but a water:silane ratio of 3:1 was held constant unless otherwise noted.

Thick films were made by casting acidified polymer solutions into glass containers (2.5 cm diameter) or custom-made Teflon scaffolds and allowing them to dry under ambient conditions. The drying procedure was performed in air and involves at least 12 hours at 80 ^{o}C (after heating at 2 ^{o}C/min) followed by 3 hours at 100 ^{o}C (after heating at 1 ^{o}C/min). Selected dry films were then cured at either 150 or 200 ^{o}C in air for an additional 3 hours (heating and cooling rates were equal to and less than 1 ^{o}C/min, respectively).

Methanol or ethanol can also be used as solvents, either for the starting precursors or for the vacuum-dried copolymers. However, in this case either lower dilution (up to 10 wt.%) or higher temperature (40 °C for methanol or 50 °C for ethanol) are required in order to prevent phase separation and obtain stable solutions.

A1.2 Characterization

In the following pages, the full set of experimental data for the synthesized hybrid copolymer is provided. A detailed explanation can be found in Harreld et al., *Chem. Mater*, 15 (**2003**), 3481.

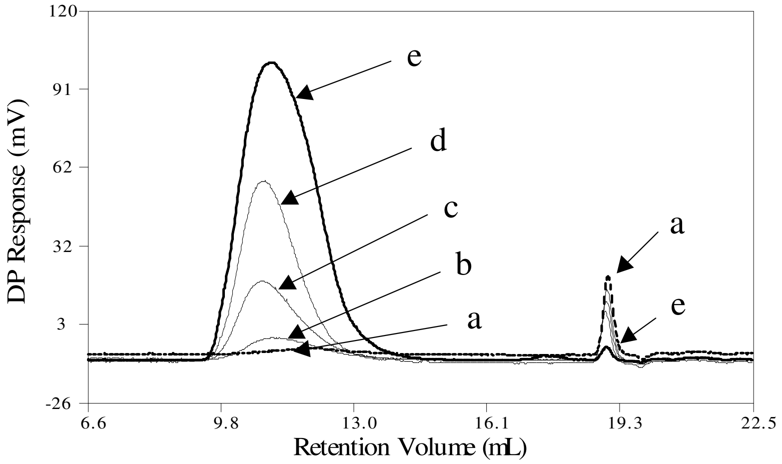

Figure A1.1. GPC data from viscosimetry detector for TMSPM homopolymer samples prepared using UV exposure of (a) 1, (b) 3, (c) 7, (d) 14, and (e) 96 hours; ratio of initiator:monomer = 1:10,000.

Monomer Conversion	Gelation Time*
0	$> 2 \times 10^4$
6	$> 2 \times 10^4$
20	18
60	8

Table A1.1. Gelation times for TMSPM homopolymer in the presence of residual TMSPM monomer (* In each case the total concentration of acrylate units and HCl is the same).

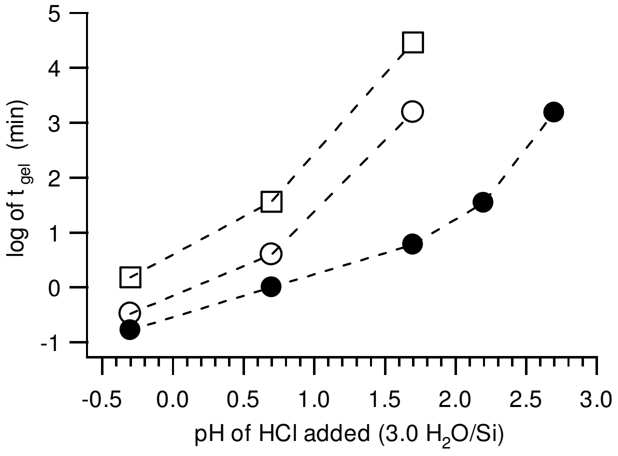

Figure A1.2. Relationship between gelation time (in sealed vials at 25 wt.% in THF) and HCl concentration for homopolymer (1:0 TMSPM:MMA) of high M_w (280,000 amu, closed circles) and low M_w (9,100 amu, open circles) and for copolymer (1:2 TMSPM:MMA) of low M_w (9,700 amu, open squares).

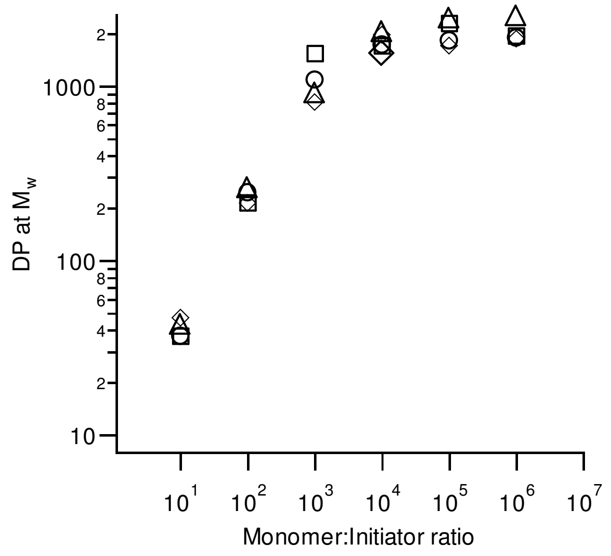

Figure A1.3. The degree of polymerization at the M_w as a function of the monomer:initiator ratio for polymer compositions of 1:0 (circles), 1:1 (squares), 1:3 (triangles), and 0:1 (diamonds) TMSPM:MMA.

TMSPM:MMA	AIBN:Monomer	M_w (amu)	DP_w (mer)	PDI	a_{MH}
1:0	1:10	18,000	71	1.7	0.83
	1:1000	260,000	1000	1.5	0.87
1:1	1:10	17,000	97	1.7	0.85
	1:1000	220,000	1200	1.4	0.87
1:2	1:10	16,000	110	1.8	0.85
	1:1000	190,000	1200	1.4	0.88
1:4	1:10	20,000	160	2.1	0.87
	1:1000	190,000	1500	1.4	0.87

Table A1.2. GPC data from TMSPM-MMA copolymer solutions (DP_w = degree of polymerization at M_w, PDI = polydispersity index, a_{MH} = Mark-Houwink parameter).

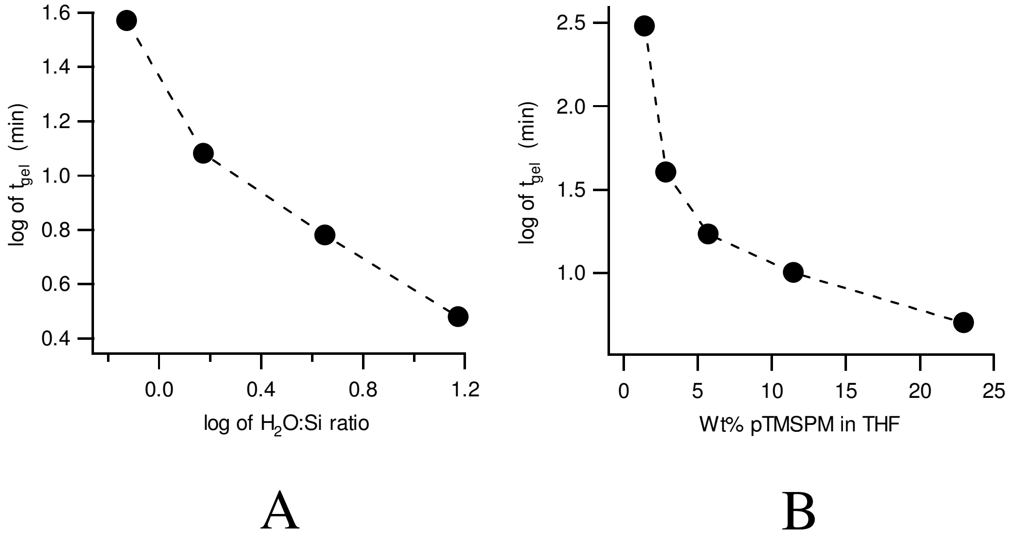

Figure A1.4. The dependency of TMSPM homopolymer gelation rate on (A) H_2O:Si ratio for a 23 wt.% solution in THF using 0.020 N HCl, and (B) polymer concentration in THF using a 9:1 ratio of H_2O:Si and 0.020 N HCl; the homopolymer was synthesized using a ratio of 1:100.

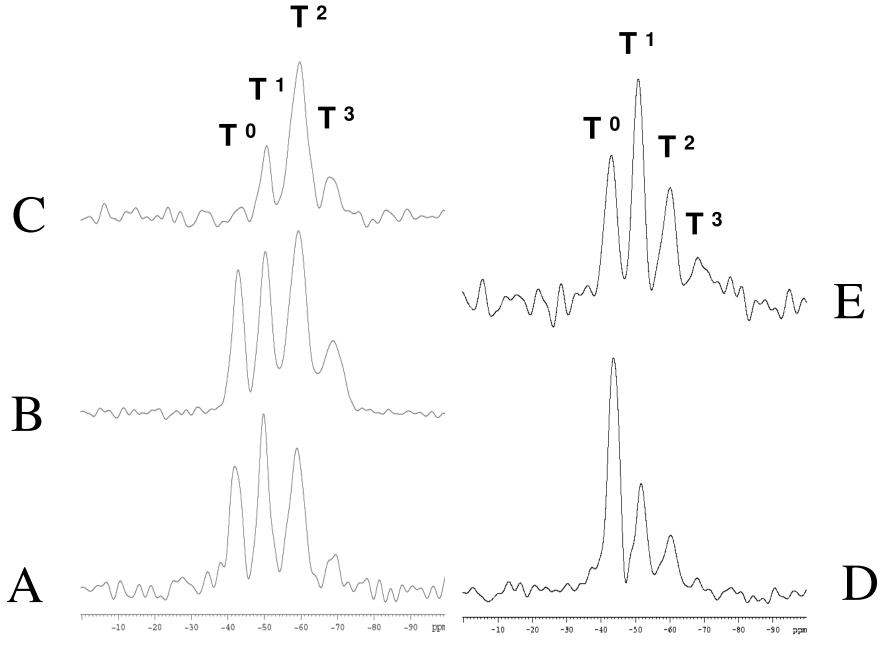

Figure A1.5. ^{29}Si NMR data for homopolymer (A-C) and 1:4 TMSPM:MMA copolymer (D, E) films representing different chemical and thermal crosslinking treatments. The samples were obtained using the following pairs of acid concentration (normality N of the added solution, H_20 : Si = 3) and cure temperature: (A) 0.02 N, 100 °C; (B) 0.02 N, 150 °C; (C) 0.10 N, 100 °C; (D) 0.02 N, 150 °C; and (E) 0.02 N, 200 °C.

pH of Acid Added (N)	T_{cure} (^{o}C)	T^0 (mol. %)	T^1 (mol. %)	T^2 (mol. %)	T^3 (mol. %)	Degree of Condensation (%)	HP
0.02	150	64	22	14	0	17	4H
0.02	200	28	39	22	11	39	7H

Table A1.3. ^{29}Si NMR and hardness data from solvent-cast, thick (~0.8 mm) films from crosslinked copolymer (1:4 TMSPM:MMA, 20 k amu); HP ~ pencil hardness. T^N indicates the degree of crosslinking, where N equals the number of ≡Si–O–Si≡ bonds.

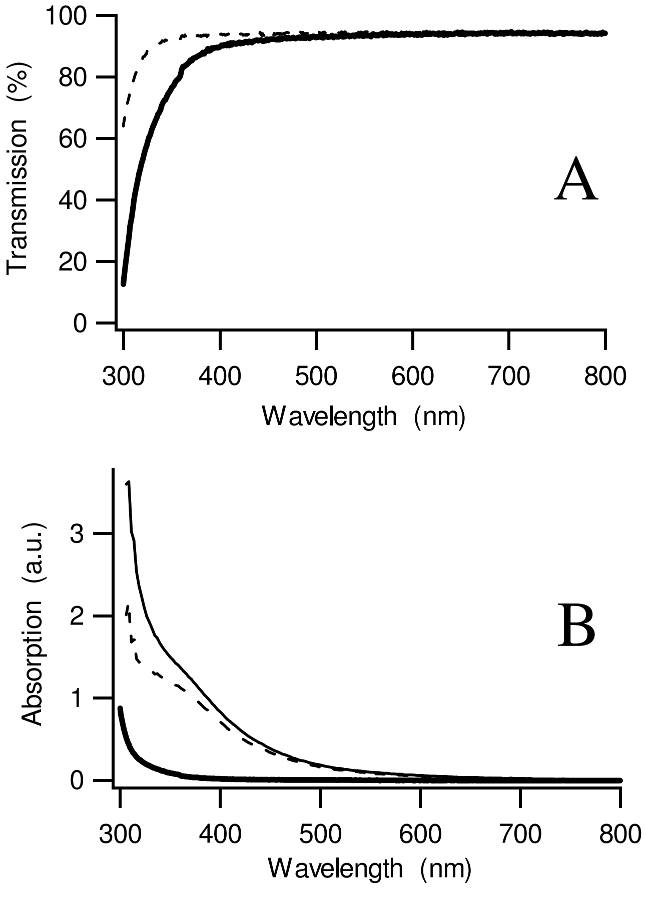

Figure A1.6. UV-vis transmission spectra of a 1:4 TMSPM:MMA copolymer film without HCl after having been dried at 100 °C for 3 hrs (**bold** trace); the dashed line represents the transmission the Pyrex® dish substrate prior to film casting. B) UV-vis absorption data from a 1:4 TMSPM:MMA copolymer film without HCl after having been dried at 100 °C for 3 hrs (**bold** trace) and from the same film after having been cured at 150 °C for 7 hrs (fine trace); the spectral difference is presented as the dashed line showing an absorption peak at ca. 350 nm that corresponds to a yellow discoloration.